Optical properties of single semiconductor nanowires and nanowire ensembles

Probing surface physics by photoluminescence spectroscopy

DISSERTATION

zur Erlangung des akademischen Grades

Dr. rer. nat.
im Fach Physik

eingereicht an der
Mathematisch-Wissenschaftlichen Fakultät I
Humboldt-Universität zu Berlin

von
Dipl.-Phys. Carsten Pfüller
10.11.1980, Berlin

Präsident der Humboldt-Universität zu Berlin:
Prof. Dr. Jan-Hendrik Olbertz

Dekan der mathematisch-Wissenschaftlichen Fakultät I:
Prof. Dr. Andreas Herrmann

Gutachter:

(I.)   Prof. Dr. Henning Richert

(II.)   Prof. Dr. W. Ted Masselink

(iii)   Dr. Pierre Lefebvre

Datum der Promotion: 27. 06. 2011

Abstract

This thesis presents a detailed investigation of the optical properties of semiconductor nanowires (NWs) in general and single GaN NWs and GaN NW ensembles in particular by photoluminescence (PL) spectroscopy.

NWs are often considered as potential building blocks for future nanometer-scaled devices. This vision is based on several attractive features that are generally ascribed to NWs. For instance, they are expected to grow virtually free of strain and defects even on substrates with a large structural mismatch. In the first part of the thesis, some of these expectations are examined using semiconductor NWs of different materials. On the basis of the temperature-dependent PL of Au- and self-assisted GaAs/(Al,Ga)As core-shell NWs, the influence of foreign catalyst particles on the optical properties of NWs is investigated. For the Au-assisted NWs, we find a thermally activated, nonradiative recombination channel, possibly related to Au atoms incorporated from the catalyst. These results indicate the limited suitability of catalyst-assisted NWs for optoelectronic applications. The effect of the substrate choice is studied by comparing the PL of ZnO NWs grown on Si, Al_2O_3, and ZnO substrates. Their virtually identical optical characteristics indicate that the synthesis of NWs may indeed overcome the constraints that limit the heteroepitaxial deposition of thin films.

The major part of this thesis discusses the optical properties of GaN NWs grown on Si substrates. The investigation of the PL of single GaN NWs and GaN NW ensembles reveals the significance of their large surface-to-volume ratio. Differences in the recombination behavior of GaN NW ensembles and GaN layers are observed. First, the large surface-to-volume ratio is discussed to be responsible for the different recombination mechanisms apparent in NWs. Second, certain optical features are only found in the PL of GaN NWs, but not in that of GaN layers. An unexpected broadening of the donor-bound exciton transition is explained by the abundant presence of surface donors in NWs. The existence and statistical relevance of these surface donors is confirmed by PL experiments of single GaN NWs which are either dispersed or free-standing. In this context, the distinct optical characteristics of each individual NW is investigated in greater detail. Third, the increase of the PL intensity of GaN NW ensembles upon exposure to ultraviolet light is ascribed to a reduction of the electric field strengths. These fields are shown to be present in the entire NW volume due to a pinning of the Fermi level at the NW sidewalls. Finally, the quantum efficiency of GaN NWs is studied. The coupling of light with GaN NWs is assessed by comparing the reflectance and the Raman intensities of a GaN NW ensemble with that of a thick GaN layer. A considerably increased extraction efficiency is found for the NWs. In addition, the internal quantum efficiency of GaN NWs is studied by time-resolved PL measurements. The typically observed nonexponential recombination behavior of NW ensembles is explained with a model based on a distribution of recombination rates. This rate distribution is motivated by the above results of this thesis: each NW exhibits its own individual recombination behavior, which is influenced by nonradiative surface recombination, the presence and location of donors within the NW, and the strength of the electric fields. Preliminary simulations using this model describe the nonexponential decay of GaN NW ensembles satisfactorily. The results suggest that nonradiative recombination processes prevail in GaN NWs.

Keywords: Gallium nitride, Nanowires, Photoluminescence, Semiconductor surfaces

Zusammenfassung

Diese Arbeit beschreibt die optische Charakterisierung mittels Photolumineszenz-spektroskopie (PL) von Halbleiter-Nanodrähten (ND) im allgemeinen und einzelnen GaN-ND und GaN-ND-Ensembles im speziellen.

ND werden oftmals als vielversprechende Bausteine zukünftiger, kleinster Bauelemente bezeichnet. Diese Vision beruht insbesondere auf einigen attraktiven Eigenheiten, die ND im allgemeinen zugeschrieben werden: so erwartet man beispielsweise aufgrund der geringen Grenzfläche zum Substrat, dass ND weitestgehend frei von Verspannungen und Defekten selbst auf Substraten mit deutlich unterschiedlichen strukturellen Eigenschaften wachsen. Im ersten Teil dieser Arbeit werden exemplarisch einige dieser Erwartungen näher untersucht. So wird anhand von temperaturabhängigen PL-Messungen an Au- und selbstinduzierten GaAs/(Al,Ga)As-ND der Einfluss des Keimmaterials auf die PL der ND untersucht. Für die Au-induzierten ND finden wir einen thermisch aktivierten, nichtstrahlenden Rekombinationskanal, der möglicherweise mit dem Einbau von Au-Atomen aus dem Nukleationskeim in die ND zusammenhängt. Diese Ergebnisse zeigen, dass fremdinduzierte ND weniger gut für optoelektronische Anwendungen geeignet sind. Weiterhin werden die optischen Eigenschaften von ZnO-ND untersucht, die auf Si-, Al_2O_3- und ZnO-Substraten gewachsen wurden. Die nahezu identischen PL-Spektren dieser Proben zeigen, dass die optischen Eigenschaften von ND weitestgehend losgelöst vom benutzten Substrat sind. Die Herstellung von ND anstelle von Schichten kann daher tatsächlich zur überwindung der vom Substrat vorgegebenen Einschränkung führen.

Die optische Charakterisierung von GaN-ND nimmt den Hauptteil dieser Arbeit ein. Die detaillierte Untersuchung einzelner GaN-ND und von GaN-ND-Ensembles zeigt die Relevanz des großen Oberflächen-zu-Volumen-Verhältnisses. GaN-ND-Ensembles und GaN-Schichten weisen verschiedene Rekombinationsmechanismen auf, die vermutlich auf nichtstrahlende Prozesse an der Oberfläche der ND zurückzuführen sind. Des Weiteren zeigen GaN-ND bestimmte Merkmale in ihrer PL, die für GaN-Schichten nicht beobachtet werden. So wird die unerwartet starke Verbreiterung des strahlenden übergangs donatorgebundener Exzitonen durch das vermehrte Auftreten von Oberflächendonatoren erzeugt, deren statistische Relevanz durch PL-Messungen an einzelnen ausgestreuten und freistehenden GaN-ND nachgewiesen werden kann. Diese Messungen zeigen, dass jeder einzelne ND individuell spezifische optische Eigenschaften aufweist. Weiterhin analysieren wir den Effekt von ultravioletter Bestrahlung der GaN-ND auf deren PL-Intensität. Der beobachtete Anstieg der PL-Intensität wird auf eine Reduzierung der Stärke der elektrischen Felder in den ND zurückgeführt, die durch eine Verankerung des Ferminiveaus an den Seitenflächen der ND verursacht werden. Abschließend untersuchen wir die Quanteneffizienz von GaN-ND. Dazu werden die Ein- und Auskopplung von Licht in GaN-ND und in eine GaN-Schicht mithilfe von Reflektanz- und Ramanmessungen bestimmt. Wir beobachten eine deutlich erhöhte Auskopplung im Fall der ND. Die interne Quanteneffizienz von GaN-ND wird mit zeitaufgelösten PL-Messungen untersucht. Die nichtexponentielle Rekombinationdynamik in ND-Ensembles wird mit einem Modell beschrieben, dass auf einer kontinuierlichen Verteilung der Rekombinationsraten beruht. Diese Verteilung wird durch die vorherigen Ergebnisse motiviert: jeder ND zeigt individuelle optischen Eigenschaften, die durch nichtstrahlende Oberflächenrekombination, das Vorhandensein und die Position von Donatoren und die elektrische Feldestärke bestimmt sind. Vorläufige Ergebnisse dieses Modells beschreiben das nichtexponentielle Rekombinationdynamik zufriedenstellend und implizieren die Dominanz nichtstrahlender Rekombinationsprozesse.

Stichworte: Galliumnitrid, Nanodrähte, Photolumineszenz, Halbleiteroberflächen

Abbreviations

(A^0,X)	Acceptor-bound exciton
CCD	Charge-coupled device
CL	Cathodoluminescence
CNT	Carbon nanotube
cw-PL	Continuous-wave photoluminescence
DAP	Donor-acceptor pair
(D^0,X)	Donor-bound exciton
$(D^0,X_{A,B})$	Donor-bound A or B exciton
FX	Free exciton
$FX_{A,B,C}$	Free A, B, or C exciton
FWHM	Full width at half maximum
hh	Heavy hole
HV	High vacuum
HVPE	Hydride vapor phase epitaxy
IR	Infrared
LED	Light-emitting diode
lh	Light hole
LN	Liquid nitrogen
LO	Longitudinal optical
MBE	Molecular beam epitaxy
MOCVD	Metal-organic chemical vapor deposition
MPL	Conventional photoluminescence
µPL	Micro-photoluminescence
NW	Nanowire
PAMBE	Plasma-assisted molecular beam epitaxy
PL	Photoluminescence
SEM	Scanning electron microscopy
SF	Stacking fault
SO	Surface optical
so	Split-off
SX	Surface exciton
TD	Threading dislocation
TES	Two-electron satellite
TO	Transversal optical
TRPL	Time-resolved photoluminescence
UV	Ultraviolet
(U,X)	Unknown excitonic complex
VIS	Visible
VLS	Vapor-liquid-solid
XRD	X-ray diffractometry

Contents

Contents

1. Introduction

Over the past decade, the field of nanotechnology has been a rapidly developing research area. On the one hand, nanotechnology is a consequence of the ever ongoing miniaturization of semiconductor devices (Moore's law), which approach dimensions well below 50 nm.[1] On the other hand, this field has attracted increasing interest as it opens the way to entirely new device concepts based on phenomena unknown from structures of macroscopic dimensions.[2]

Two distinct approaches for the fabrication of semiconductor nanostructures are established. The conventional "top-down" method is based on the growth of bulk crystals or planar heterostructures. Subsequent lithography, etching, and deposition steps are applied to create functional devices. In the past years, device dimensions have continued following the trend predicted by Moore's law. The spatial resolution of lithographic processes, however, is limited by the wavelength of the light used for exposure. Structures with dimensions smaller than this limit require more sophisticated and more expensive lithography, which eventually reaches physical as well as economic limitations.[1]

Consequently, new concepts for device fabrications are explored ("More-than-Moore"). The synthesis of self-organized nanostructures such as carbon nanotubes (CNTs) or semiconductor nanowires (NWs), i.e., a "bottom-up" approach, has been proposed as an alternative to the conventional top-down methods.[3] While the controlled synthesis of CNTs is still challenging,[4] the growth of semiconductor NWs has been demonstrated for a range of materials.[5–8] Employing semiconductor NWs, precisely controlled structures of different chemical compositions, size, and morphology may be synthesized.[9]

The fabrication of semiconductor heterostructures using the conventional top-down approach is based on the growth of planar films. The deposition of such films poses difficulties due to the mismatch of lattice constants and thermal expansion coefficients. These mismatches result in the generation of defects and strain, which, in general, are detrimental for the desired functionality of the structures. In NWs, the interface dimensions are considerably reduced. As a consequence, extended defects are bound to the interface or are bent to the nearby surface rather than propagating along the entire crystal.[10] Furthermore, an efficient elastic strain relaxation is expected at the interface of an axial heterostructure as well as at the substrate interface.[11–13] In other words, NWs are believed to be essentially free of strain and extended defects, and their functionality is independent of the chosen substrate. For instance, the synthesis of NWs allows for a monolithic integration of direct bandgap semiconductors with standard Si technology.[14] In addition, the defect-free combination of different materials in axial NW heterostructures may drastically improve the performance of optical devices such as light-emitting diodes (LEDs).[15] Due to the unique geometry of NWs, an efficient coupling of light, beneficial for the performance of photodetectors, solar cells, and LEDs, is also expected. The fabrication of other devices such as transistors,[16] biological and chemical sensors,[17] and lasers[18] demonstrates the wide field of applications for NWs. Thus, it is not surprising that NWs are predicted to act as versatile components of future nanometer-scaled devices.[19,20] These visions rely on a number of assumptions. For instance, NWs are believed to grow strain-free on any kind of substrate. The choice of substrate should, in

addition, not affect the crystalline quality and thus the optical and electrical properties of the NWs. Furthermore, different growth techniques and growth mechanisms are often assumed to be equally well-suited for the synthesis of NWs.

Considering the high potential of NWs, it is all the more surprising that many aspects of the fabrication of NWs and of their optical and electrical properties are still poorly understood. For instance, the exact nucleation mechanisms of catalyst-free GaN NWs on AlN have been unveiled only very recently,[21] although the first reports of GaN NW growth appeared more than ten years ago.[5] Catalyst-assisted GaAs NWs are typically of wurtzite phase,[22] while bulk material exhibits a zincblende crystal structure. The incorporation of impurities such as dopants is also not fully understood. Even more scarcely investigated are the electrical and optical properties of NWs, especially with respect to the large surface-to-volume ratio. For example, the origin of commonly observed optical transitions in the photoluminescence (PL) spectra of, e.g., GaN or GaAs NWs,[23,24] has not been determined yet. Another issue is the typically nonexponential recombination behavior exhibited by NWs of various materials,[25,26] and the coupling of light to NWs is controversially discussed.[27–29]

The purpose of the present work is to improve the understanding of the optical properties of semiconductor NWs by using PL spectroscopy. Particular attention is paid to surface-related effects, which are expected to influence the optical properties of NWs due to their large surface-to-volume ratio. Some of the above expectations are examined investigating the PL of semiconductor NWs of different materials. The focus of this thesis lies on the specific optical properties of single GaN NWs and GaN NW ensembles. The synthesis of GaN on Si represents a good example for the monolithic growth of semiconductor heterostructures exhibiting a lattice mismatch. Due to a lack of native substrates,[a] GaN layers are commonly grown on substrates with a different lattice constant such as Si or Al_2O_3. These planar structures generally exhibit strain and a high density of threading dislocations (TDs). As heterostructures of GaN and its alloys potentially cover the entire wavelength range from ultraviolet (UV) to visible light, this material is very attractive for solid-state lighting and photovoltaic applications. Hence, an efficient and cost-effective integration on standard substrates is desirable. This integration may be achieved by growing GaN NWs, and indeed, relatively simple LEDs based on GaN NWs have been demonstrated.[31,32] Moreover, other device concepts have been realized employing GaN NWs. Amongst these are field-effect transistors,[33] photodetectors,[34] diode lasers,[35] and sensors.[18]

The thesis is structured as follows: first of all, an introduction into the theoretical and experimental principles of this thesis is given. The discussion in Chap. 2 focuses on the carrier recombination processes in semiconductors. In addition, electrical and mechanical properties of NWs are briefly considered. In Chap. 3, the experimental methods and setups applied in this work are presented. These comprise the micro-PL (µPL) setup, which is used for the majority of the measurements, two further setups for time-integrated and time-resolved PL, Raman spectroscopy and x-ray diffractometry. Furthermore, the growth and morphology of the NW samples investigated in this work are described.

Two of the above assumptions considering general NW properties are examined in Chap. 4. First, the effect of the catalyst on the optical properties of GaAs/(Al,Ga)As core-

---

[a]It should be noted that bulk GaN is available[30] but the production costs and the limited crystal sizes prohibit its use in commercial applications.

shell NWs is investigated. The temperature-dependent PL of two GaAs/(Al,Ga)As NW samples is compared, one of which is grown employing a Au catalyst and the other one is grown self-assisted. In the second part of this chapter, the consequences of the chosen substrate on the optical characteristics of ZnO NWs are studied. Three ZnO NW samples grown on Si, Al_2O_3, and ZnO substrates are probed.

After the investigation of these general aspects of the optical properties of NWs, the attention is turned to the specific case of GaN NWs. An introduction into their optical properties is given in Chap. 5. The large surface-to-volume ratio is identified to play a significant role for the optical properties of GaN NWs. The recombination processes specific to NWs are discussed comparing the PL of GaN NW ensembles to that of GaN layers. Another important aspect of these PL measurements is the unexpectedly large linewidth of the donor-bound exciton transition of GaN NW ensembles. PL experiments with dispersed and free-standing single GaN NWs have been performed to identify the broadening mechanism that is related to the surface of the NWs. The results are presented in Chap. 6. Electric fields in GaN NWs and their impact on the PL of NWs are studied in Chap. 7. Here, the temporal evolution of the PL intensity of a NW ensemble under continuous exposure to UV light is observed and used to model the desorption of oxygen from the surface of GaN NWs. The results of time-resolved PL measurements are discussed in the context of the large surface-to-volume ratio of the NWs. The coupling of light to GaN NWs is discussed in Chap. 8. By comparing the reflectance and the Raman signal of a GaN layer and a GaN NW ensemble, the external quantum efficiency of GaN NWs is determined. Subsequently, the internal quantum efficiency of GaN NWs is approached using time-resolved PL measurements. A preliminary model of the recombination behavior in NW ensembles based on the surface-related phenomena discussed in the previous chapters is introduced. The PL spectra of GaN NWs exhibit a commonly observed transition band at 3.45 eV, whose origin is still under debate. The findings of the experiments presented in the previous chapters regarding this luminescence band are summarized and discussed in Chap. 9.

Finally, the results of the thesis are concluded in Chap. 10 and a brief outlook is given.

2. Basics

In the following, the fundamentals necessary for the understanding of this thesis are presented. First of all, the band structure of semiconductors is described. Afterwards, the optical excitation of semiconductors is discussed, and particular attention is paid to the subsequent recombination processes. Two main recombination mechanisms are distinguished, namely excitonic and free-carrier recombination. The focus of this work lies on GaN, which shows a mixture of these two recombination mechanisms at room temperature. In contrast, the recombination in ZnO is almost entirely excitonic, while in GaAs free-carrier recombination dominates at room temperature. Therefore, the specifics of excitonic and free-carrier recombination are illustrated using ZnO and GaAs, respectively. As references, the books of Kittel,[36] Morkoç,[37] Pankove,[38,39] and Knox[40] are used. Additional references are indicated where necessary.

2.1. Crystal structure and band structure

When atoms are brought close together such that they form a crystal, the overlap of the electron wave functions eventually leads to the formation of energy bands separated by bandgaps. The resulting band structure determines to a large extent the optical and electrical properties of a crystal. In direct bandgap semiconductors, the valence band maximum and the conduction band minimum are located at the same position in **k**-space, which is typically the center of the Brillouin zone, labeled as the Γ-point.

In thermodynamic equilibrium, GaAs crystallizes in the zincblende structure as most III-V semiconductors do, while GaN as well as ZnO condenses in the wurtzite structure (see Fig. 2.1). However, the meta-stable phase (wurtzite in the case of GaAs and zincblende for GaN and ZnO) has also been observed, in particular during the growth of NWs.[42–44] Due to the tetrahedral structure, the distances to the nearest neighbors as well as to the next-nearest neighbors are virtually identical in both crystal structures. The decisive difference is the third nearest neighbor relation. The simplest way to visualize this difference is by looking along the ⟨111⟩ direction in the zincblende or along the ⟨0001⟩ direction (also referred to as *c*-direction or *c*-axis) in the wurtzite crystal (denoted by the arrows in Fig. 2.1).

In Figure 2.2, the near-bandgap band structure of zincblende GaAs and wurtzite GaN close to the center of the Brillouin zone (denoted as the Γ-point) is shown. The conduction band is composed of atomic s orbitals, while the valence band is built by p-like orbitals. In the zincblende GaAs crystal, the heavy hole (hh) and light hole (lh) band are degenerate at the Γ-point, and only the split-off (so) band is separated due to spin-orbit interaction. In the wurtzite phase, however, an additional crystal field along the *c*-axis is present, resulting in a splitting of the degenerate states. Consequently, three separate valence bands exist near the band edge. They are commonly denoted as A, B, and C valence band, beginning from the top.

At low growth temperatures, or if impurities or strain are present, the formation of stacking faults (SFs) can be observed. SFs can be thought of as being a zincblende in-

(a) Zincblende crystal structure. The stacking sequence is $\ldots ABCABCABC \ldots$. The arrow denotes the $\langle 111 \rangle$ direction.

(b) Wurtzite crystal structure. The stacking sequence is $\ldots ABABABAB \ldots$. The arrow denotes the $\langle 0001 \rangle$ direction.

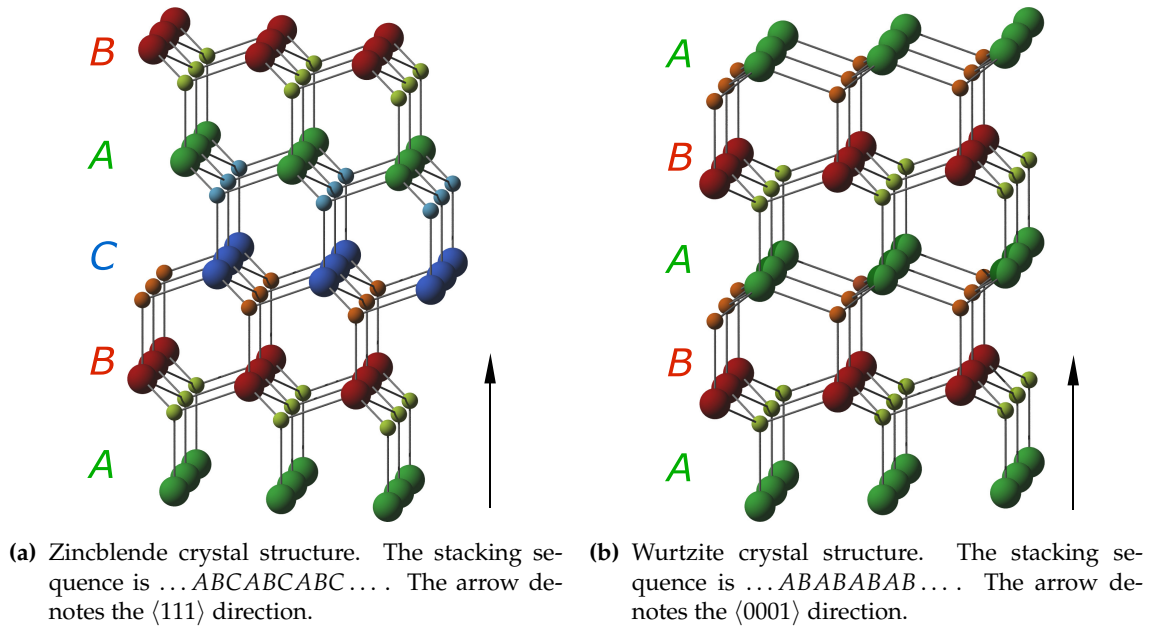Figure 2.1.: Ball-and-stick model of a zincblende and a wurtzite crystal. The large balls represent cations (e.g., In, Ga, Zn,...) and the small balls depict anions (e.g., As, N, O,...). The lattice planes A, B, and C are marked green, red, and blue, respectively. The visualizations have been created using the program DIAMOND.[41]

(a) Band structure of zincblende crystals.
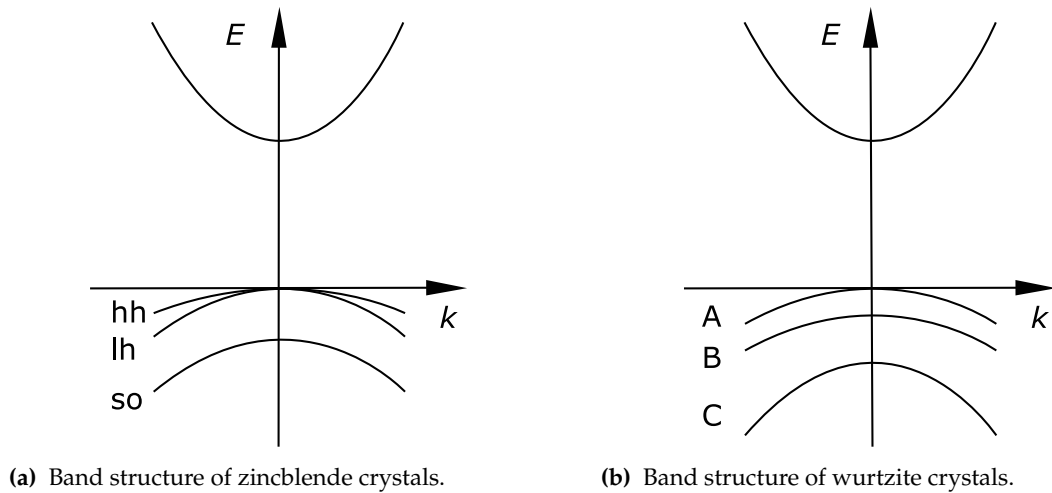
(b) Band structure of wurtzite crystals.

Figure 2.2.: Schematic comparison of the near-bandgap band structure of zincblende and wurtzite semiconductor crystals close to the Γ-point.[37,39] The diagrams are not drawn to scale.
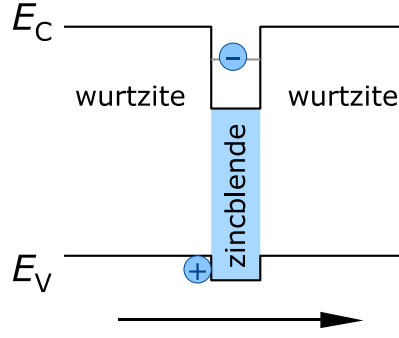
Figure 2.3.: Band profile of a stacking fault (zincblende insertion into a wurtzite crystal) with stacking sequence $...ABAB$ABC$ABAB...$. The horizontal arrow denotes the c-direction. The SFs act as barriers for holes but as QWs for electrons.

sertion in a wurtzite crystal and vice versa, i.e., $...ABCABC$AB$ABCABC...$ for the former case and $...ABAB$ABC$ABAB...$ for the latter. In both cases, SFs form planar. The zincblende and the wurtzite phase of a certain material typically have different bandgaps. Considering the specific alignment of conduction and valence band edges in the c-direction of GaN and GaAs, SFs form quantum wells for electrons and barriers for holes,[45] as shown in Fig. 2.3. Hence, they may localize electrons or excitons and thus represent efficient recombination channels. In fact, luminescence related to SFs is present in the luminescence of both GaN and GaAs NWs.[46,47]

2.2. Recombination processes

The intrinsic optical properties of a semiconductor are determined by its band structure, in particular by the bandgap. In addition, defects and impurities represent radiative or nonradiative recombination centers and thus influence the luminescence properties of a crystal. PL spectroscopy allows for the non-destructive investigation of the optical characteristics of semiconductors. PL is highly sensitive to radiative defects and impurities, and thus, this method is ideally suited to obtain information about the nature of crystal defects and incorporated impurities, even if their concentration is very low.

Excitation of free carriers and formation of excitons

Semiconductors are transparent for light with a photon energy $\hbar\omega$ below the bandgap energy E_G. Thus, in PL experiments, semiconductors are excited using light with $\hbar\omega_{exc} > E_G$. Figure 2.4 displays a schematic description of the generation of carriers. By the absorption of a photon, an electron is lifted from the valence band into the conduction band leaving behind a hole. As the excitation energy is usually a little larger than the bandgap, the two free carriers have a certain excess energy. Emitting longitudinal optical (LO) phonons, the carriers thermally relax to the band edges. Due to Coulomb attraction, the electron and the hole form a bound state referred to as the exciton. This bound state can be formally described in the same way as a hydrogen atom, with two fundamental differences: First, the electron and hole masses m_e^* and m_h^* are typically of the same order, and second, the Coulomb interaction is screened by the dielectric constant ε_s[a] of the

---

[a]The dielectric constant ε_s is here defined as the product of the material specific relative permittivity ε and the vacuum permittivity ε_0, i.e., $\varepsilon_s = \varepsilon\varepsilon_0$.
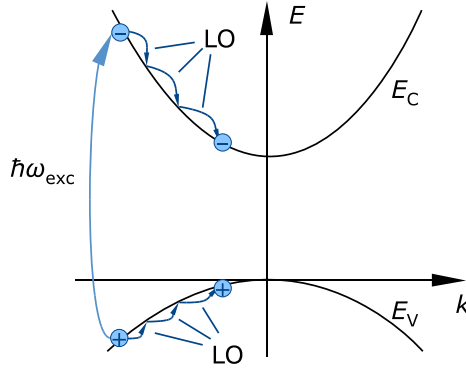
Figure 2.4.: Carriers are generated by absorption of light with $\hbar\omega_{\mathrm{exc}} > E_{\mathrm{G}}$. An electron is excited from the valence band into the conduction band leaving behind a hole. The two opposite carriers thermalize via LO phonon emission to the band edges.

semiconductor in which the exciton is excited. The corresponding Schrödinger equation can be written as:

$$\left(-\frac{\hbar^2}{2m_{\mathrm{e}}^*}\nabla_{\mathrm{e}}^2 - \frac{\hbar^2}{2m_{\mathrm{h}}^*}\nabla_{\mathrm{h}}^2 - \frac{e^2}{4\pi\varepsilon_{\mathrm{s}}}\frac{1}{r_{\mathrm{eh}}} \right)\Psi = E\Psi\,. \tag{2.1}$$

e and $\hbar$ are the elementary charge and Planck's constant, respectively, and r_{eh} is the distance between the electron and the hole. Pursuant to the solution of the hydrogen atom, the separation of the center-of-mass and the relative motion yields an instructive solution for the exciton wave function:

$$\Psi = \frac{1}{\sqrt{V}}e^{i\mathbf{k}\mathbf{R}}\Phi(\mathbf{r})\,, \tag{2.2}$$

where $\mathbf{k}$ denotes the crystal momentum and V stands for the crystal volume. The center-of-mass coordinate $\mathbf{R}$ and the relative position $\mathbf{r}$ are defined by the electron and hole coordinates $\mathbf{r}_e$ and $\mathbf{r}_h$:

$$\mathbf{R} = \frac{1}{2}(\mathbf{r}_e + \mathbf{r}_h) \qquad \text{and} \qquad \mathbf{r} = (\mathbf{r}_e - \mathbf{r}_h)\,. \tag{2.3}$$

The energy of an exciton in the nth state can now be obtained from Eq. 2.1:

$$E_n = E_{\mathrm{G}} + \frac{\hbar^2 k^2}{2(m_{\mathrm{e}}^* + m_{\mathrm{h}}^*)} - E_{\mathrm{FX}}\,. \tag{2.4}$$

The second term in Eq. 2.4 is the kinetic energy of the exciton due to its center-of-mass motion. The last term in Eq. 2.4, the free exciton binding energy E_{FX}, is obtained from the relative motion $\Phi(\mathbf{r})$. Adjusting the well-known solution of the hydrogen atom, E_{FX} can be written as:

$$E_{\mathrm{FX}} = -\frac{\mu e^4}{32\pi^2\hbar^2\varepsilon_{\mathrm{s}}^2}\frac{1}{n^2}\,, \tag{2.5}$$

Table 2.1.: Parameters of free excitons in GaAs, GaN, and ZnO. The GaN layers investigated in Refs. 48 and 49 were grown homoepitaxially on single crystal GaN substrates. Transition energies were obtained by reflectance and PL measurements at temperatures below 10 K.

	GaAs		GaN		ZnO
Crystal structure	zincblende		wurtzite		wurtzite
Exciton binding energy E_{FX} (meV)	4.2[50]	A	24.8[51] 25.2[53] 26.7[54]	A	60[52]
		B	24.7[51] 25.3[53]	B	57[52]
		C	26.8[51] 27.3[53]		
Exciton transition energy $\hbar\omega$ (eV)	1.5153[55]	A	3.479[48] 3.4776[49]	A	3.3773[52] 3.3771[56]
		B	3.484[48] 3.4827[49]	B	3.3895[52] 3.3898[56]
		C	3.502[48] 3.5015[49]	C	3.4335[56]
Exciton Bohr radius a_B (nm)	11[57]		3[58]		1.8[59]

with μ being the reduced exciton mass:

$$\frac{1}{\mu} = \frac{1}{m_e^*} + \frac{1}{m_h^*}\,.$$ (2.6)

In the same manner, the exciton Bohr radius a_B can be defined as:

$$a_B = \frac{4\pi\hbar^2\varepsilon_s}{\mu e^2}n^2\,,$$ (2.7)

describing the "size" of an exciton. Exciton binding and transition energies as well as exciton Bohr radii for GaAs, GaN, and ZnO are listed in Tab. 2.1. Excitons in GaN and ZnO may consist of holes from either of the three valence bands denoted as A (FX$_A$), B (FX$_B$), and C excitons (FX$_C$). The notation FX is equivalent to FX$_A$ in this thesis. The excitons in the materials considered in this work are seen to span over several unit cells. Such excitons are highly mobile and are called Wannier-Mott excitons. Excitons in materials with low dielectric constants such as alkalihalides have a size comparable to the unit cells. They are referred to as Frenkel excitons and are not considered here.[40]

The center-of-mass wave function is determined by the properties and dimensions of the host material. In a perfect, infinite crystal, it has the form of a plane wave. In this case, the free exciton can be considered as a coherent excitation of the entire crystal.[60]

In finite crystals, the center-of-mass wave function is described by much more complex expressions. If the kinetic energy is larger than E_{FX}, the exciton is not stable and dissociates. In most cases, excitons in the ground state $n = 1$ with zero kinetic energy ($\mathbf{k} = 0$) are considered, as only these are allowed to decay radiatively.

Donor- and acceptor-bound excitons

Shallow donors and analogously shallow acceptors[b] can be treated as hydrogenic impurities characterized by a certain binding or ionization energy E_I of the loosely bound electron and hole, respectively:

$$E_I = -\frac{m_e^* e^4}{32\pi^2\hbar^2\varepsilon_s^2}\frac{1}{n^2}. \tag{2.8}$$

As E_I is small compared to the bandgap, donors introduce energy levels slightly below the conduction band. If a free exciton feels the potential of a donor, its center-of-mass wavefunction collapses, and the exciton is localized at the donor, forming an excitonic complex [(D^0,X)[c]]. This complex is of hydrogenic nature with a characteristic binding energy E_X. The relation between E_X and E_I for a given semiconductor is empirically described by Haynes rule:[61]

$$E_X = \alpha_D E_I, \tag{2.9}$$

where the proportionality constant α_D depends on the ratio of m_e^* and m_h^* and typically takes values between 0.1 and 0.2. E_I resembles the ionization energy of a hydrogen atom with modified mass and dielectric constant. The ionization energy thus depends on the chemical nature of the semiconductor and varies for different materials. Due to the central-cell-correction the values of E_I are generally larger than predicted by Eq. 2.8, giving rise to various characteristic shallow and deep donor levels as well as exciton binding energies E_X. Consequently, low-temperature PL spectroscopy with $k_B T \ll E_X$, where $k_B T$ denotes the Boltzmann constant, allows for the identification of certain impurities in a semiconductor. Donors and acceptors represent efficient recombination centers as bound excitons are strongly localized. Their oscillator strength is strongly increased compared to free excitons in bulk, and thus, the radiative recombination of bound excitons dominates the luminescence at low excitation densities.[62]

Figure 2.5 illustrates schematically a (D^0,X) complex. As mentioned before, the recombination of such a (D^0,X) can occur via different recombination channels. If the exciton recombines directly, the donor is left behind in its ground state, as shown in the left part of Fig. 2.5. For the Auger-like recombination process via two-electron satellites (TES), a fraction of the exciton energy is used to excite the excess electron of the donor. The emitted phonon energy is consequently reduced by a certain amount, e.g., $3E_I/4$ if the donor is left behind in the first excited state. When excitons couple to LO phonons, the energy of the emitted photon is also reduced by one ore more LO phonon energies.

---

[b]All considerations regarding donors can be analogously employed for acceptors replacing the effective electron mass m_e^* with the effective hole mass m_h^*, changing the sign of the charge e, and taking the top of the valence band as reference instead of the bottom of the conduction band.

[c]Just as for FX, bound excitons may consist of holes from either of the three valence bands. Throughout this thesis, (D^0,X) is equivalent to (D^0,X_A), i.e., the hole originates from the A valence band. Only where necessary, the origin of the hole is indicated by indices.
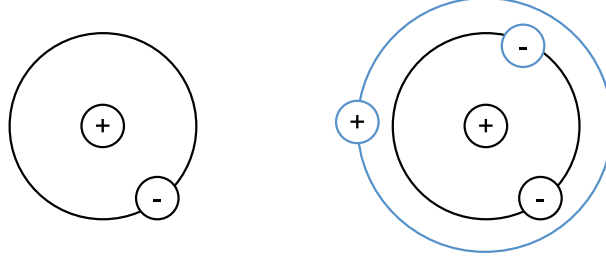
Figure 2.5.: Illustration of a donor (left) and a (D^0,X) complex (right). The black symbols indicate the atom core $\oplus$ of the donor and its excess electron $\ominus$. The blue symbols are the positive (hole) and negative (electron) charges provided by the exciton.[37,39]
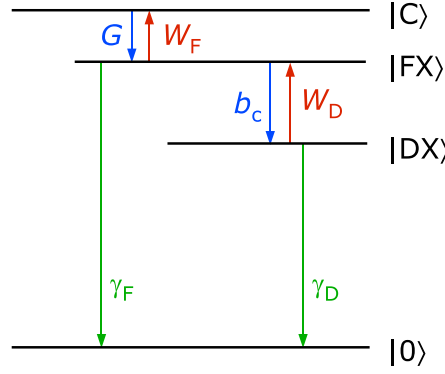

Figure 2.6.: Scheme of excitonic generation (blue arrows), recombination (green), and dissociation (red) processes in semiconductors. $|C\rangle$ and $|0\rangle$ denote the crystal continuum and ground state, respectively.

Excitonic recombination

Excitonic recombination dominates the recombination processes as long as $k_B T \ll E_{FX}$. For instance, this condition is met for GaN and ZnO investigated at low temperatures. Once being created, a free exciton can either recombine, bind to a defect, or an impurity or dissociate. All of these processes are associated with a respective rate. Hence, a system of coupled rate equations can be used to describe them. Let n_F be the free-exciton density in an n-type semiconductor with donor concentration N_D and let N_D^0 be the density of unoccupied donors. Denoting the density of occupied donors as N_D^+, the recombination dynamics is described by:

$$0 = \frac{dn_F}{dt} = G - \gamma_F n_F - b_c n_F N_D^0 + W_D N_D^+ - W_F n_F \,, \tag{2.10a}$$

$$0 = \frac{dN_D^0}{dt} = -\gamma_D N_D^+ + b_c n_F N_D^0 - W_D N_D^+ \,. \tag{2.10b}$$

In Fig. 2.6, this rate equation system is illustrated. The coefficients used in this model are the following:

G The rate at which free excitons are generated by the optical excitation.

γ_F Recombination rate of free excitons, comprising radiative and nonradiative recombination: $\gamma_F = \gamma_{F,r} + \gamma_{F,nr}$. If a free exciton recombines radiatively, it emits a photon

of the energy $\hbar\omega = E_G - E_{FX}$. Nonradiative recombination may, for example, occur at threading dislocations[63] or at the crystal surface.

b_c Coefficient describing the capture of free excitons to neutral donors.

W_F Dissociation rate of free excitons. Different mechanisms can lead to the dissociation of free excitons. If the thermal energy $k_B T$ is larger than the exciton binding energy E_{FX}, free excitons are likely to dissociate into free carriers before recombining or getting trapped by defects. The dissociation of free excitons can also be caused by other mechanisms. For instance, excitons may be ionized by impacts with other excitons or carriers, or by the presence of an electric field, which separates the electron and the hole of the exciton.

γ_D Recombination rate of the (D^0,X) complex, which again includes radiative and nonradiative recombination: $\gamma_D = \gamma_{D,r} + \gamma_{D,nr}$. If a (D^0,X) recombines radiatively, in general a photon of the energy $\hbar\omega = E_G - E_{FX} - E_X$ is emitted. The energy of the emitted photon is reduced if the exxciton recombines via TES transitions or couples with LO phonons. Auger recombination is a typical nonradiative decay process. The exciton recombines nonradiatively and excites the bound electron into the conduction band. [64]

W_D Dissociation rate of the (D^0,X) complex. A donor-bound exciton can be released from its donor due to thermal energy or other ionization processes and become a free exciton.

If other defects (e.g., SFs) or impurities such as acceptors are present in a significant concentration, the rate equation system has to be expanded by appropriate expressions for the corresponding rates.

The dissociation rate W_F of free excitons depends on temperature. At sufficiently high temperatures ($k_B T > E_{FX}$), the formation of excitons is suppressed. Thus, E_{FX} determines, whether recombination of excitons or of carriers dominates at a certain temperature. At room temperature ($k_B T = 26\,\text{meV}$) for instance, excitonic recombination can be observed in ZnO ($E_{FX} = 60\,\text{meV}$), while in GaAs ($E_{FX} = 4\,\text{meV}$) free-carrier recombination is predominant. The recombination processes in GaN, however, are a mixture of both types. At low temperatures, the recombination processes in both GaN and ZnO are well represented by Eqs. 2.10.

For low excitation densities ($n_F \ll N_D$) Eqs. 2.10 can be linearized. In this case, the density of bound excitons n_D instead of N_D^0 is used, and the term $b_c n_F N_D^0$ is replaced by $\gamma_c n_F$. In the general case, Eqs. 2.10 is a nonlinear system of coupled differential equations. For a discussion of the excitonic recombination dynamics, see App. B.

Free-carrier recombination

For GaAs at room temperature, the decay processes are dominated by free-carrier recombination, since $k_B T \gg E_{FX}$ and excitons dissociate. Hence, Eqs. 2.10 does not represent the recombination processes in GaAs at room temperature. Instead, the densities of free electrons n and free holes p have to be considered. Under steady state conditions, their rates are given by:

$$\frac{dn}{dt} = G - Bnp - b_n n n_t^+ = 0, \tag{2.11a}$$

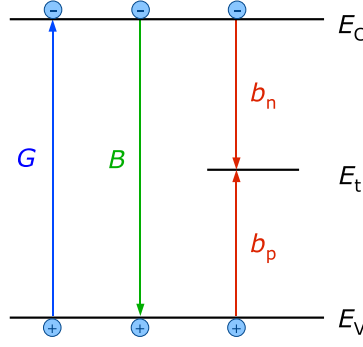$$\frac{dp}{dt} = G - Bnp - b_p p n_t^0 = 0. \tag{2.11b}$$

Figure 2.7.: Scheme of free carrier generation (blue arrow), radiative (green) and nonradiative recombination (red).

Here, G again denotes the generation rate, B the radiative recombination coefficient, and b_n and b_p the capture coefficients of positively charged (n_t^+) and neutral (n_t^0) nonradiative centers, respectively. Eqs. 2.11 are illustrated schematically in Fig. 2.7. Considering the case of n-type semiconductors (with a donor density N_D), the electron and hole densities are $n = N_D + \Delta n$ and $p = \Delta p$, respectively, where $\Delta n = \Delta p$ is the number of excited carriers.

The recombination rate R_{nr} via nonradiative centers with a density $N_t = n_t^+ + n_t^0$ is:

$$R_{nr} = \frac{b_n b_p np}{b_n n + b_p p} N_t\,, \tag{2.12}$$

which is the well-known Shockley-Read-Hall expression (see App. B).[65,66] In the case of low excitation density, i.e., if $\Delta n = \Delta p \ll N_D$, the radiative decay is described by:

$$Bnp = BN_D\Delta p = \gamma_r \Delta p = \tau_r^{-1}\Delta p\,, \tag{2.13}$$

and analogously the nonradiative decay by:

$$R_{nr} = b_p N_t \Delta p = \gamma_{nr}\Delta p = \tau_{nr}^{-1}\Delta p\,, \tag{2.14}$$

with τ_r (τ_{nr}) and γ_r (γ_{nr}) denoting the radiative (nonradiative) recombination times and rates, respectively. For high excitation ($\Delta n = \Delta p \gg N_D$), the radiative recombination is given by:

$$Bnp = B\Delta p^2\,, \tag{2.15}$$

yielding a nonexponential decay. In contrast, the nonradiative recombination is given by:

$$R_{nr} = \frac{b_p b_n}{b_p + b_n} N_t \Delta p = \gamma_{nr}\Delta p = \tau_{nr}^{-1}\Delta p\,. \tag{2.16}$$

A detailed discussion of the decay dynamics can be found in App. B.

Typically, all of the described recombination processes occur simultaneously, and the recombination schemes shown in Figs. 2.6 and 2.7 provide only highly simplified pictures of the recombination processes in a semiconductor. To indicate the complexity of these processes, Fig. 2.8 depicts some of the additional radiative recombination processes
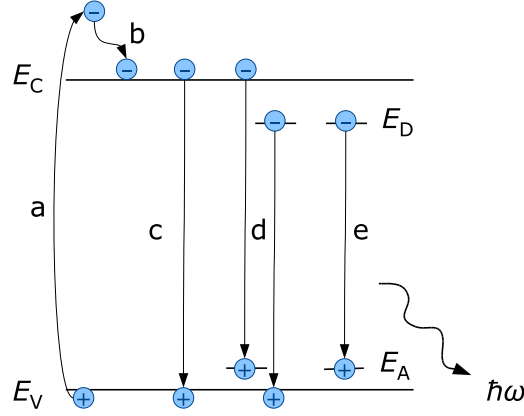
Figure 2.8.: Scheme of generation and radiative recombination processes in semiconductors. (a) Generation of electron-hole pair (b) relaxation to band edge (c) band-to-band recombination (d) free-to-bound recombination (e) donor-acceptor-pair recombination. E_D and E_A denote the donor and acceptor levels in the bandgap.

related to free carriers. Each of these processes is related to a respective rate, determined by external parameters such as the temperature. Consequently, when the recombination dynamics in a semiconductor is investigated, e.g., by means of time-resolved PL spectroscopy, effective recombination rates γ_{eff} or effective lifetimes τ_{eff} are obtained. They relate to the radiative and nonradiative rates and lifetimes as:

$$\gamma_{\text{eff}} = \gamma_{\text{r}} + \gamma_{\text{nr}}, \tag{2.17}$$

$$\tau_{\text{eff}}^{-1} = \tau_{\text{r}}^{-1} + \tau_{\text{nr}}^{-1}. \tag{2.18}$$

From the radiative and nonradiative recombination rates, the internal quantum efficiency η_{int} can be determined:

$$\eta_{\text{int}} = \frac{\gamma_{\text{r}}}{\gamma_{\text{r}} + \gamma_{\text{nr}}} = \frac{\tau_{\text{eff}}}{\tau_{\text{r}}}. \tag{2.19}$$

η_{int} describes the efficiency of the conversion of electron-hole pairs or excitons into photons *inside* a semiconductor crystal. For PL experiments, the coupling of light into the crystal as well as its extraction are of importance. Considering the respective efficiencies η_{in} and η_{out}, the PL intensity is given by:

$$I_{\text{PL}} = \eta_{\text{ext}} I_{\text{L}}, \tag{2.20}$$

where I_{L} is the intensity of the exciting laser and $\eta_{\text{ext}} = \eta_{\text{in}} \eta_{\text{int}} \eta_{\text{out}}$ is the external quantum efficiency.

Absorption and emission in planar layers

Light hitting the surface of a planar semiconductor layer is, depending on its wavelength, partially reflected and partially absorbed or transmitted. The reflectance R of a layer with an ideally flat surface can be deduced from the complex index of refraction n_{s} of

the semiconductor and that outside of the crystal, typically air or vacuum ($n_1 \approx 1$). For normal incidence R is given by:

$$R = \left| \frac{n_s - 1}{n_s + 1} \right|^2 .$$ (2.21)

The fraction of light that is not reflected is coupled into the crystal, i.e., $\eta_{in} = 1 - R$. The absorption of light in opaque materials is described by Beer's law:

$$I(z) = I_0 e^{-\alpha z} ,$$ (2.22)

where the intensity $I(z)$ at a distance z from the surface is related to the intensity I_0 at the surface and to the absorption coefficient α, which is a function of the energy $\hbar\omega$ of the light. Ideally, $\alpha(\hbar\omega < E_G)$ is zero, i.e., the semiconductor is transparent, for photons with an energy below the bandgap. For light with a photon energy above the bandgap, the semiconductor is strongly absorbing [$\alpha(\hbar\omega > E_G) > 0$]. The penetration depth z_p can be obtained from Eq. 2.22 with $I(z_p) = I_0 e^{-1}$. In PL experiments on planar layers, z_p roughly describes the depth up to which carriers are generated.

The extraction of light from such a planar layer is highly inefficient. Photons can only escape from the crystal if they travel toward the surface under an angle smaller than the critical angle β_c of total internal reflection, which is determined by Snell's law:

$$\beta_c = \arcsin\left(\frac{n_1}{n_s} \right) .$$ (2.23)

The resulting escape cone describes a section of a sphere. Relating the surface of the cone cap to the surface of this sphere, the extraction efficiency η_{out} can be roughly estimated to:

$$\eta_{out} = \frac{1 - \cos\beta_c}{2} .$$ (2.24)

The extraction efficiency η_{out} of planar layers is thus limited by total internal reflection.

Absorption and emission in nanowires

The diameter of the NWs investigated in this work is in general smaller than the wavelength of both the exciting as well as the emitted light. For this reason, geometric optics as above cannot be applied to describe the penetration of light into and the extraction of light out of the NW material. The incoming light can be considered as a plane wave, as the minimum laser spot has a diameter of several μm (see Sec. 3.2). According to Huygens' principle, each point of a wavefront of this plane wave acts as a source of a new spherical wave. The newly created spherical waves are superimposed and form a new wavefront. If such a wavefront encounters a NW ensemble, it will be diffracted by the NW tips. In other words, each NW tip acts accordingly as an origin of a new spherical wave that propagates in all directions. Consequently, the NWs are excited from the side rather than from the top and over their entire length. Due to their complexity, these processes are not understood quantitatively.
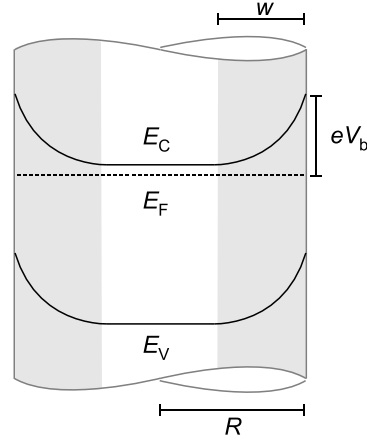
Figure 2.9.: Schematics of conduction the (E_C) and valence band (E_V) profile across a NW. The Fermi level E_F is pinned at eV_b below the conduction band edge at the NW sidewalls. The gray shaded areas depict the depletion region.

2.3. Electrical properties

The presence of donors (as well as acceptors) does not only affect the optical properties of a semiconductor as described in the previous section, but also its electrical characteristics. Shallow, hydrogenic donors supply electrons which are weakly bound with the ionization energy E_I. In a one-particle picture, the excess electron resides on a donor level E_D within the bandgap, separated by the ionization energy E_I from the conduction band edge E_C (see Fig. 2.7). If the excess electron is lifted into the conduction band, e.g., through thermal activation, it can contribute to carrier transport in the crystal. Donor levels may also be introduced by intrinsic point defects such as vacancies.

In undoped semiconductors, the Fermi level E_F lies in the middle of the bandgap. With the introduction of a donor level, the Fermi level is shifted toward the conduction band edge such that it resides between E_C and E_D at low temperatures. The same considerations apply analogously for holes, introduced by doping with acceptors.

At the surface of a crystal, the Fermi level can be pinned within the bandgap due to the presence of surface states. These surface states may be introduced for instance by dangling bonds or adsorbates. In *n*-type semiconductors, the conduction and valence band edges bend upwards, thus forming a potential that is repulsive to electrons and attractive to holes. The result is a depletion region region close to the surface, as illustrated in Fig. 2.9. The band alignment is described by Poisson's equation, which relates the potential ϕ to the carrier density N.

Poisson's equation

The one-dimensional form of Poisson's equation can be written in Cartesian coordinates:

$$\frac{\partial^2 \phi}{\partial x^2} = -\frac{\rho}{\varepsilon_s} = -\frac{qN}{\varepsilon_s} , \tag{2.25}$$

where ρ denotes the charge density and q is the charge. NWs can be approximated by infinitely long cylinders. Hence, Eq. 2.25 is transformed into cylindrical geometry:

$$\frac{\partial^2 \phi}{\partial r^2} + \frac{1}{r}\frac{\partial \phi}{\partial r} = -\frac{qN}{\varepsilon_s} \tag{2.26}$$

with the general solution:

$$\phi(r) = -\frac{qN}{4\varepsilon_s}r^2 + C_1 \ln(r) + C_2 . \tag{2.27}$$

C_1 and C_2 are integration constants, which are determined by the boundary conditions of the specific problem. For sufficiently large carrier concentrations N, the NWs are only partially depleted (see Fig. 2.9). The boundary conditions can then be determined to $\partial\phi(R-w)/\partial r = 0$ and $\phi(R) = V_b$, with V_b resulting from the Fermi level pinning at the surface.[67] Here, R denotes the radius of the NW. Consequently, the integration constants can be determined to:

$$C_1 = \frac{qN}{2\varepsilon_s}(R-w)^2 \qquad \text{and} \qquad C_2 = V_b + \frac{qN}{2\varepsilon_s}\left[\frac{1}{2}R^2 - (R-w)^2\ln(R)\right], \tag{2.28}$$

which yields the following solution for the potential in an n-type NW ($N = N_d$ and $q = -e$):

$$\phi(r) = V_b - \frac{eN_d}{2\varepsilon_s}\left[\frac{1}{2}(R^2 - r^2) + (R-w)^2 \ln\left(\frac{r}{R}\right)\right]. \tag{2.29}$$

The depletion width w can be obtained by setting $e\phi(w) = (E_C - E_F)$, which yields a transcendental equation with respect to w. Although w cannot be expressed in a closed analytical form, the critical parameters determining its value can be identified as the Fermi level pinning V_b and the doping density N_d. The Fermi level pinning depends on various factors, such as surface orientation, adsorbed species, and even growth conditions.[68] In the case of n-type GaN, the vast majority of reports refers to C-plane surfaces, with the Fermi level pinning taking values of about 1 eV for surfaces exposed to air[69,70] and 0.3 to 1.4 eV for clean surfaces.[68,71–73] Here, however, the Fermi level pinning at the NW sidewalls, i.e., at M-plane surfaces is of interest. For this surface, only few studies exist. Based on calculations within the local-density approximation, clean M-plane GaN surfaces are believed to have no surface states inside the bandgap and thus they do not pin the Fermi level.[74] In contrast, other calculations[68] as well as photoconductivity experiments of GaN NWs[75] confirm the presence of Fermi level pinning at about 0.6 eV below the conduction band edge, possibly due to the exposure to air in the experiment.

If the NW is fully depleted ($w = R$), Eq. 2.29 yields a parabolic potential:[67,76,77]

$$\phi(r) = V_b - \frac{eN_d}{4\varepsilon_s}(R^2 - r^2). \tag{2.30}$$

The first derivative of the potential describes the electric field $\mathcal{E}(r)$ in the NW:

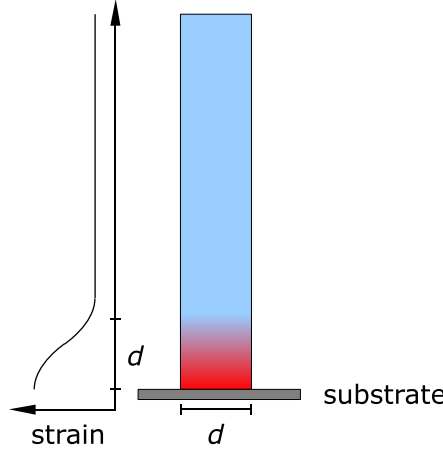$$\mathcal{E}(r) = -\frac{\partial \phi}{\partial r} . \tag{2.31}$$

Figure 2.10.: Schematics of the principle of St. Venant. The strain introduced by the lattice mismatch at the NW/substrate interface is pictured by the red color.

In other words, the slope of the conduction and valence band introduced by the Fermi level pinning causes an electric field $\mathcal{E}(r)$ across the NW diameter. According to Eq. 2.29, it is given by:

$$\mathcal{E}(r) = \frac{eN_\mathrm{d}}{2\varepsilon_\mathrm{s}}r - \frac{eN_\mathrm{d}(R-w)^2}{2\varepsilon_\mathrm{s}}\frac{1}{r}, \qquad (2.32)$$

or in the case of full depletion by:

$$\mathcal{E} = \frac{eN_\mathrm{d}}{2\varepsilon_\mathrm{s}}r. \qquad (2.33)$$

Note, that Eqs. 2.30 and 2.33 differ only by a factor of 2 from the equivalent solution for a thin semiconductor film.

At the NW surface, the electric field reaches its maximum value, while it vanishes in the center of the NW. The presence of electric fields affect the recombination processes in the NWs. In an exciton, the electron and the hole are separated, and thus, the overlap of their wavefunctions is reduced. Consequently, the radiative recombination rates for excitonic recombination are decreased in the presence of electric fields. If the electric field strength is sufficiently high, i.e., if the potential drop across the exciton Bohr radius a_B corresponds to an energy larger than the exciton binding energy E_FX, the exciton dissociates into free carriers.

2.4. Mechanical properties of nanowires

In contrast to layers, NWs are virtually free of strain even when grown on lattice mismatched substrates. Due to their large surface-to-volume ratio, strain accumulated at the NW/substrate interface is effectively released.[78] The principle of St. Venant[79–81] describes this strain release, which is illustrated in Fig. 2.10.[d] Let an elastic rod with diameter d be clamped at one end but otherwise be free. At the clamped end, strain is

---

[d]In Ref. 81 an explicit solution of this problem is given.

introduced into the rod. As the surface is free, this strain can be released by elastic deformation. Within a distance from the clamped end that corresponds to *d*, the strain is entirely relieved.

If the diameter exceeds a critical value, strain may be released by plastic deformation, forming extended defects. [11,12,21] These defects are found to either be bound to the interface or to be terminated at the nearby surface. Thus, in the lower part of a NW close to the NW/substrate interface, defects and strain may be present, while in the upper part the material is essentially free of strain and extended defects.

Similar considerations apply to axial heterostructures in NWs. The lattice mismatch of heterostructures may be designed to be higher in NWs than in layers as this mismatch can be compensated more efficiently by elastic relaxation. [82,83]

3. Experiment

A number of different experimental methods have been used in the framework of this thesis. They will be presented in this chapter. First of all, a brief introduction to the preparation of the investigated NW samples will be given, including NW growth and dispersion as well as details of the NW morphology. In the second part, the experimental setups will be described. Particular attention is paid to µPL spectroscopy, as the majority of the PL experiments have been performed using a µPL setup. Other techniques described are standard PL, time-resolved PL, and Raman spectroscopy and x-ray diffractometry.

3.1. Nanowire growth

For the synthesis of NWs, several different techniques have been demonstrated.[6,84,85] The NWs investigated in this work are fabricated using a "bottom-up" approach. All of the GaN and GaAs NWs are grown by plasma-assisted molecular beam epitaxy (PAMBE), while the ZnO NWs are grown by metal-organic chemical vapor deposition (MOCVD). In the following, the growth mechanisms and the general growth conditions are outlined.

Nanowire growth mechanisms in molecular beam epitaxy

The vapor-liquid-solid (VLS) mechanism[86] is widely used to synthesize III-V semiconductor NWs. The metal-assisted growth of GaAs NWs[87] is illustrated in Fig. 3.1. Impinging Ga and As adatoms are collected by liquid nanometer-sized metallic seed particles[a] residing on a substrate. The seed particle acts as an effective sink for both, directly impinging as well as diffusing Ga adatoms. Eventually, the formed eutectic alloy supersaturates, and the semiconductor compound precipitates at the interface of the seed particle and the wafer. As a result, a crystal grows below the seed particle in vertical direction, i.e., a NW forms with the seed particle residing on top. Growth occurs under As rich conditions and is globally limited by the supplied amount of Ga. The diameter and the position of the NWs are determined by the seed particles. Controlling the seed particles thus is a means to control the size and the arrangement of the NWs.

The majority of GaAs NWs are grown using a foreign element as the seed, typically Au. However, it is also possible to grow self-assisted GaAs NWs as shown by Fontcuberta *et al.*[88] and Breuer *et al.*[42] using Ga as the seed. While the basic mechanism is the same, the process parameters have to be adjusted. For instance, the optimum growth temperature for self-assisted is higher than for Au-assisted GaAs NWs.

The growth of GaN NWs by molecular beam epitaxy (MBE) is more complex and not as well understood. In contrast to GaAs NWs, GaN NWs form spontaneously and do

---

[a]In conventional crystal growing, the term "seed particle" denotes a solid particle with a well defined crystal structure. Strictly speaking the use of this term is incorrect and "collector particle" should be used instead. However, "seed particle" is commonly found in the literature, and therefore, this term will be used here as well.
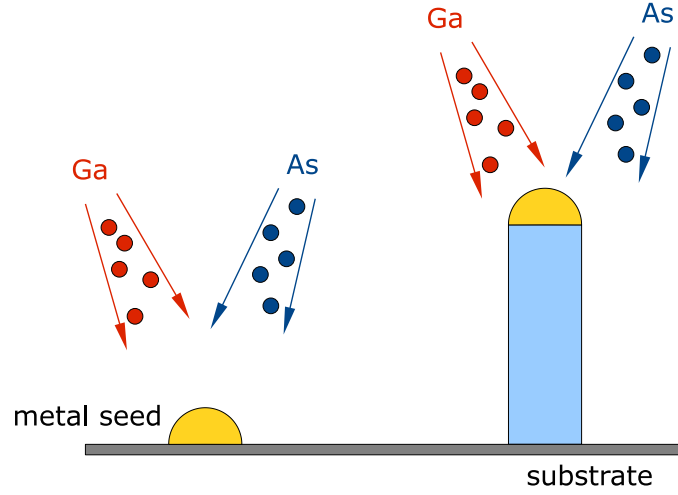
Figure 3.1.: Illustration of the VLS mechanism. The liquid metal seed (yellow) collects impinging Ga (red) and As (dark blue) adatoms. When the seed supersaturates, GaAs precipitates at the substrate surface, and the NW (light blue) grows under the seed.

not require the use of metallic seed particles. A V/III ratio larger than one is necessary to achieve NW growth. Ga adatoms are adsorbed on the substrate, where they either diffuse or desorb. The desorption rate strongly depends on the substrate temperature. If it is lower than the adsorption rate, the Ga atoms will eventually form clusters on the substrate, at which N atoms will bond. Once nuclei above the critical size have formed, the resulting GaN islands undergo several shape transitions from flat islands via pyramids and truncated pyramids, until finally NWs grow vertically.[21,89] Additional Ga atoms, that either directly impinge on the NWs or diffuse via the substrate to the NWs, preferably diffuse along the NW sidewalls to the top facets such that vertical growth is promoted.

Nanowire growth and morphology

An overview of the growth conditions and the morphology of all NW samples studied in this thesis can be found in Tab. A.1 in App. A. All GaAs NWs have been grown on Si(111) substrates at a temperature of around $500\,°C$ and a V/III flux ratio of around 2 for Au-assisted GaAs NWs. Self-assisted GaAs NWs are grown at a higher temperature of around $580\,°C$ and a lower V/III flux ratio of around 1. As nonradiative surface recombination significantly reduces the PL intensity of bare GaAs NWs, most of the samples are surrounded with an (Al,Ga)As shell with a nominal Al content of 10%. The NW density is rather low, ranging from 10^8 to $10^9\,\text{cm}^{-2}$. Diameters [including the optional (Al,Ga)As shell] range from 40 to $150\,\text{nm}$, while the NWs have a length between 2 and $9\,\mu\text{m}$. The GaAs NWs have been grown by S. Breuer at the PAUL-DRUDE-INSTITUTE, Berlin.

The GaN NWs investigated here have been synthesized in three different MBE chambers on either Si(001) or Si(111) substrates. All samples are grown at temperatures between 720 and $820\,°C$ under highly N-rich growth conditions, similar to the conditions reported by other groups.[5,90] Scanning electron microscopy (SEM) images of a typical GaN ensemble are shown in Fig. 3.2. All samples investigated here are characterized by a high NW density of about $10^{10}\,\text{cm}^{-2}$. This density strongly depends on the growth
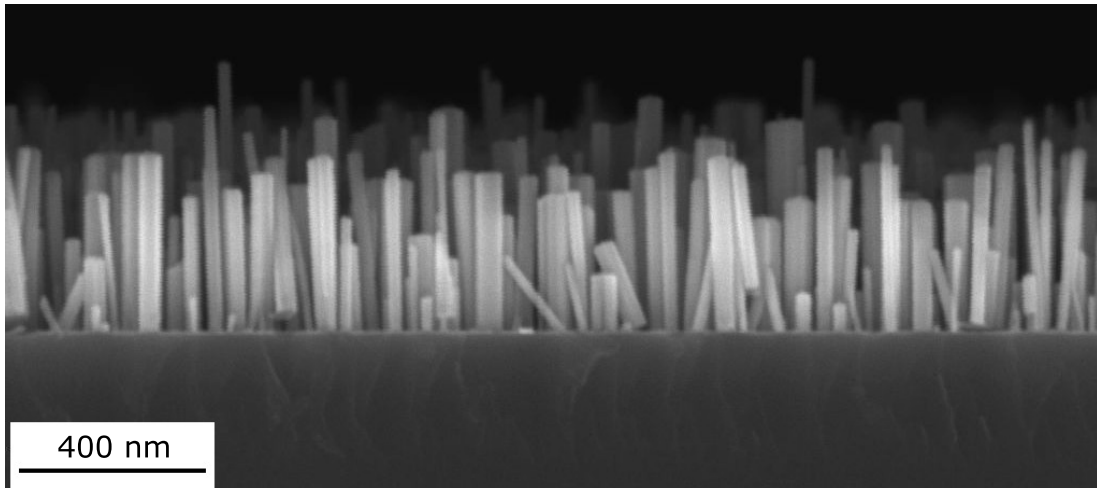
(a) Side view of a GaN NW ensemble.
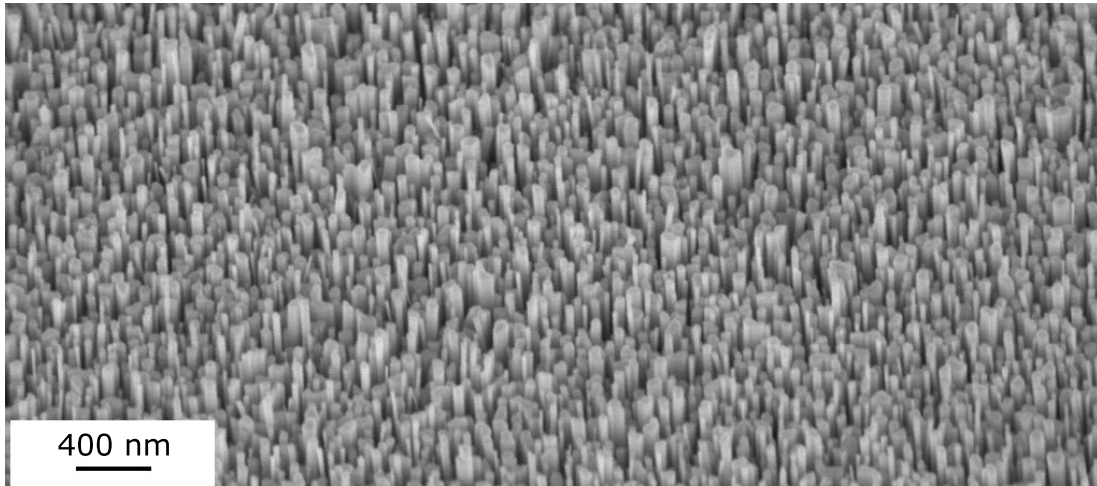
(b) Bird's view of a GaN NW ensemble.
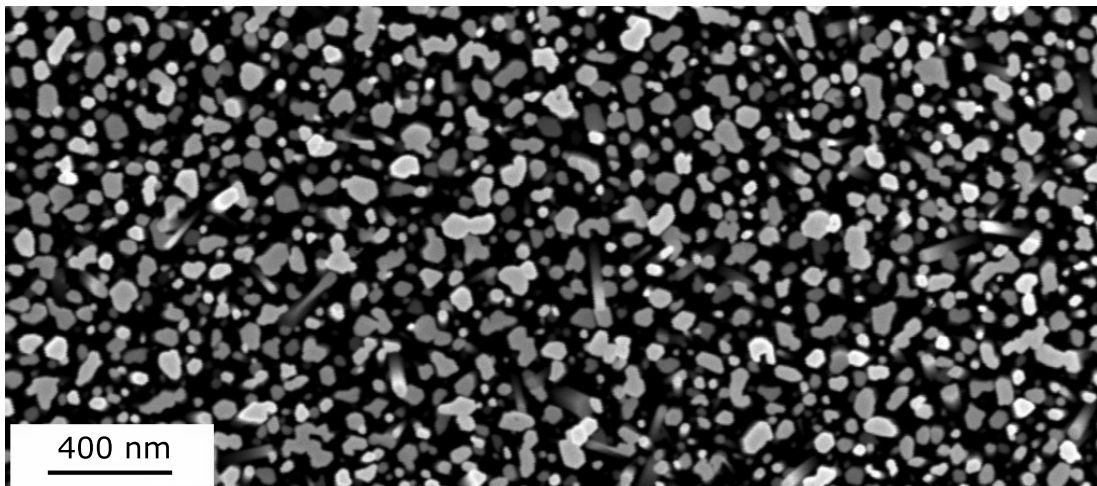
(c) Top view of a GaN NW ensemble.

Figure 3.2.: SEM images of a typical GaN NW ensemble (sample 30887) as investigated in this work. The images have been taken by C. Chèze.

temperature. With increasing temperature, Ga desorption is promoted, and thus, the nucleation density is reduced. In addition, the nucleation time varies strongly from nucleus to nucleus, resulting in a large length spread of the NWs. The GaN NWs have been grown by C. Chèze at INFINEON and QUIMONDA, Munich, and by V. Consonni, P. Dogan, M. Knelangen, and M. Wölz at the PAUL-DRUDE-INSTITUTE, Berlin.

Since nucleation is a statistical process, the distance between adjacent NWs varies. As a result, the amount of material available for a nucleus differs, and thus, statistical fluctuations in diameter and length occur. The NWs grow vertically in the *c*-direction. They may experience a slight tilt of a few degrees. The investigated NWs typically have diameters ranging from 20 to about 200 nm, with an average of about 40 nm. Diameters above 80 nm are typically caused by coalescence of neighboring NWs. The NW length is primarily governed by the growth rate and growth time. Typical values for the length of GaN NWs range from 400 nm to 2 μm. Non-coalesced NWs usually exhibit hexagonal cross sections with *M*-plane side facets and Ga-polar *C*-plane top facets.[91,92]

In contrast to the GaAs and GaN NWs, the ZnO NWs are grown by MOCVD on Si, Al_2O_3, and ZnO substrates. Growth is performed at temperatures from 550 to 615 °C with VI/II ratios ranging from 290 to 39 800. The NW length and diameter parameters are comparable to the ones of the GaN NWs, while their density, being on the order of 10^9 cm^{-2}, is slightly lower. The morphology of the ZnO NWs ranges from perpendicular growth with strong coalescence to randomly inclined NWs. The ZnO NWs have been grown by T. Ive at the UNIVERSITY OF CALIFORNIA, Santa Barbara.

Dispersion of nanowires

For the investigation of certain NW properties, it is helpful to characterize single NWs. Since the NW density in a NW ensemble is very high, e.g., 10^{10} cm^{-2} in the case of GaN NWs, optical techniques such as PL spectroscopy actually probe at least several hundred NWs simultaneously, if an ensemble is studied. Therefore, the single NWs have to be isolated, which can be achieved by several approaches:

Wet dispersion: A piece of a NW ensemble is placed in a solvent, e.g., isopropanol or acetone. The solution is then exposed to ultrasonic sound. Due to the vibration, NWs break off and float in the solvent, which are then dispersed on an empty wafer using a pipette. The NW density in the solution can be increased by scratching the sample with a scalpel prior to the ultrasonic bath. The density of isolated NWs on the carrier can also be adjusted by the amount of dispersed solvent. After evaporation of the solvent, the dispersed NWs can be examined. In the present work, this routine was applied to disperse GaN NWs on Si(111) substrates using isopropanol as solvent.

Scratching: Using a scalpel, NWs can be scraped off of a wafer. They are then transfered to an empty wafer by sliding the scalpel along its surface. The density of isolated NWs is, however, difficult to adjust. Depending on the hardness degree of the NW material, other tools such as cotton tips or tissues may be used.

Press and push: The NW ensemble is placed upside down on a bare wafer. Then it is pressed down and pushed into one direction. As a result, NWs will break off and stick to the empty wafer. Usually they are well aligned in the direction the sample was moved along. This method works well for GaAs NWs.

Depending on the length of the NWs, different means have to be applied to locate them. GaAs NWs, having typically a length of several µm, can be easily identified using an optical microscope. GaN NWs, which are often shorter than 1 µm, can be located only by using SEM. Therefore, markers are needed to retrieve the position of the dispersed NWs found by SEM. Here, a MAXTAFORM H7 finder grid is placed on the Si(111) wafer prior to the dispersion of the NWs.

3.2. Micro-photoluminescence

Experimental setup

Most experimental data presented in this work have been collected on a combined µPL and Raman setup (HORIBA JOBIN YVON LABRAM HR 800 UV). A schematic drawing of this setup is shown in Fig. 3.3(a). For optical excitation of large bandgap materials, the 325-nm line of a KIMMON IK 3552R-G HeCd laser with a maximum power of $I_0 = 30$ mW is used. Furthermore, the setup is equipped with a COHERENT IN-NOVA 301 Kr$^+$ laser and a MELLES GRIOT 25 LHR 925 HeNe laser. All of these lasers are continuous-wave lasers. Table 3.1 gives an overview of the available lasers and their common applications. A filter wheel equipped with a set of neutral density filters is used to reduce the excitation density by up to four orders of magnitude. An additional filter wheel with a continuously increasing optical density can be placed in the laser beam to vary the excitation density over a smaller range.

A microscope objective both focuses the laser onto the sample and collects the luminescence emitted by the sample (confocal design). The setup is equipped with a number of different objectives, which are either optimized for the UV range or for visible light. An overview of the microscope objectives is given in Tab. 3.2. With these objectives, the laser can be focused to a spot of 1 (100× objective) to 3 µm (15× objective). The latter one is used for the majority of experiments shown here. As it transmits UV light and has a large working distance, it is suitable for low-temperature PL experiments of GaN. In order to direct the laser beam into the microscope objective, either a notch or an edge filter is used. In Fig. 3.3(b), the transmittance of these filters is depicted schematically. Both are highly reflective at the laser wavelength, but transmit light of longer wavelengths. Behind this filter, the detection unit is located. Thus, the collected luminescence passes the notch or edge filter and is focused onto the entrance slit of the monochromator, while laser light reflected from the sample is efficiently blocked. The monochromator has a focal length of 80 cm and is equipped with two gratings (600 and 2 400 lines/mm), which spectrally disperse the signal onto a liquid-nitrogen (LN) cooled ISA SPECTRUM ONE charge-coupled device (CCD) camera with 1 024 × 256 pixels. Using the grating with 2 400 lines/mm, a spectral resolution of 0.25 Å (250 µeV in the UV range) is achieved.

For room-temperature experiments, the sample under investigation is placed on top of a cryostat, enabling the use of microscope objectives with a low working distance and a high magnification. For low-temperature measurements, the sample has to be placed inside a KRYOVAC cryostat on a cold finger, which can accommodate multiple samples at once. Using a turbo molecular pump by BALZERS, an isolating high vacuum (HV) of $10^{-5} - 10^{-6}$ mbar is created. The cold finger holding the samples can be cooled down with liquid helium to 10 K. In combination with a resistive heating element, the sample temperature can be adjusted continuously in the range from 10 to 325 K. The cryostat is placed on an x-y-stage, which allows for automated mapping of samples. The entire
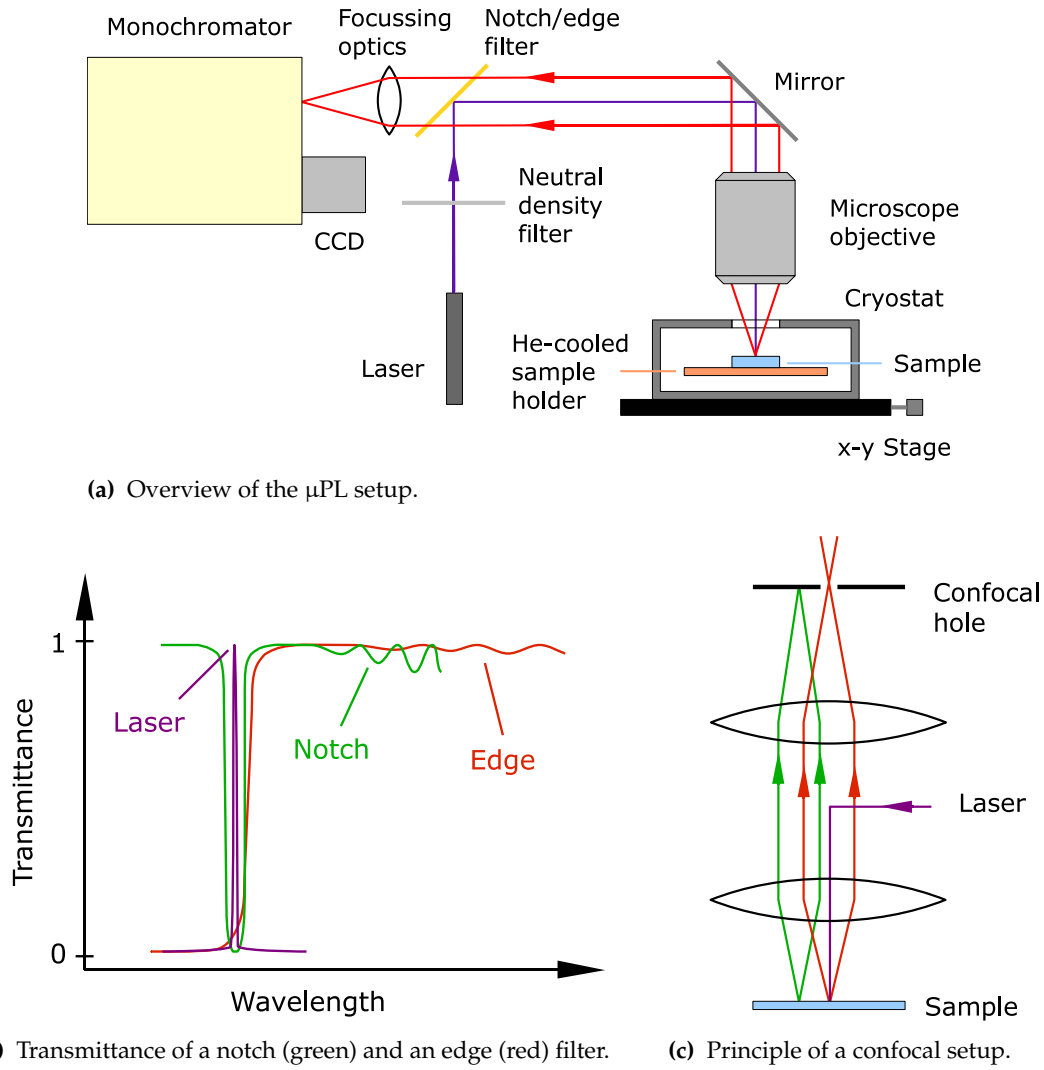
3. Experiment

(a) Overview of the µPL setup.

(b) Transmittance of a notch (green) and an edge (red) filter.

(c) Principle of a confocal setup.

Figure 3.3.: Schematic description of the µPL setup.

Table 3.1.: Overview of the lasers available at the µPL setup. Given are the laser wavelengths and energies as well as the materials whose PL is typically investigated with these lasers.

Laser type	Wavelength (nm)	Energy (eV)	Power (mW)	Material
HeCd	325.0	3.8149	30	GaN, ZnO, (Al,Ga)N, (In,Ga)N
Kr^+	413.0 482.5	3.0020 2.5696	100 30	(In,Ga)N
HeNe	632.8	1.9587	17	GaAs, (Al,Ga)As

Table 3.2.: Microscope objectives available at the µPL setup. Only microscope objectives with a working distance of more than 3 mm can be used for low-temperature experiments, for which the sample is placed inside the cryostat. VIS and IR denote the range of visible ($380 - 750$ nm) and infrared light, respectively.

	Magnification	Numerical aperture	Working distance (mm)	Wavelength range
1	15×	0.32	8.5	UV – VIS
2	40×	0.5	1	UV – VIS
3	50×	0.55	10	VIS – IR
4	100×	0.9	0.2	VIS – IR

detection system is controlled via the LABSPEC software.

As mentioned above, the µPL setup has a confocal design, i.e., the entrance slit of the monochromator acts as a circularly shaped aperture that defines the detection area on the sample. Figure 3.3(c) illustrates the principle of operation of the confocal design. The laser (violet line) is directed into the microscope objective and excites the sample at a specific position. Radiative recombination can take place at this very position (red lines) or after lateral diffusion of the excited carriers (green lines). The luminescence emitted after diffusion is blocked by the confocal aperture. The ratio of the aperture diameter and magnification of the microscope objective defines the region from which luminescence is collected. For the present work, lateral diffusion is prohibited by the very nature of the NWs. In general, the aperture is set to a diameter of 100 µm. The resulting area from which luminescence is collected thus covers the entire laser spot.

Ozone-cleaning procedure

The samples are mounted in the cryostat using an acetonic solution of conductive silver. The solvents basically consist of hydrocarbons, which are supposed to evaporate. However, a contamination of the samples with organic hydrocarbons is possible. The chemical bonds of these hydrocarbons are cracked by impinging UV light [or electron beams in cathodoluminescence (CL) spectroscopy] and an opaque substance consisting mainly of amorphous C is deposited on the sample surface. As a consequence, the intensity of the emitted light considerably decreases. In order to prevent the deposition of C, the O_3-cleaning procedure described in Ref. 93 is applied prior to the measurements. After closing the cryostat, the samples are illuminated for about 30 min with light from a Hg lamp. The 185-nm of the Hg spectrum is absorbed by O_2, leading to the formation of O_3. The 254-nm line of the Hg spectrum in turn is absorbed by O_3, and thus, O atoms are generated. These O atoms are strong oxidizing agents, which react with the organic hydrocarbons to CO_2, CO, H_2O, etc.[93]

Signal detection and processing

As the PL signal emitted from the sample under investigation is spectrally dispersed, the CCD camera records only a certain spectral range of the entire spectrum. Here, the angle of the grating as well as its groove density determine which part of the spectrum is detected. By adjusting the angle, different spectral sections can be recorded and are merged by LABSPEC to one spectrum. Thus, large spectral ranges can be investigated. Adjacent
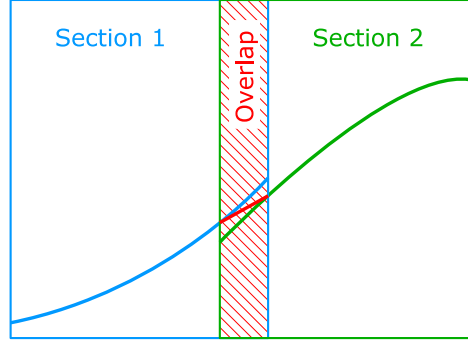
Figure 3.4.: Spectral sections are recorded individually and later on merged to one spectrum. In the overlap (red) region discrepancies between adjacent spectral sections are smoothed.

spectral sections are recorded with an overlap (see Fig. 3.4) to account for discrepancies in intensity at opposite sides of a spectral section. Such discrepancies can be caused by the CCD itself, but also by misaligned optics in the setup. The recorded PL spectra depict the intensity in counts/s vs. wavelength. In order to compare the absolute intensity of two samples, they either have to be probed side-by-side or their respective intensities have to be related via a reference sample.

For the analysis of recombination processes in semiconductors, the energy rather than the wavelength of the emitted photons is of interest, since it is the energy that is directly related to the fundamental physics. In contrast, the spectral dispersion of the PL signal using a grating correlates this signal to a wavelength λ. Therefore, λ is converted into an energy E using the following relation:

$$E[\text{eV}] = \frac{hc}{n_{\text{air}}\lambda} = \frac{1\,239.489}{\lambda[\text{nm}]} \, , \tag{3.1}$$

where $h = 4.13566733(10) \times 10^{-15}\,\text{eVs}$ is Planck's constant[94] and $c = 299\,792\,458\,\text{ms}^{-1}$ is the speed of light in vacuum.[94] The refractive index of air n_{air} depends on the wavelength of the light. In the near-band-edge region of GaN (around 360 nm), it is 1.000285,[95] yielding the conversion factor given in Eq. 3.1.

3.3. Additional experimental setups

Standard photoluminescence setup

While in a µPL setup the laser spot diameter is reduced to a few µm, in regular PL spectroscopy, (here referred to as MPL) the laser spot diameter is typically about one to two orders of magnitude larger. Consequently, the excitation density is considerably lower.

For a number of experiments, a MPL setup has been used, which is equipped with a KIMMON IK 3552R-G HeCd laser for UV applications. In addition, a COHERENT 890 tunable Ti:sapphire laser, which is optically pumped by a COHERENT VERDI V5 solid state laser, provides laser emission in the wavelength range from 700 to 850 nm. The MPL system is a bifocal setup, i.e., the focusing of the laser and the collection of the PL signal is achieved by two separate lenses. A minimum spot diameter of about 75 µm can be achieved. The signal is spectrally dispersed by two gratings with 600 1/mm in

a Horiba Jobin-Yvon U1000 double monochromator with a focal length of 1 m. For signal detection, a LN cooled Symphony Spectrum One CCD camera is used. The sample is placed on a cold finger inside an Oxford cryostat, which is cooled by liquid helium. An Oxford ITC4 temperature controller allows to adjust the temperature in the range from 10 to 400 K via a resistive heater.

An advantage of this system over the µPL setup is the more stable temperature control, in particular at higher temperatures. The spectral resolution of this setup is comparable to the one of the µPL setup. Depending on the application, the decreased excitation density may also be advantageous. Due to the large spot size, a larger number of NWs than in µPL is excited simultaneously, which allows for averaging over NW ensembles with a low NW density such as GaAs. However, fluctuations in the optical properties from NW to NW can only be observed with a considerably lower spot size as in the µPL setup.

Time-resolved photoluminescence setup

Time-resolved PL (TRPL) spectroscopy is a common technique to determine the recombination dynamics in semiconductors as described in Sec. 2.2. A TRPL setup differs from a continuous-wave PL (cw-PL) setup in two major respects. First, a pulsed laser is required. Second, on the detection side, an appropriate temporal resolution must be realized. Furthermore, the detection has to be synchronized with the excitation. While in cw-PL spectroscopy two-dimensional arrays (typically intensity vs. wavelength) are acquired, a third coordinate, namely the time, is added in TRPL spectroscopy.

For the TRPL experiments in the UV range, a femtosecond Coherent Mira 900 Ti:sapphire laser is pumped by a Verdi V10 solid-state laser. The Ti:sapphire laser with a tunable wavelength pumps in turn an Coherent Mira optical parametric oscillator. Its second harmonic having a wavelength of 325 nm is used for excitation of wide-bandgap materials such as GaN and ZnO. For the excitation of the GaAs samples, the wavelength of the Ti:sapphire laser is set to 740 nm. In all cases, pulses have a duration of 200 fs at a repetition rate of 76 MHz. The PL signal is dispersed in a 22-cm Horiba Jobin Yvon Spex 1681 spectrometer and detected by a Hamamatsu C5680 streak camera. The system has a spectral resolution of 2 nm and a temporal resolution of less than 2 ps.

The spectral resolution of the µPL setup is considerably higher than the one of the TRPL setup. Consequently, individual transitions, which can be distinguished in µPL spectra, may not be resolved spectrally in the TRPL measurements. The transients may thus comprise contributions from distinct transitions, which have different lifetimes.

Raman spectroscopy

The scattering of light in solids allows for the investigation of various properties of a semiconductor such as crystal structure, strain state, and carrier concentration. The scattering of light may also be used to study the coupling of light with a semiconductor structure. Incident photons are scattered elastically (Rayleigh scattering) or inelastically (Raman scattering) under the emission (Stokes) or absorption (anti-Stokes) of a phonon.[b] In crystals, only discrete Raman modes with characteristic energies are allowed. The phonon dispersion consists of acoustical and, if the crystal's unit cell contains two or more atoms, optical phonon branches. In this work, the intensity and energy of optical

---

[b]The quantum mechanical description of a lattice vibration is denoted as phonon. Phonons are delocalized quasiparticles existing in the entire crystal volume.

Table 3.3.: Overview of the allowed Raman modes in wurtzite GaN.[96] The experiments are performed in backscattering geometry. Here, the z-direction is parallel to the c-axis, considering c-plane GaN layers or NW ensembles. The polarization of the incoming and scattered light is given by the term in the brackets, with $z(y,y)\bar{z}$ and $z(y,x)\bar{z}$ denoting polarized and depolarized configuration of our setup, respectively.

Configuration	Allowed modes
$x(y,y)\bar{x}$	$A_1(TO)$, E_2
$x(z,z)\bar{x}$	$A_1(TO)$
$x(z,y)\bar{x}$	$E_1(TO)$
$x(y,z)y$	$E_1(TO)$, $E_1(LO)$
$x(y,y)z$	E_2
$z(y,x)\bar{z}$	E_2
$z(y,y)\bar{z}$	$A_1(LO)$, E_2

phonons [transversal (TO) and LO phonons as well as mixed states of those such as the E_2 phonon] of GaN NWs have been examined. From the position of the E_2 phonon, the strain state of the NWs is determined, and the intensity of the E_2 phonon Raman line is used to estimate the extraction efficiency of NWs. The selection rules for optical phonon modes in wurtzite crystals listed in Tab. 3.3 are used to investigate the coupling of light with the NWs.

Raman experiments have been performed at the combined μPL and Raman setup described in Sec. 3.2. As the energy of Raman-scattered photons differs only by several meV from that of the incident photons, Raman spectra are recorded close to the laser wavelength. Therefore, it is of vital importance to efficiently filter elastically scattered photons, i.e., light of the laser wavelength from the collected signal, since it otherwise would dominate the usually relatively weak Raman signal. Hence, the notch filter shown in Fig. 3.3(a) is used for Raman experiments, as its transmittance at the laser wavelength is much lower and its transmission edge is steeper than those of the edge filter [cf. Fig. 3.3(b)]. The spectral resolution of the setup is limited to about $1\,\mathrm{cm}^{-1}$.

The polarization orientation of the incident laser light is controlled with a Fresnel rhomb. Using a linear polarizer for the Raman signal, the allowed modes listed in Tab. 3.3 can be studied. At the combined μPL and Raman setup, the experiments are performed in backscattering geometry, i.e., the z-direction is parallel to the c-axis of a c-plane GaN layer.

X-ray diffractometry

X-ray diffractometry (XRD) is used here to determine the lattice constant of the material constituting the NWs. The wavelength λ of x-rays is on the same order as the lattice constant. Hence, the crystal acts as a grating, and the radiation is diffracted under a certain angle θ determined by Bragg's law:

$$\lambda = 2d_{\mathrm{hkl}} \sin \theta \,, \tag{3.2}$$

where d_{hkl} is the distance between adjacent lattice planes. From the lattice parameters of a crystal, its strain state can be determined.

The samples are mounted to a high-precision goniometer. By rotation of the sample, the angle ω of the incident beam is altered. Under an angle of 2θ with respect to the incident beam, the signal is detected. $\omega - 2\theta$-scans of GaN NWs have been performed to obtain the lattice constant in c-direction. For these scans, an analyzer in front of the detector is used to increase the angular resolution. Here, only symmetric reflexes ($\omega = \theta$) are studied. In addition, ω-scans, of GaN NWs have been conducted. The direction of these scans is in **k**-space perpendicular to that of $\omega - 2\theta$-scans, and thus, the out-of-plane distribution of the NWs can be measured to investigate their tilt.

XRD measurements are performed in a PANALYTICAL X'PERT PRO MRD diffractometer. The characteristic K_{α_1} Cu line, with a wavelength of 1.54056 Å, is used to irradiate the sample. The linewidth of this line is reduced by a Ge220 monochromator with a resolution of $\Delta\lambda/\lambda = 3 \times 10^{-4}$.

4. The effects of selected growth issues on the optical properties of nanowires

A number of exciting characteristics are attributed to semiconductor NWs, such as their strain-free nature and high material quality. The for that reason expected superior optical and electrical properties often serve as a motivation for the fabrication of NWs, nourished by the vision of NWs acting as building blocks for future nanometer-scaled devices.[16,19,97,98] In order to meet these expectations, NWs of high material quality are required, a property that is often taken for granted. In the present chapter, some of these, usually considered as given, exciting characteristics are tested. Two key issues of NW fabrication, the seed used for NW nucleation and the substrate the NWs are grown on, are explored in an exemplary way. In the first part, the effect of the seed particles on the optical properties of NWs is investigated by comparing Au-induced and Ga-assisted[a] GaAs/(Al,Ga)As core-shell NWs. The respective results are reported in Ref. 99. In the second part, the optical quality of ZnO NWs grown on different substrates is studied in order to determine the influence of the substrate. The results of this study are reported in Ref. 100.

4.1. Catalyst-induced vs. self-assisted nanowires

The growth of III-V or II-VI NWs is often initiated by seed particles of foreign species such as Au (cf. the VLS mechanism in Sec. 3.1). Here, the effect of foreign atoms on the optical properties of GaAs/(Al,Ga)As core-shell NWs is investigated by comparing the time-integrated and the time-resolved PL of Au-assisted (sample M6939) and self-assisted NWs (sample M6967). Figure 4.1 shows representative SEM images of the two samples. The average diameter of the Au-assisted NWs is around 60 nm. The upper parts of these NWs is conically tapered with a Au droplet, which is too small to be visible by SEM, residing on their tip. In contrast, the self-assisted NWs grow vertically with an average diameter of 150 nm and a clearly visible Ga droplet on top. Their density is lower than the one of the Au-assisted NWs. Table 4.1 gives a brief overview of the growth conditions and the NW morphology.

Optical characterization

Figure 4.2 compares the time-integrated and the time-resolved PL of self-assisted (green curve) with that of Au-assisted (red curve) GaAs/(Al,Ga)As core-shell NWs at room temperature.[99] The integrated PL intensity of sample M6967 is more than two orders of magnitude larger than the one of sample M6939 [see Fig. 4.2(a)]. The luminescence of the self-assisted NWs is dominated by a transition at 1.429 eV corresponding to band-to-band recombination of zincblende GaAs, while for the Au-assisted NWs a transition

---

[a]The term "self-assisted" is equivalent to "Ga-assisted", i.e., self-induced Ga droplets are used for the nucleation of NWs.

(a) Au-assisted GaAs/(Al,Ga)As core-shell NWs (sample M6939).

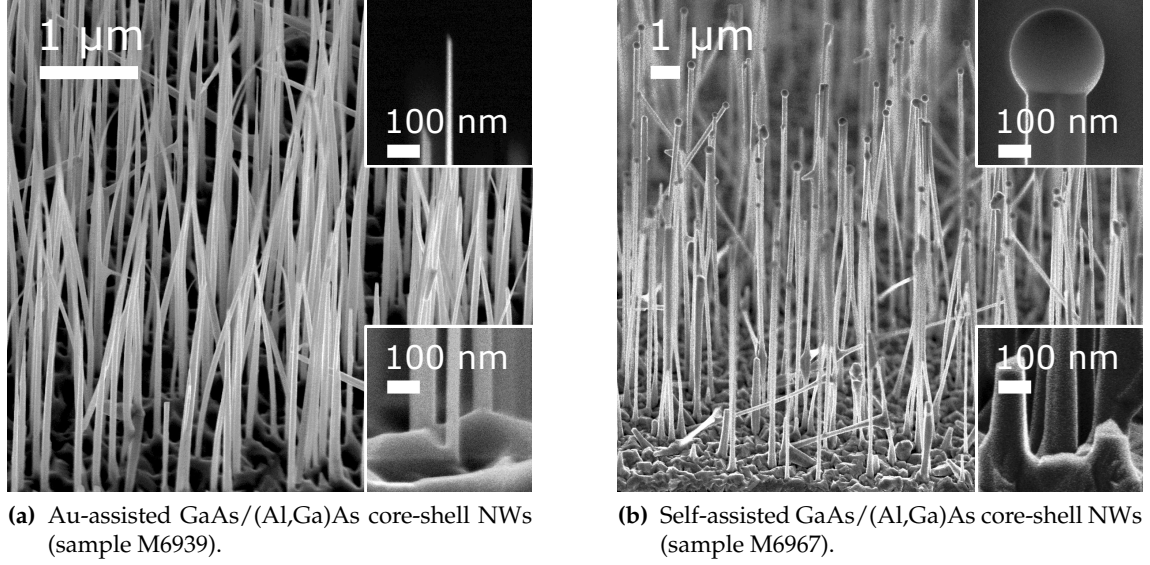**(b)** Self-assisted GaAs/(Al,Ga)As core-shell NWs (sample M6967).

Figure 4.1.: SEM images of Au-assisted (sample M6939) and self-assisted (sample M6967) GaAs/(Al,Ga)As core-shell NWs grown on Si(111) The insets show magnifications of the NW tips and of NW/substrate interfaces. The images have been taken by A.-K. Bluhm.

at 1.448 eV as in wurtzite GaAs is dominant. The presence of different crystal structures for the two growth modes is also reported in the literature.[47,101] In addition, the Au-assisted NWs exhibit a second transition at 1.525 eV originating from (Al,Ga)As with an Al content of about 6%.[55,102]

In Fig. 4.2(b), the PL transients of the two samples are shown. At room temperature, the recombination processes in GaAs are dominated by free-carrier recombination (see Sec. 2.2). From fits that consider both bimolecular radiative and monomolecular nonradiative recombination (see App. B), the carrier lifetimes can be determined.[99] For sample M6939 [see inset of Fig. 4.2(b)], a carrier lifetime of $\tau_{Au} = (9 \pm 1)\,\text{ps}$ is found. This lifetime is essentially identical to that reported for similar Au-assisted GaAs NWs.[103] For the self-assisted NWs, the transient exhibit an effective small-signal lifetime of $\tau_s = (2.5 \pm 0.1)\,\text{ns}$.[99]

In order to interpret the obtained lifetimes τ, the specific NW geometry has to be taken into account, in particular the large surface-to-volume ratio. Consequently, τ comprises recombination processes in the bulk-like part of the NW as well as recombination via the surface, or, in the case of core-shell NWs, via the core-shell interface:

$$\frac{1}{\tau} = \frac{1}{\tau_b} + \frac{4S}{d}\,, \tag{4.1}$$

with τ_b denoting the radiative bulk lifetime, S the surface or in this case interface recombination velocity, and d the NW or core diameter. Thus, the last term in Eq. 4.1 represents the nonradiative recombination at the NW surface. The factor 4 arises from the cylindrical geometry of the NWs.[104] By means of Eq. 4.1, the lifetimes obtained for samples M6939 and M6967 can be set in relation to state-of-the-art data of planar GaAs/(Al,Ga)As quantum wells. With $\tau_b = 0.8\,\mu\text{s}$ and $S = 250\,\text{cm/s}$,[105] a lifetime of approximately 4 to 10 ns is expected for GaAs/(Al,Ga)As core-shell NWs with a core diameter of 40 to 100 nm.

Table 4.1.: Brief overview of the growth conditions and morphology of the Au-assisted (sample M6939) and self-assisted (sample M6967) GaAs/(Al,Ga)As core-shell NWs.

Sample	M6939	M6967
Growth mechanism	Au-assisted	Self-assisted
Substrate temperature (°C)	500	580
Substrate	Si(111)	Si(111)
V/III flux ratio	2	1
NW density (cm^{-2})	5×10^8	1×10^8
Average NW length (nm)	5 000	9 000
Average NW diameter (nm)	60	150
Core diameter (nm)	40	100

Both τ_{Au} as well as τ_s thus represent nonradiative lifetimes. However, the value of τ_s is comparable to the lifetime expected for state-of-the-art material, while τ_{Au} is more than two orders of magnitude smaller than τ_s.

Temperature dependence

The discrepancies in lifetime (and thus internal quantum efficency) as well as in PL intensity reveal the presence of a highly efficient nonradiative recombination channel present only in the Au-assisted NWs. This effect cannot be explained by the different growth temperatures, since self-assisted GaAs/(Al,Ga)As core-shell NWs grown at 540 °C[b] show comparable lifetimes and PL intensities as sample M6967. Thus, the only plausible explanation for the observed discrepancies is the incorporation of Au into the NWs of sample M6939, which acts as a nonradiative recombination center. Although the solubility of Au in GaAs (2.5×10^{16} cm^{-3} at 900 °C) is rather low, a concentration on the order of 10^{16} cm^{-3} still corresponds to one Au atom within a length of 80 nm for NWs with a core diameter of 40 nm. Since the ambipolar diffusion length in GaAs has been measured to be about 0.7 μm[106], these Au atoms would be easily reached by free carriers and thus open up an efficient nonradiative recombination channel.

Such nonradiative recombination centers are often characterized by their thermal activation energy E_A. In fact, temperature-dependent measurements [shown in Fig. 4.3(a)] reveal that the difference in the PL intensities of the two samples considerable decreases at temperatures below 30 K. Furthermore, the lifetimes obtained at 10 K are almost identical taking values of $\tau_s(10\,K) = 5.0$ ns and $\tau_{Au}(10\,K) = 4.9$ ns.[99] The additional nonradiative recombination channel is thus thermally activated. The data shown in Fig. 4.3(a) have been recorded in the standard PL setup described in Sec. 3.3 with a low excitation power. The integrated PL intensity I_{PL} thus depends on the nonradiative lifetime as:

$$I_{PL} = \frac{I_0}{1 + \tau_r/\tau_{nr}} \tag{4.2}$$

---

[b]A direct comparison of self-assisted and Au-assisted GaAs/(Al,Ga)As core-shell NWs is not possible, as the growth temperature regime of the two growth modes does not overlap.
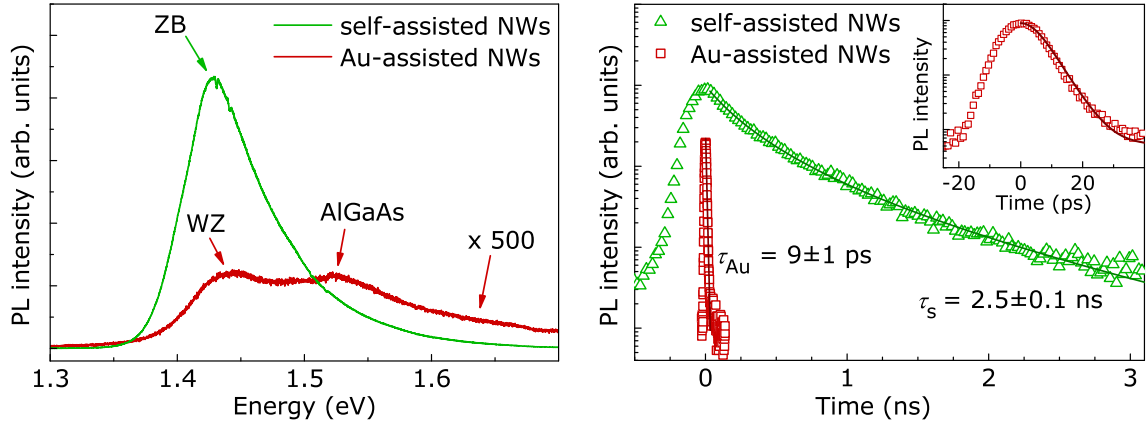
(a) Comparison of the PL spectra of samples M6939 and M6967. The spectrum of sample M6939 are increased by a factor of 500 and the main transitions are indicated. The spectra have been recorded by O. Brandt.

(b) Comparison of the PL transients of samples M6939 and M6967. The solid lines depict fits considering both bimolecular radiative and monomolecular nonradiative recombination processes. The inset shows the transient of sample M6939 with a higher temporal resolution. The transients have been recorded by T. Flissikowski.

Figure 4.2.: Comparison of the room-temperature PL of Au-assisted (sample M6939) and self-assisted (sample M6967) GaAs/(Al,Ga)As core-shell NWs.[99]

with I_0 being the extrapolated integrated intensity at $T = 0$. The thermally activated nonradiative lifetime is assumed to depend on the temperature T as:

$$\frac{1}{\tau_{nr}} = \frac{1}{\tau_{nr}^{\infty}} \exp\left(-\frac{E_A}{k_B T}\right),$$

(4.3)

where τ_{nr}^{∞} denotes the nonradiative lifetime at very high temperatures. The activation energy can be deduced from the slope of an Arrhenius-like plot as presented in Fig. 4.3(b) by converting Eq. 4.2 to:[107,108]

$$\ln\left(\frac{I_0}{I_{PL}(T)} - 1\right) = -\frac{E_A}{k_B T} + \ln\left(\frac{\tau_{nr}^{\infty}}{\tau_r}\right).$$

(4.4)

In the low-temperature range, both samples exhibit a similar behavior, reflected by an identical activation energy of (4.3 ± 0.1) meV. This activation energy represents the thermal dissociation of the FX, which has a binding energy of 4.2 meV in GaAs.[50] In contrast to neutral excitons, the dissociated carriers are subject to nonradiative recombination via charged defects, which explains the slight decrease in the PL intensity with decreasing temperature in the low-temperature range. At higher temperatures, only the Au-assisted NWs exhibit a second thermally activated process with an activation energy amounting to (77 ± 2) meV, substantiating the presence of a nonradiative recombination center. This recombination center is presumably related to Au atoms in the GaAs core as it is not found in the self-assisted NWs. However, the microscopic nature of this recombination center cannot be identified with the available data. In order to understand the evolution of the PL intensity of sample M6967, it should be noted that even at perfect GaAs/(Al,Ga)As interfaces, nonradiative recombination is present. Having a finite non-
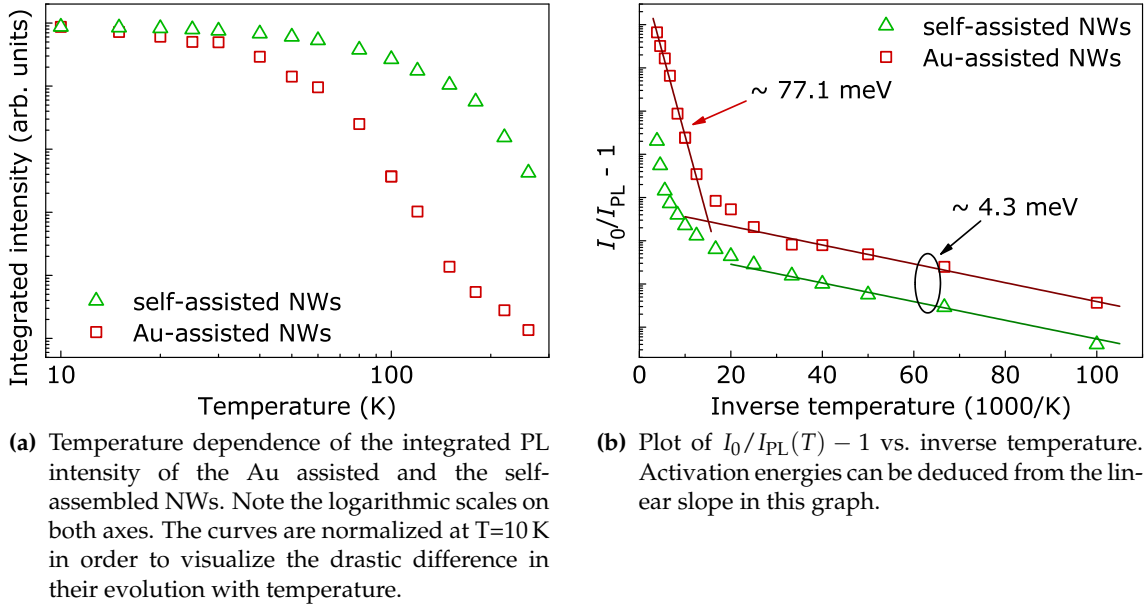
(a) Temperature dependence of the integrated PL intensity of the Au assisted and the self-assembled NWs. Note the logarithmic scales on both axes. The curves are normalized at T=10 K in order to visualize the drastic difference in their evolution with temperature.

(b) Plot of $I_0/I_{PL}(T) - 1$ vs. inverse temperature. Activation energies can be deduced from the linear slope in this graph.

Figure 4.3.: Temperature dependence of the PL intensity of samples M6939 and M6967.

radiative lifetime τ_{nr} and a temperature-dependent radiative lifetime $\tau_r \propto T^{3/2}$, the internal internal quantum efficiency η_{int} inevitably decreases with increasing temperature (cf. Eq. 2.19).

4.2. Nanowires grown on different substrates

The electrical and optical properties of a semiconductor layer largely depend on the substrate the layer is grown on. For example, the growth of GaN on substrates such as Al_2O_3 or Si leads to defective material due to the mismatch of lattice constants and thermal expansion coefficients. As a result, GaN layers grown on foreign substrates are often characterized by a high dislocation density and are under tensile or compressive strain. One of the major motivations for the growth of self-assembled semiconductor NWs is the expectation that it overcomes these limitations. Due to the small area of the NW/substrate interface, strain is effectively released (compare Sec. 2.4). Furthermore, extended defects such as threading dislocations are terminated by the nearby sidewalls. As a consequence, the major part of the NWs is free of strain and defects, and thus, their optical and electrical properties are expected to be independent of the underlying substrate. However, the experimental confirmation of this expectation is still lacking, probably to a large extent because it is rather difficult to grow NWs under comparable conditions on different substrates.

ZnO offers the possibility to synthesize self-assembled NWs heteroepitaxially on a range of different substrates. In addition, and in contrast to GaN, homoepitaxial growth of high-quality ZnO layers on commercially available ZnO substrates is possible. Here, we study the PL of three ZnO NW samples grown on different substrates and of a homoepitaxially grown ZnO layer. Samples 2, 3, and 5 are grown on Si(111), Al_2O_3, and ZnO, respectively. A brief overview of the growth conditions and morphology is given in Tab. 4.2. All ZnO NWs are of wurtzite structure. However, SEM images (see Fig. 4.4)

37

Table 4.2.: Brief overview of the growth conditions and morphology of the three ZnO NWs under investigation.

| Sample	2	3	5	layer
Substrate	Si(111)	Al_2O_3(0001)	ZnO(0001)	ZnO(0001)
Substrate temperature (°C)	615	550	550	1000
Average NW length (nm)	650	280	700	300
Average NW diameter (nm)	40	60	80	–
NW density (cm^{-2})	5×10^{-9}	5×10^{-9}	10^{-9}	–
Alignment	randomly inclined	perpendicular	perpendicular	–
Coalescence	partly	partly	strong	–

reveal remarkable differences in the morphology for the three NW samples. All samples exhibit a coalescence of adjacent NWs and even wall-like structures in sample 5. The NWs of sample 2 are randomly inclined, while the NWs of samples 3 and 5 are vertically aligned.

**Photoluminescence of ZnO NWs grown on different substrates**

The PL spectra at 10 K of the three samples are depicted in Fig. 4.5. Although the samples show strong differences in their morphology, their spectra are virtually identical in terms of energy, linewidth, and intensity of the observed transitions. All spectra are dominated by two distinct, sharp transitions at 3.3566 and 3.3597 eV, which are labeled according to the notation in Ref. 109 as I_9 and I_8, respectively. Accurate transition energies are obtained from high-resolution spectra of the near-band-edge region shown in Fig. 4.5(a). The two transitions are attributed to the recombination of excitons bound to neutral In and Ga donors. The presence of both species is due to parallel (In,Ga)N growth experiments in the same reactor, the NWs are grown in. Secondary ion mass spectrometry confirmed the presence of these two species in ZnO layers grown in the same system. Figure 4.5(a) shows in addition the luminescence of the ZnO reference layer. The layer PL (gray shaded area) is governed by the I_9 transition and shows additional weak lines at 3.3612 and 3.364 eV, which most likely represent the I_5 and I_3 transitions.[109] Due to the high resolution of the spectra shown in Fig. 4.5(a), not only the transition energies, but also the linewidths (see Tab. 4.3) of the I_9 and I_8 peaks can be precisely determined. With values ranging from 0.7 to 1.1 meV, they compare well with the narrowest linewidths reported for the luminescence of semiconductor NW ensembles.[110–112]

At 3.365 eV, an additional rather broad transition can be found in the PL of samples 3 and 5. This band is frequently observed in the PL of ZnO NWs and is ascribed to the recombination of surface excitons (SX),[113–115] i.e., excitons that are localized at surface centers originating from adsorbed particles. Note that the intensity of this transition increases with increasing diameter, a rather unexpected finding as the surface to volume ratio decreases at the same time.
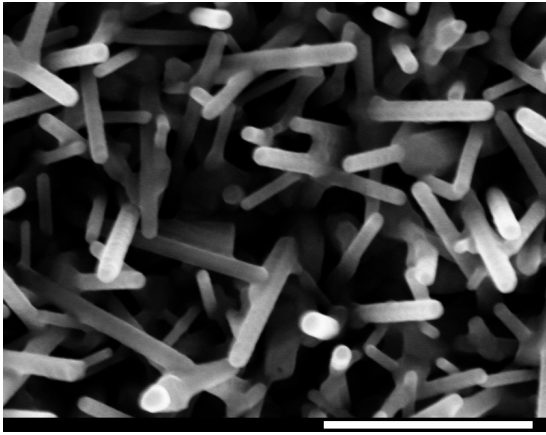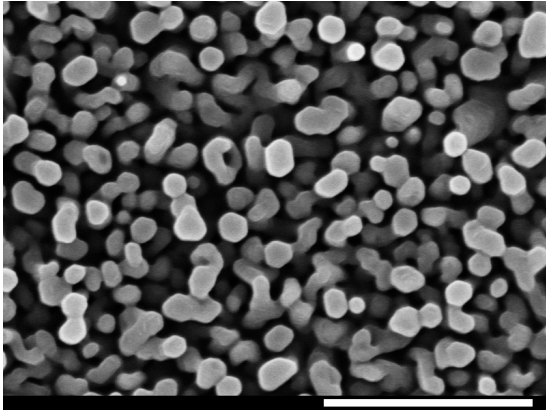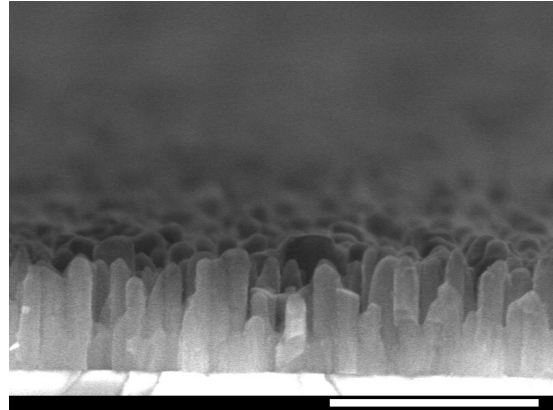
(a) SEM top view of sample 2 grown on Si.
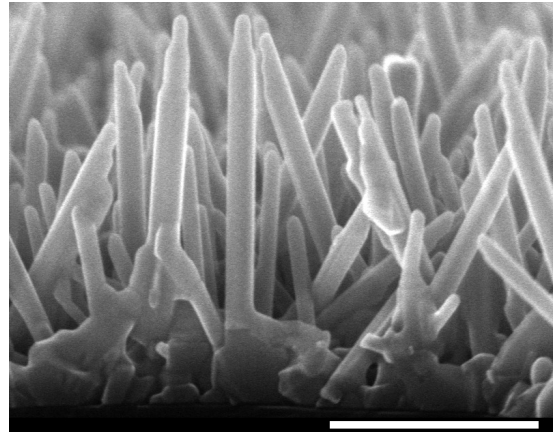
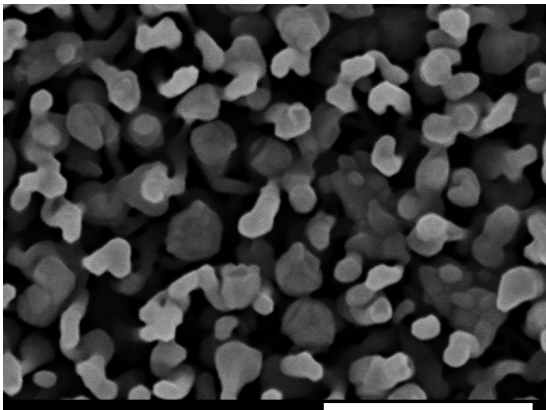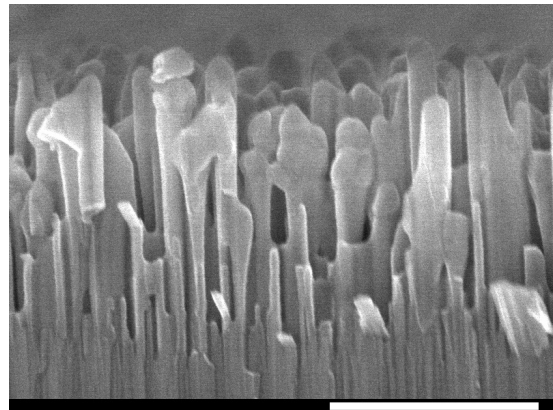**(b)** SEM side view of sample 2 grown on Si.

(c) SEM top view of sample 3 grown on Al_2O_3.

(d) SEM side view of sample 3 grown on Al_2O_3.

(e) SEM top view of sample 5 grown on ZnO.

(f) SEM side view of sample 5 grown on ZnO.

Figure 4.4.: SEM images of the three ZnO NW samples. The scale bars correspond to 500 nm. The images have been recorded by A.-K. Bluhm.

(a) Normalized high-resolution PL spectra of the near-band edge energy range. The spectra are compared to the PL of a layer grown in the same system on a ZnO substrate (gray shaded area).

(b) Logarithmic plot of the PL spectra of the three samples. The spectra are shifted vertically for clarity.
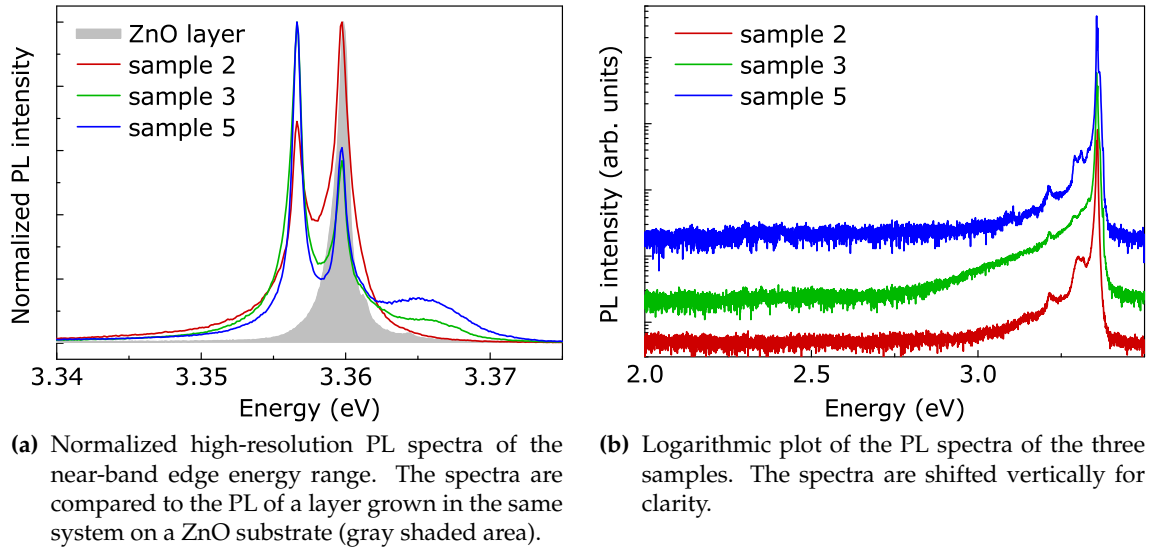
Figure 4.5.: PL spectra of the three ZnO NW samples. The experiments were performed at 10 K.

Table 4.3.: Overview of the parameters of the transitions dominating the ZnO NW PL spectra.

Sample		2	3	5
Substrate		Si	Al_2O_3	ZnO
I_9	energy (eV)	3.3566	3.3566	3.3566
	FWHM (meV)	0.7	0.9	0.8
I_8	energy (eV)	3.3597	3.3597	3.3597
	FWHM (meV)	1.1	0.8	0.8
SX	energy (eV)	–	3.365	3.365
1/e-decay time (ps)		310	240	240

Figure 4.5(b) shows a logarithmic plot of the NW PL spectra on a larger energy scale. In addition to the (D^0,X) transitions, their first and second order LO phonon replica can be observed at about 3.29 and 3.21 eV.[56] Furthermore, the TES of the (D^0,X) transitions appears at around 3.315 eV.[116] In the low-energy regime, no traces of green luminescence are present. This green luminescence around 2.5 eV[117] is commonly observed in ZnO layers and is attributed to native defects.[118]

The PL intensity of the three ZnO NW samples is almost exactly the same. According to Huygens' principle, the entire NW volume is excited. Considering the density, length, and diameter of the NWs, this volume is also almost the same for all samples. It should also be pointed out that the PL signal from the ZnO substrate used for the homoepitaxial growth of sample 5 differs significantly from the NW spectra confirming that the substrate does not contribute to the spectra shown in Fig. 4.5 (blue lines).
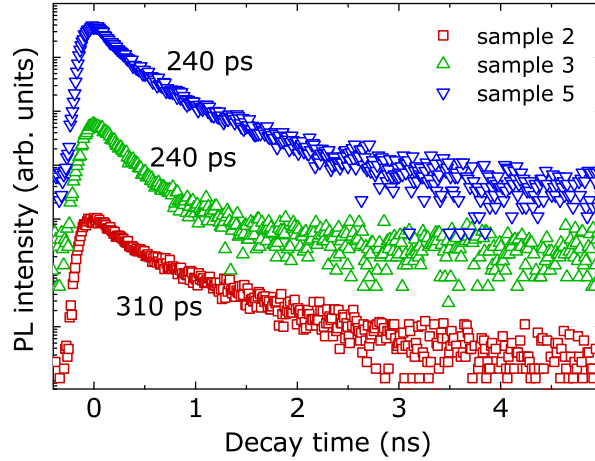
Figure 4.6.: Comparison of the PL transients of the three ZnO NW samples measured at 15 K. The 1/e-decay times are indicated in the figure. The graphs are shifted vertically for clarity. The transients have been recorded by T. Flissikowski.

Time-resolved photoluminescence of ZnO nanowires

Figure 4.6 depicts the PL transients of the three ZnO NW samples recorded at a temperature of 15 K. Due to the comparably low spectral resolution of the TRPL setup, the transients are integrated over the entire near-band-edge range. All samples show a clear non-exponential decay behavior, which is commonly observed for NW ensembles.[103,115,119] The respective 1/e-decay times of 310 ps (sample 2) and 240 ps (samples 3 and 5) are longer than values reported in the literature.[114,115,120,121] However, high-quality bulk ZnO exhibits lifetimes of about 1 ns.[56] The decay dynamics in the NWs are thus governed by nonradiative recombination, most likely via surface states.[120,121] With decreasing diameter, the influence of the surface decreases, and thus, decreasing decay times are expected. Our data, however, do not show a corresponding correlation. In addition, the intensity of the SX transition does not increase with decreasing NW diameter.

Nevertheless, the presented results underline that, in contrast to layers, the optical properties of ZnO NWs are largely independent of the applied substrate. Although their morphology differs, the investigated NWs exhibit almost no differences in their optical characteristics. That means, that their crystal quality is independent of the substrate properties. Therefore, the synthesis of NWs may indeed overcome the limitations that the mismatch of lattice constants and thermal expansion coefficients poses to the heteroepitaxial growth of layers.

4.3. Conclusions

Comparing the PL of Au- and self-induced GaAs/(Al,Ga)As core-shell NWs, it has been shown that the application of a foreign seed may severely affect the optical and electrical properties of the NWs. The incorporation of Au atoms into the GaAs NW cores results in the presence of a nonradiative, thermally activated recombination center, which degrades the optical properties of the NWs at room temperature. The application of Au-assisted NWs in optoelectronic devices is therefore rather disadvantageous, while self-assisted NWs are promising.

In contrast to the seed material, the substrate plays only a minor role for the optical

quality of ZnO NWs. As the comparison of ZnO NWs grown on three different substrates shows, NWs bear a significant advantage over layers: their optical quality is indeed not restricted by constraints related to the substrate such as structural, chemical, and thermal mismatch. Instead, the substrates may be chosen freely.

5. General optical properties of GaN nanowires

The crystal quality of GaN layers is in general limited by the substrate they are grown on. Usually GaN layers are grown on substrates with different lattice constants and thermal expansion coefficients. A consequence is the presence of strain and a high defect density in these layers.[122–124]

GaN NWs have been grown on a number of different substrates which exhibit a lattice mismatched.[5] Close to the substrate interface, a NW experiences strain. However, the major part of the NW is believed to be essentially free of strain. The large surface-to-volume ratio allows for an effective strain release within a short distance from the substrate, as the principle of St. Venant[79] states (cf. Sec. 2.4). The density of defects is also expected to be considerably lower in GaN NWs than in GaN layers. Threading dislocations forming at the NW/substrate interface are believed to be bent to the NW sidewalls,[10,125] and thus in general do not propagate along the entire NW length. Moreover, point defects such as impurities or vacancies may segregate to the NW surface during growth and therefore become inactive or simply disappear.[90,126]

The signature of both strain and defects can be detected by PL spectroscopy to a precision and sensitivity that exceeds those of most other methods. Therefore, PL spectroscopy is widely used to judge the crystal quality of NWs in general and GaN NWs in particular. The number of groups fabricating GaN NWs has increased constantly over the past decade. The majority of these groups focuses on the fabrication of devices, most of all LEDs based on GaN/(In,Ga)N or (Al,Ga)N/GaN NW heterostructures.[29,31,127–129] Despite the community's increasing interest in GaN NWs for optical application, only a few detailed studies on their fundamental optical or electrical characteristics have been published. The nature of the excitonic near-band edge luminescence and of the defect-related luminescence has been investigated by temperature- and excitation-density-dependent PL, CL, and TRPL spectroscopy[5,23,130,131] and has been related to the morphology and crystal quality of the NWs.[5] Defect-related PL peaks have been ascribed to structural defects and point defects such as impurities and native defects.[5,23] The broadening of the (D^0,X) transition observed in the PL spectra of single GaN NWs was interpreted as an indication for the presence of inhomogeneous strain.[130] Thillosen *et al.*[13] found as-grown GaN NWs to effectively release strain. The incorporation of donors and acceptors and their effects on the morphology and the optical properties of GaN NWs was studied by Furtmayr *et al.*[132]

Due to the large surface-to-volume ratio, surface-related effects are expected to significantly influence the optical and electrical properties of GaN NWs. Despite their importance, such effects have been largely ignored. The significance of nonradiative surface recombination in GaN has been demonstrated for the first time by diameter-dependent TRPL experiments of single GaN NWs.[104] Hsiao *et al.*[133] investigated the Raman signal of single GaN NWs and found evidence for surface modes. Furthermore, the electrical properties of GaN NWs have been investigated by Calarco *et al.*,[75] who concluded from photoconductance measurements that surface depletion significantly reduces the con-

(a) Comparison of the near-band-edge PL spectra of two GaN NW ensembles [sample 30887 (red) and sample M9257 (blue)] and a GaN layer [sample CBL 1043 (green)]. The orange line marks the position of the (D^0,X) transition in unstrained GaN. The measurements were performed at 10 K.

(b) Room-temperature PL spectra of a GaN NW ensemble (sample 30887) and of a GaN layer grown by MOCVD. The PL intensity is plotted on a logarithmic scale. The PL spectrum of the layer exhibits prominent thickness-interference fringes. This spectrum has been recorded by O. Brandt.
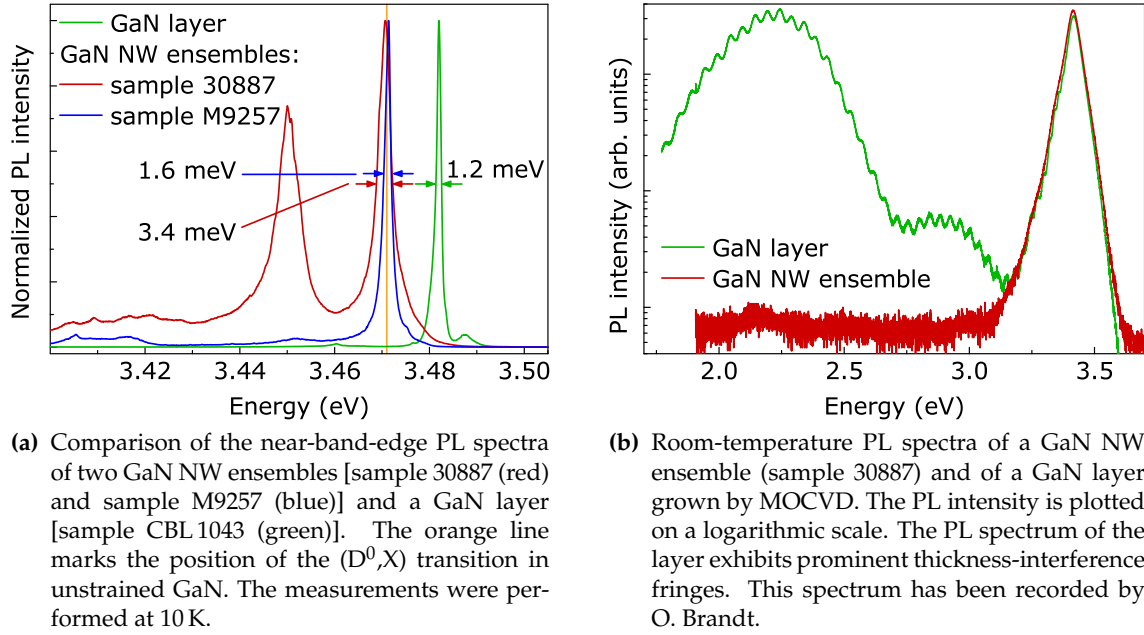
Figure 5.1.: Comparison of the PL of GaN NW ensembles and GaN layers.

ductance of GaN NWs.

Consequently, the recombination processes in GaN NWs are still poorly understood. In particular, the role of the nearby surface and its influence on the optical and electrical properties remains to be clarified. In the present chapter, a thorough investigation of the temperature and excitation density dependence of the PL of GaN NWs is presented and compared to equivalent measurements of GaN layers aiming at the identification of the major recombination channels. Typical characteristic features of GaN NW PL are discussed and the NWs are conclusively shown to be strain-free by PL and Raman spectroscopy and by x-ray diffractometry.

5.1. Photoluminescence of GaN nanowire ensembles

Figure 5.1(a) compares the near-band-edge PL spectra at a temperature of 10 K of two GaN NW ensembles (sample 30887 and sample M9257) and of a GaN layer grown on a sapphire substrate (sample CBL 1043). The NW samples are both grown by MBE on Si(111). The dominant transition of the PL of the NW ensembles can be found at 3.471 eV, the (D^0,X) recombination energy of unstrained GaN at 10 K.[134–136] This transition has a linewidth of 3.4 meV for standard GaN NWs and of 1.6 meV for the state-of-the-art sample.[a] In the PL of the layer, the (D^0,X) transition is blue-shifted, indicating that the material is compressively strained. The full width at half maximum (FWHM) of this transition amounts to 1.2 meV. The strain state of the NWs is discussed in more detail at the end of this chapter, while the relatively large linewidth of the (D^0,X) transition in the PL of the NW ensembles will be discussed in Chap. 6.

---

[a] At the time of writing this thesis, sample M9257 (grown at 820 °C) is our best GaN NW ensemble in terms of the linewidth of the (D^0,X) transition at 10 K. However, at the beginning of this work, sample 30887 (grown at 780 °C) was our state-of-the-art sample. Hence, most studies shown in this work have been performed using sample 30887. For detailed growth conditions, see App. A.

The transition at 3.45 eV observed in the PL spectrum of sample 30887 and less prominent also in that of sample M9257 is frequently reported for GaN NWs. Its origin has not been identified yet, but several possibilities have been discussed in the literature. On the one hand, this transition has been attributed to excitons bound to planar defects.[23,137] On the other hand, abundant point defects, such as surface defects, may act as excitonic recombination centers.[132] The TES of the (D^0,X) is found in this energy range and has been observed in the PL spectra of GaN layers.[135,138] However, its intensity is only a fraction of that of the (D^0,X) transition. In Sec. 9, the experimental results of this work regarding the 3.45 eV band will be discussed in more detail. As for now, it should be mentioned that the 3.45 eV transition is considered to originate from an unidentified excitonic complex and therefore will be referred to as (U,X).

A third luminescence band is centered at 3.42 eV. This band has been attributed to the recombination of excitons bound to intrinsic I_1 SFs,[46] which represents a zincblende insertion with a width of three monolayers.[45] These planar defects have been observed to develop when adjacent NWs coalesce.

A remarkable observation can be made in Fig. 5.1(b). Here, the room-temperature PL spectrum of a GaN layer grown by MOCVD is compared to that of a GaN NW ensemble (sample 30887). In the range of 2.0 to 3.0 eV, the GaN layer shows a broad PL band around 2.2 eV. This yellow PL is most likely caused by a transition between a shallow donor and a Ga vacancy[139] and is typical for GaN layers regardless of their provenience. In contrast, the NWs exhibit no PL in this range, suggesting a low density of native point defects in the NWs. Note that both samples exhibit a broad transition at 3.415 eV, which is attributed to FX recombination at room temperature.[138] The (U,X) transition seen in Fig. 5.1(a) is not resolved at this temperature due to thermal broadening of the FX line.

5.2. Temperature dependence of GaN nanowire luminescence

The temperature dependence of the normalized PL spectra of a GaN NW ensemble (sample M9257) is shown in Fig. 5.2(a). At low temperatures, the spectra are dominated by bound exciton emission. The (D^0,X_A) line at 3.471 eV, a minor (U,X) transition at 3.45 eV, and a weak SF luminescence at 3.42 eV are observed. In addition, a barely resolved line at 3.475 eV can be found, which probably represents the (D^0,X_B) transition. Free excitons at 3.479 eV however, are only visible on a logarithmic scale. At temperatures of 15 to 20 K, the FX_A line appears on the high energy side of the (D^0,X_A) line at 3.479 eV as higher lying states become thermally occupied. At an energy of 3.484 eV, the FX_B emerges and also the (D^0,X_B) becomes more prominent. With further increasing temperature, the free excitons dominate over the donor-bound exciton emission. This effect is explained by a thermally activated release of bound excitons from their defects. In addition, a significant thermal broadening of the luminescence is observed. PL spectra recorded at temperatures above 120 K are characterized by a single, broad FX transition. Figure 5.2(b) depicts the evolution of the recombination energies of the (D^0,X_A), (D^0,X_B), FX_A, and FX_B transitions with temperature, illustrating that at temperatures above 40 K the thermal shrinking of the bandgap sets in. As a result, a considerable redshift of the transition energies is observed. The temperature-dependent bandgap $E_G(T)$ is often described by Varshni's formula:[141]

$$E_G(T) = E_G(0) - \frac{\alpha_V T^2}{\beta + T},$$

(5.1)

(a) Normalized temperature-dependent PL spectra of sample M9257. The spectra are recorded in the temperature range from 10 to 160 K. The vertical lines serve as guide to the eye and denote the position of the (D^0,X_A) (orange), (D^0,X_B) (green), FX_A (blue), and FX_B (violet) transition.

(b) Evolution of the peak energy with temperature for the near-band-edge transitions observed in the NW PL in 5.2(a). The red line depicts the FX_A transition energy of unstrained GaN taken from Ref. 140.
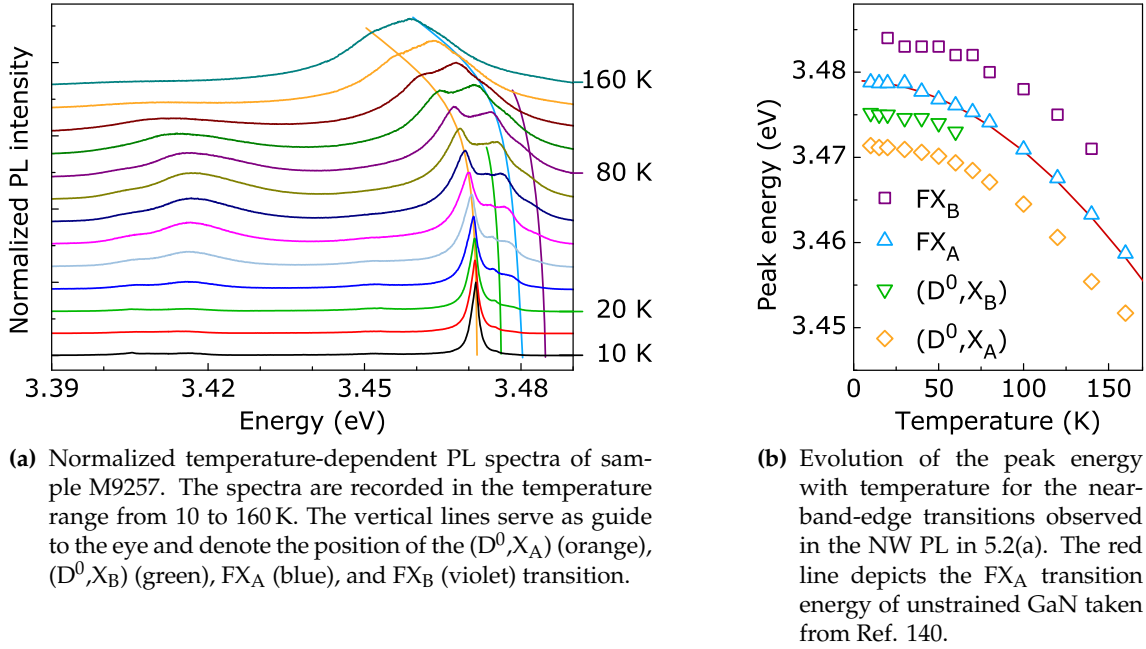
Figure 5.2.: Temperature-dependent PL spectra of a GaN NW ensemble (sample M9257). The spectra are recorded at an excitation power of $10^{-4}I_0$.

where $\alpha_V = -\partial E_G(T)/\partial T|_{T\to\infty}$ denotes the limiting slope at high temperatures and β is a phenomenological parameter with the dimension of a temperature.[140] However, Varshni's model is purely empirical and has no physical meaning. A physically motivated model taking into account the material-specific phonon dispersion has been developed by Pässler[140] (the derivation of this relation can be found in Ref. 142):

$$E_G(T) = E_G(0) - \frac{\alpha\Theta}{2}\left(\sqrt[4]{1 + \frac{\pi^2}{6}\left(\frac{2T}{\Theta}\right)^2 + \left(\frac{2T}{\Theta}\right)^4} - 1\right). \qquad (5.2)$$

Here, $\alpha = -\partial E_G(T)/\partial T|_{T\to\infty}$ again represents the limiting slope and Θ is the effective phonon temperature. The red line in Fig. 5.2(b) represents the evolution with temperature of the FX_A transition energy of *unstrained* GaN as given in Ref. 140. The FX_A transition of sample M9257 matches this evolution perfectly.

The evolution of the spectrally integrated PL intensity with temperature is depicted in a double-logarithmic plot in Fig. 5.3(a). A pronounced decrease of PL intensity I_{PL} with increasing temperature due to an enhanced nonradiative recombination rate is observed. Using Eq. 2.19, I_{PL} is given by:

$$I_{PL}(T) = \eta_{int}(T)I_{PL}(0) \qquad \text{with} \qquad \eta_{int}(T) = \frac{1}{\tau_r(T)/\tau_{nr}(T) + 1}. \qquad (5.3)$$

The internal quantum efficiency $\eta_{int}(0) = 1$. If a thermally activated nonradiative recombination center is present, the nonradiative recombination time $\tau_{nr}(T)$ is proportional to $\exp[E_A/(k_B T)]$. E_A denotes the activation energy of the nonradiative recombination center, which, in an Arrhenius plot, can be obtained from the slope of the data at high temperatures (cf. the analysis in Sec. 4.1). On the left-hand side of Fig. 5.3(b) such an

(a) Evolution of the integrated PL intensity with temperature for the GaN NW ensemble and a GaN layer (sample CBL 1043). The numbers given in the graph represent the respective exponents b from Eq. 5.4.

(b) The graph on the left hand side shows the integrated PL intensity data in the Arrhenius plot. The blue and violet line represent fits that take into account one or two thermally activated nonradiative recombination channels, respectively. On the right-hand side, the very same data and fits are plotted in a double logarithmic graph. The black circles mark the discrepancies between data and fit curves.

Figure 5.3.: Evolution of the spectrally integrated PL intensity of a GaN NW ensemble (sample 30887) with temperature. The measurements were recorded at the MPL setup with an excitation density of about $1\,\mathrm{kW/cm^2}$.

Arrhenius plot and the fit of the data according to the above relation is depicted for one (blue) and two (violet) thermally activated recombination centers. While in this plot, the fits appear to be reasonable, systematic discrepancies become apparent at high temperatures when the same data and fit curves are plotted in a double logarithmic graph [right-hand side of Fig. 5.3(b)]. Hence, the decrease of the PL intensity is not caused by such a thermally activated nonradiative recombination center. Instead, we assume that $\tau_\mathrm{r}(T) \propto T^{3/2}$ and we describe $\eta_\mathrm{int}(T)$ with a function that can be approximated by a power law at high temperatures:

$$I_\mathrm{PL}(T) = \frac{I_\mathrm{PL}(0)}{(aT)^{3/2+b} + 1}, \tag{5.4}$$

with the three fitting parameters $I_\mathrm{PL}(0)$, a, and b. In this presentation, the pre-factor a is a not further identified inverse temperature and the exponent b describes the temperature dependence of the nonradiative recombination processes.

The solid lines in Fig. 5.3(a) show least-square fits of Eq. 5.4 to the data for the integrated PL intensities of the GaN layer and of the GaN NWs with the fitting parameters $b_\mathrm{L} = 0.38 \pm 0.04$ for the layer and $b_\mathrm{NW} = 0.23 \pm 0.05$ for the NWs. As this exponent describes the temperature dependence of the nonradiative recombination channels in the two different samples, the differences between b_L and b_NW imply that at elevated temperatures different nonradiative recombination mechanisms are present in the two samples.

(a) Evolution of the normalized PL spectrum of sample M9257 with excitation power. The spectra are shifted vertically for clarity. The vertical lines denote the position of the (D^0,X_A) (orange), (D^0,X_B) (green), and FX_A (blue) transition.

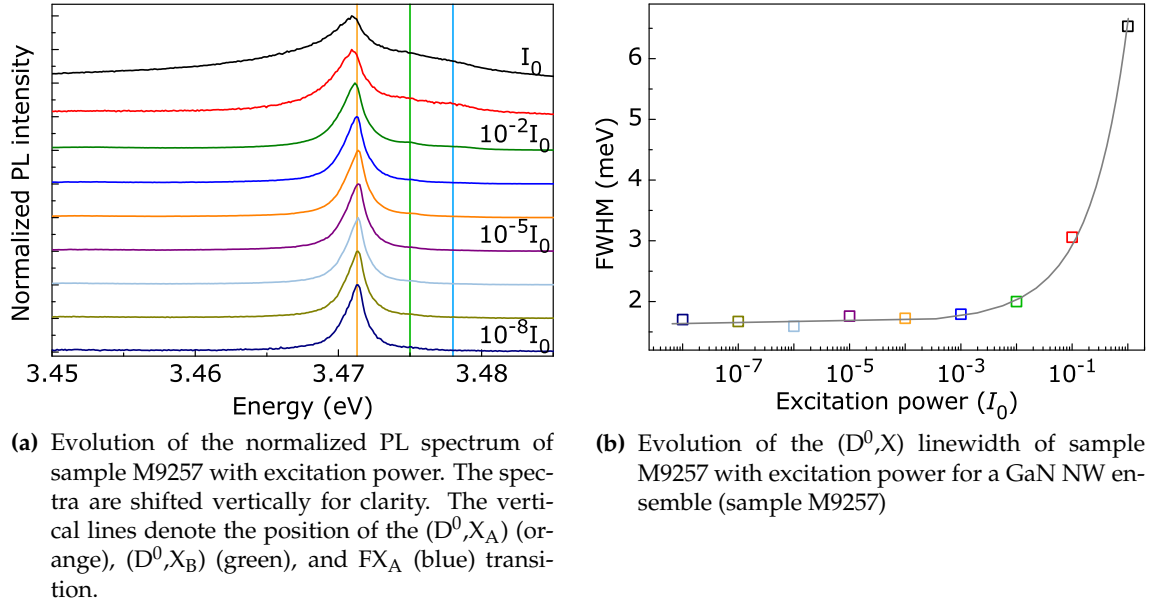**(b)** Evolution of the (D^0,X) linewidth of sample M9257 with excitation power for a GaN NW ensemble (sample M9257)

Figure 5.4.: Excitation-power-dependent measurements of a GaN NW ensemble (sample M9257). The spectra are recorded at a temperature of 10 K.

5.3. Excitation density dependence of GaN nanowire photoluminescence

The relative intensity and the FWHM of a radiative transition depend on the excitation density. Figure 5.4(a) shows the normalized PL spectra of sample M9257 for different excitation powers, covering eight orders of magnitude. For all excitation powers, the PL spectra are dominated by the (D^0,X_A) transition at 3.471 eV. For low excitation levels, the normalized spectra compare well. Only at excitation densities higher than $10^{-2}I_0$, the linewidth rapidly broadens from less than 2 meV to more than 6 meV as shown in Fig. 5.4(b), and at the high energy side, the (D^0,X_B) and the FX_A become visible.[143]

Plotting the integrated PL intensity versus excitation density may give insights on the participation of nonradiative recombination when examining the slope of the curve in a double-logarithmic plot. Figure 5.5 shows the integrated room-temperature PL intensity of a GaN NW ensemble (sample 30887) compared to that of a GaN layer (sample CBL 1043). In an ideal sample with internal quantum efficiency of one the recombination processes are purely radiative, and thus, the dependence of the *integrated* PL intensity on the excitation density is linear. Consequently, this curve has a slope of one in a double-logarithmic plot. If a nonradiative recombination channel is introduced, the slope would still be one as long as the experiment is performed in the low excitation density range, where, according to Eqs. B.12 and B.14 in App. B the radiative and nonradiative recombination rates scale linearly with excitation density. As a result, the radiative and nonradiative recombination channels compete with each other. This can be observed in the PL of the GaN layer for low excitation densities. At a certain excitation density, however, radiative recombination takes over as described by Eqs. B.17 and B.19 and Fig. B.1 in App. B. As a result, the excitation density dependence becomes superlinear for higher excitation densities. In the excitation density dependence of sample 30887, a linear region can be found at medium excitation densities, where radiative and nonradiative recombination
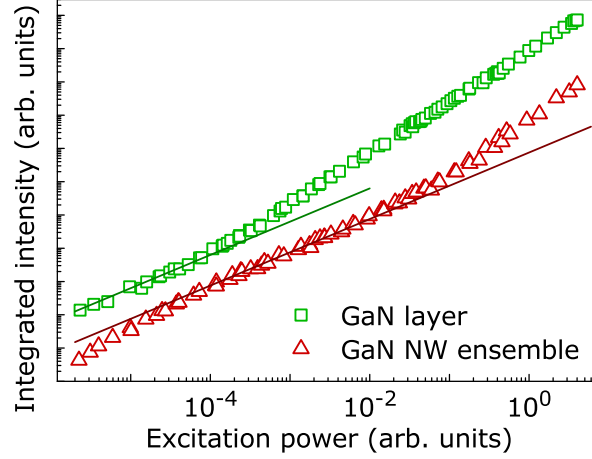
Figure 5.5.: Comparison of the room-temperature PL intensity evolution with excitation power of sample 30887 and of a GaN layer (sample CBL 1043). The straight red and green lines have a slope of one, representing ranges in which radiative and nonradiative recombination channels coexist.

channels coexist. At high excitation densities, the radiative recombination takes over just as in the layer. The superlinear regime at low excitation densities indicates either that in the NWs a nonradiative recombination channel of different nature than in the layer is present or, if the same nonradiative mechanism is present as in the layer, than its density is considerably lower in the NWs. [144]

Nonradiative surface recombination

The different behavior of GaN NWs and layers at elevated temperatures and with increasing excitation density possibly indicates the existence of a different nonradiative recombination channel in the NWs. While in the layers the recombination is most likely dominated by nonradiative recombination due to dislocations, in NWs the dislocation density is very low. However, the surface-to-volume ratio of NWs is considerably larger than that of layers. Hence, nonradiative recombination via the surface may play a prominent role in the NW recombination processes. In fact, the significance of nonradiative surface recombination in GaN NWs has been shown by Schlager *et al.*,[104] who determined the surface recombination velocity S for GaN at room temperature to 9×10^3 cm/s from the diameter-dependent lifetimes in GaN NWs. In GaN layers the contribution of the nonradiative surface recombination is actually too small to determine S. With Eq. 4.1 and assuming a bulk lifetime of 1.2 ns,[138] this surface recombination velocity is equivalent to an effective lifetime of about 100 ps for NWs with a diameter of 40 nm.

The nonradiative surface recombination velocity in GaAs is several orders of magnitude higher ($S_{GaAs} = 10^6$ cm/s)[145] than that in GaN. Consequently, its effect on the optical properties of NWs can be illustrated by a comparison of the PL intensity of bare GaAs NWs and GaAs/(Al,Ga)As core-shell NWs. Figure 5.6 shows the low-temperature PL spectra of bare GaAs NWs (sample M6835) and of GaAs/(Al,Ga)As core-shell NWs (sample M6868). The PL intensity of sample M6835 is considerably lower than that of sample M6868. The (Al,Ga)As shell, that has a nominal Al content of 10%, has a larger bandgap than the GaAs core and acts as a barrier to free carriers. Hence, nonradiative surface recombination is effectively prevented and the PL intensity of this sample is considerably increased.
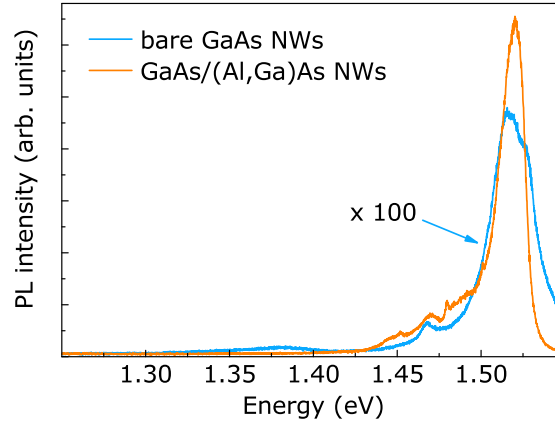
Figure 5.6.: Comparison of the PL of GaAs/(Al,Ga)As core-shell NWs (sample M6868) and bare GaAs NWs (sample 6835). The spectra are recorded at 10 K.

The cases of both, GaN and GaAs NWs indicate, that the surface introduces a nonradiative recombination channel. Due to their large surface-to-volume ratio, this recombination process may severely affect the optical properties of NWs.

5.4. Light coupling and strain in GaN nanowires

Coupling of light into and extraction of light out of GaN nanowires

Figure 5.7(a) compares Raman spectra of a GaN NW ensemble (sample M9257) and of a thick GaN buffer grown on Si (sample NAE_02042) with (In,Ga)N QWs on top. On the right-hand side of the graph, the signal is enlarged by a factor of 20 in order to visualize the LO phonon part of the spectra. The spectra are taken in polarized $[z(y,y)\bar{z}]$ and depolarized $[z(x,y)\bar{z}]$ configuration using the 482.5-nm line of the Kr^+ laser. All spectra are dominated by the optical phonon peak from the Si substrate at 520.2 cm^{-1}.[146] As expected from the selection rules listed in Tab. 3.3, the layer signal contains the E_2^H phonon at 569.7 cm^{-1} and the $A_1(LO)$ phonon at 733 cm^{-1}.[96] The latter one appears only in the polarized, but not in the depolarized configuration. The NWs exhibit a slightly lower Raman shift of the E_2^H phonon of 567.3 cm^{-1}. In contrast to the layer, the NWs do not show the $A_1(LO)$ phonon in either of the two configurations, but rather the $E_1(LO)$ phonon at 742 cm^{-1}.[96] In addition, a broad band from 660 to 760 cm^{-1} can be found due to surface optical (SO) phonon modes.[147] The exact Raman shift of these modes depends on the NW diameter. The rather broad SO band thus indicates a large variance in diameters with a mean value of 100 nm.[148] For the Raman spectra in Fig. 5.7(b), the 413-nm line of the Kr^+ laser is used. The $A_1(TO)$ and the $E_1(TO)$ phonons at 531.8 cm^{-1} and at 558.6 cm^{-1}, respectively, can be identified.[96] In the inset of Fig. 5.7(b), the Si LO phonon and the E_2^H phonon are shown to full scale.

Considering the allowed Raman configurations as listed in Tab. 3.3, these results reveal how light is coupled into and extracted out of the NW volume. If the light would penetrate into the NWs through their c-plane top facets, the $A_1(LO)$ should appear in the $z(y,y)\bar{z}$ and disappear in the $z(x,y)\bar{z}$ configuration. However, in neither of the two configurations the $A_1(LO)$ phonon is observed. The $A_1(TO)$, $E_1(TO)$, and $E_1(LO)$ phonons are only allowed if the light enters *and* leaves the NW volume through the sidewalls [cf. the $x(*,*)\bar{x}$ and $x(*,*)y$ configurations in Tab. 3.3]. A similar result is obtained from
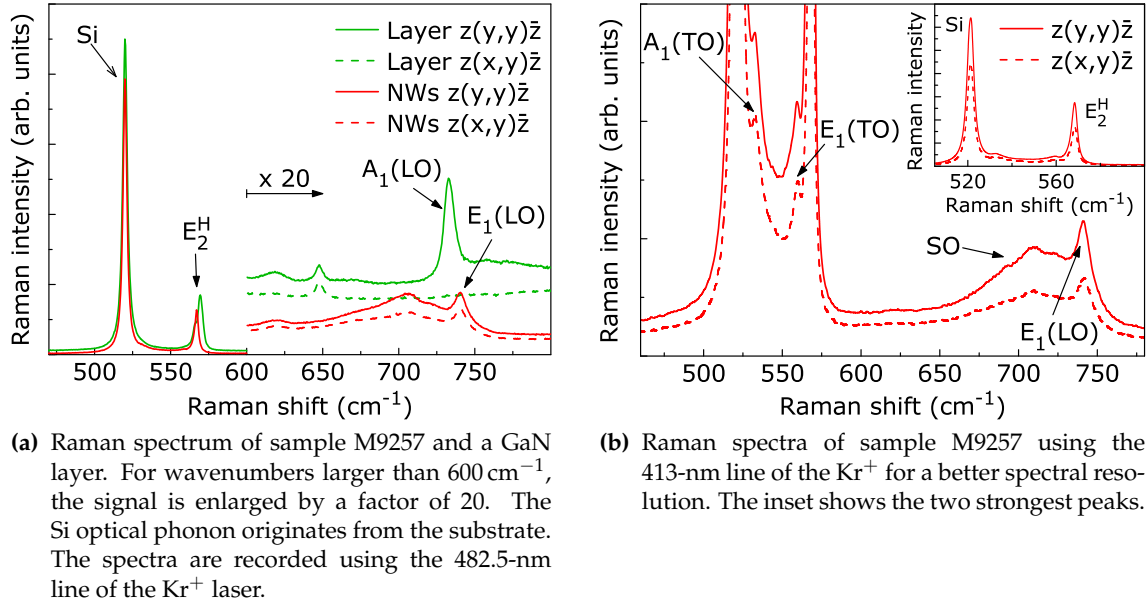
(a) Raman spectrum of sample M9257 and a GaN layer. For wavenumbers larger than $600\,\mathrm{cm}^{-1}$, the signal is enlarged by a factor of 20. The Si optical phonon originates from the substrate. The spectra are recorded using the 482.5-nm line of the Kr^+ laser.

(b) Raman spectra of sample M9257 using the 413-nm line of the Kr^+ for a better spectral resolution. The inset shows the two strongest peaks.

Figure 5.7.: Raman spectroscopy of a GaN NW ensemble (sample M9257) and a thick GaN layer grown on Si (sample NAE_02042) with (In,Ga)N QWs on top. The red and green lines refer to the NWs and the layer, respectively. Solid and dashed lines depict spectra taken in polarized [$z(y,y)\bar{z}$] and depolarized [$z(x,y)\bar{z}$] configuration, respectively.

theoretical considerations of the coupling of light into a NW ensemble. In order to investigate the PL excitation density profile in NWs, we solve Maxwell's equations for a periodic array of GaN NWs standing on a Si wafer.[b] In accordance with Huygen's principle, we find that the incident wave is diffracted at the NW tips and horizontally propagating diffracted waves excite the NWs through their sidewalls. As a result, the NWs are excited over their entire length. Due to reflection at the substrate, the light forms standing waves inside the NWs, i.e., along the NW axis a sinusoidal profile of the light intensity is obtained.[149]

Strain state of GaN nanowires

The Raman shift of the E_2^H phonon is sensitive to homogeneously distributed strain. In the NW spectra shown in Fig. 5.7(a), the E_2^H phonon is observed at $567.3\,\mathrm{cm}^{-1}$. The spectrum is calibrated using the LO phonon of Si at $520.2\,\mathrm{cm}^{-1}$.[146] The position of the E_2^H phonon obtained from Raman measurements of single crystalline GaN samples is determined to $567.6\,\mathrm{cm}^{-1}$,[96] and experiments of GaN NWs yielded a value of $567.1\,\mathrm{cm}^{-1}$.[132] Thus, within the error margins of $1\,\mathrm{cm}^{-1}$, our E_2 phonon value agrees well with literature data of unstrained GaN. For the layer, however, the E_2^H phonon is slightly blueshifted, i.e., the layer experiences a net compressive strain.

Figure 5.8(a) shows an $\omega - 2\theta$-scan of sample M9257. It comprises the Si(111) diffraction peak from the substrate and the GaN(0002) peak. The former one is taken to calibrate the diffraction profile using a value of 5.4299 Å for the lattice constant a_{Si} of Si.[150] The GaN(0002) reflection is then found at 17.2826°. Using Eq. 3.2, the lattice constant a_{GaN} of

---

[b]These calculations have been performed by A. Rathsfeld.[149]

(a) $\omega - 2\theta$-scan of sample M9257. The Si(111) diffraction peak originates from the substrate.

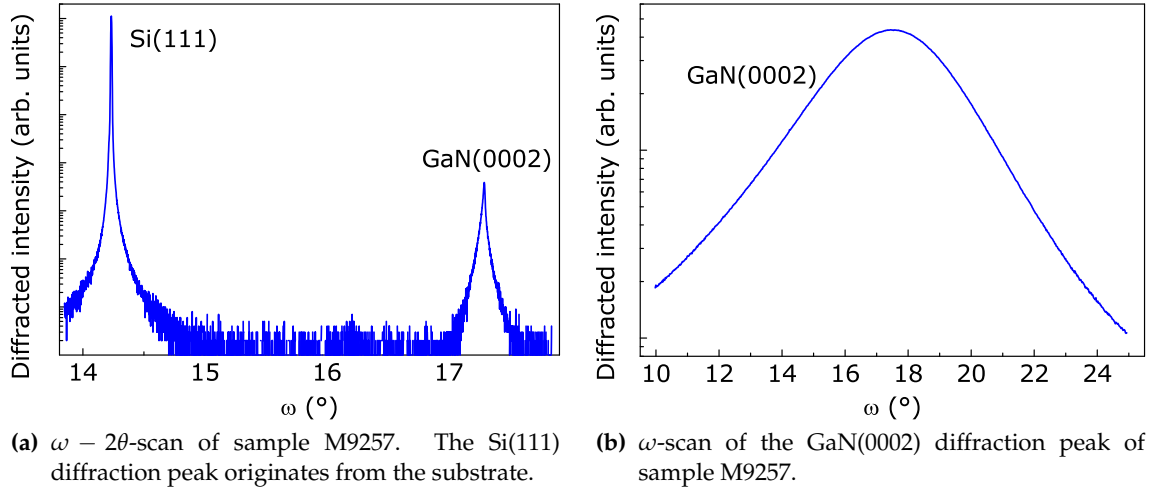**(b)** ω-scan of the GaN(0002) diffraction peak of sample M9257.

Figure 5.8.: Investigation of the strain state of a GaN NW ensemble (sample M9257) using XRD.

the GaN NWs can be determined to 5.1856 Å. This value matches within the error margins data for unstrained bulk or bulk-like GaN ($a_{\mathrm{GaN,ref}} = 5.1855 \pm 0.0006$ Å) reported in the literature.[151] The linewidth of a diffraction peak is determined by inhomogeneous strain and by the thickness of the investigated layer, or, as in the case of NWs, by their length. The thicker the layer or the longer the NWs the narrower is the diffraction peak. Sample M9257 exhibits a certain length distribution. The diffraction peak is thus a superposition of peaks with different linewidths, which consequently results in the rather unusual, almost triangular line shape of the GaN(0002) peak. In Fig. 5.8(b), an ω-scan of the GaN(0002) diffraction peak is shown. From its linewidth, the tilt of the NWs can be estimated to about $4°$. For a thorough investigation of the strain state, the position of higher order peaks [(0004) and (0006)] have to be measured.[151] Nonetheless, the present data confirm that the NWs are essentially free of strain.

Considering the PL, Raman, and XRD data, all three measurement methods show no evidence for the presence of homogeneous strain. However, the broad peak in the PL spectra as well as in the XRD profile may indicate the presence of inhomogeneous strain, with the net strain being zero.

5.5. Conclusions

The PL spectra of state-of-the-art GaN NWs indicate that the NWs are of high crystalline quality. The PL spectra are dominated by the (D^0,X) transition and almost no traces of defect luminescence are visible. However, SF luminescence as well as a rather prominent transition of unknown origin, which does not appear in the PL spectra of GaN layers, are present in the PL spectra of GaN NWs. The nature of the observed peaks has been confirmed by temperature- and excitation-dependent PL experiments. The comparison of the optical properties of GaN NWs with those of GaN layers suggests the presence of different nonradiative recombination mechanisms. Most likely, the large surface-to-volume ratio introduces a significant nonradiative recombination channel.

The investigation of the allowed Raman configurations of GaN NWs reveals that light is coupled into the NW volume through their sidewalls. In the same manner, light is extracted through the NW sidewalls. Furthermore, PL, XRD, and Raman experiments indicate that the NWs are indeed free of strain within the experimental error margins.

6. Broadening mechanisms of the (D^0,X) transition of GaN nanowire ensembles

The linewidth of (D^0,X)-related transitions of GaN NW ensemble measurements typically amounts to a few meV.[104,152] Even in state-of-the-art samples, FWHM of less than 1 meV have not been achieved.[111,132] However, based on the uncertainty principle, the linewidth of an excitonic transition in GaN with a radiative lifetime of about 1 ns can be estimated to be on the order of 1 µeV. Experimentally, a FWHM of less than 100 µeV has been observed for the (D^0,X) transition of GaN using high-resolution PL setups,[153,154] and for Si even a FWHM of about 4 µeV was measured.[155] The setup used for the present work has a spectral resolution of 300 µeV. The observed minimum FWHM of 1.2 meV for the GaN layer and 1.6 meV for sample M9257 [cf. Fig. 5.1(a)] clearly exceed this spectral resolution. As the layers under investigation are grown on a foreign substrate (Al_2O_3), they experience compressive strain, which results in a blue-shift of the spectra. The relatively large spectral linewidth may be explained by the presence of inhomogeneously distributed strain caused by dislocations. The principle of St. Venant[79] (see Sec. 2.4) predicts that NWs are, besides a small region close to the NW/substrate interface, free of strain. The experimental findings of PL and Raman spectroscopy as well as of XRD (cf. Sec. 5.4) support this prediction. CL measurements[a] on single GaN NWs as well as on GaN NW ensembles show that the strained bottom part close to the NW/substrate interface exhibits almost no luminescence. The observed PL must therefore mainly originate from the unstrained part of the NWs. In the following, potential mechanisms leading to a broadening of the (D^0,X) line in GaN NW ensembles are discussed. The origin of this relatively large linewidth is investigated by examining the PL spectra of single dispersed and single free-standing GaN NWs. The results shown here have been reported in Refs. 156 and 157.

6.1. Linewidth broadening mechanisms in nanowire ensemble spectra

Heating at high-excitation levels

When excited carriers thermalize to the band edges, they emit LO phonons (cf. Sec. 2.2), which can be considered as quantized lattice vibrations. In other words, thermal energy is generated. This thermal energy is readily dissipated at low excitation densities, but at high excitation densities, the temperature of the crystal increases. In NWs, the diffusion of excited carriers is laterally restricted by the NW sidewalls and the carrier density can be easily increased to a level not attainable in layers. Thus, already at relatively low excitation densities, the temperature of NWs may increase and the linewidth of the (D^0,X) transition may broaden (cf. Sec. 5.2). Indeed, such a broadening is observed at high excitation powers [see Fig. 5.4(b)]. However, the FWHM remains constant over a several

---

[a]CL measurements have been performed by U. Jahn.

(a) Normalized PL spectra of four GaN NW samples. With increasing substrate temperature, the V/III ratio was adjusted. The spectra are shifted vertically for clarity.

(b) (D^0,X) linewidth of the same GaN NW samples plotted against substrate temperature.
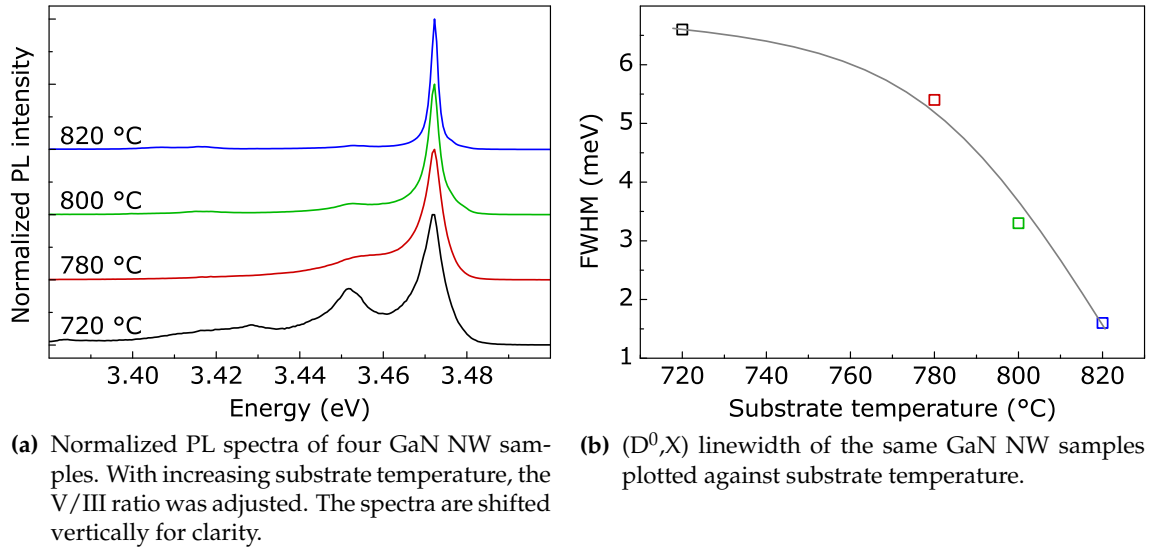
Figure 6.1.: Dependence of the PL spectra of NWs grown at temperatures on the growth temperature. Samples M9246, M9247, M9250, and M9257 were grown at 720, 780, 800, and 820 °C, respectively. The PL measurements are performed at 10 K and with an excitation density of $10^{-4}I_0$.

orders of magnitude of excitation powers before this broadening sets in. The majority of experiments shown here have been conducted in this excitation density range. Hence, the relatively large (D^0,X) linewidth in the NW spectra is not caused by thermal broadening due to the high excitation of the NWs.

Coalescence

The high NW density of $10^{10}\,\mathrm{cm}^{-2}$ inevitably leads to the coalescence of neighboring NWs. When two NWs coalesce, boundary dislocations are formed at the coalescence point to overcome the misalignment between these NWs. In addition, the presence of stacking faults can be observed several hundred nanometers above the coalescence point, giving rise to the luminescence band at 3.42 eV.[46] Along with the boundary dislocations, strain is generated. Although it is accommodated by the nearby free surface, an overall inhomogeneity of the strain state can be expected.

Figure 6.1(a) depicts the PL spectra of four NW samples which have been fabricated with different substrate temperatures (T_{gr} ranges from 720 to 820 °C). As the Ga desorption rate increases with T_{gr}, the Ga flux has to be increased as well in order to ensure N-rich conditions at the substrate surface. As a result, the NW density is on the order of $(2.5 - 4.0) \times 10^9\,\mathrm{cm}^{-2}$ for all samples from this series. The samples show a comparable morphology except for the NWs grown at 720 °C [black line in Fig. 6.1(a)]. At such low temperatures, lateral growth and thus coalescence of adjacent NWs is strongly promoted. Traces of strong coalescence can be found in the PL spectrum of this sample, which shows the most prominent SF luminescence at 3.42 eV of the four samples. This sample also exhibits the strongest (U,X) line.

With increasing substrate temperature, two effects indicating an increasing crystal quality can be observed. On the one hand, defect-related luminescence below the (D^0,X) line becomes less important. On the other hand, the linewidth of the (D^0,X) transition
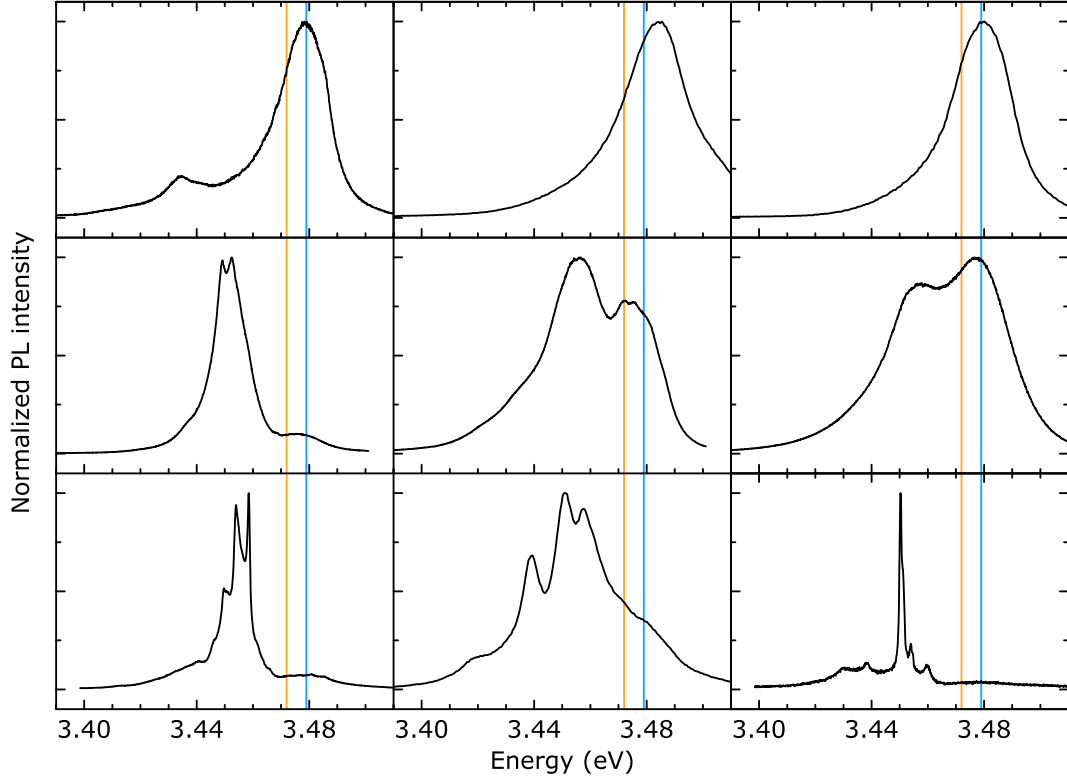
Figure 6.2.: Exemplary, normalized near-band-edge PL spectra of single NWs or NW clusters of sample 30887 dispersed on a Si(111) substrate. In the top row, NW spectra dominated by a broad peak around 3.48 eV are shown. The second row shows NWs exhibiting strong luminescence around the 3.45 eV peak. In the bottom row some NWs with sharp transitions belonging to the 3.45 eV band are depicted. The orange and blue lines mark the positions of the (D^0,X) and FX transitions in unstrained GaN. All measurements are performed at 10 K and at excitation densities ranging from $10^{-2}I_0$ to I_0.

decreases considerably from more than 6 to 1.6 meV as shown in Fig. 6.1(b). Considering the coalescence, no significant reduction[b] can be observed with increasing T_{gr}, since the Ga flux has been increased simultaneously. Hence, the decrease of the linewidth at lower substrate temperatures is not directly related to coalescence-induced strain inhomogeneities. However, it is conceivable that an increase of T_{gr} might lead to a reduced tilting of the NWs. As a consequence, the misalignment, which has to be accommodated when adjacent NWs coalesce, may be less, and thus, the induced strain would be reduced. However, increasing T_{gr} above 820 °C does not further reduce the linewidth of the (D^0,X) transition. Thus, linewidths much in excess of 1 meV are likely to be caused by coalescence-induced strain.

Strain in dispersed nanowires

With a NW density of $10^{10} \, cm^{-2}$, around 10^3 NWs are probed simultaneously even in µPL measurements of as-grown NW ensembles. These 10^3 NWs most certainly contain coalesced as well as non-coalesced NWs, which all contribute to the recorded ensemble PL spectra. As coalescence induces inhomogeneous strain, which possibly broadens the

---

[b]The quantification of the coalescence degree is rather difficult. Here, only subjective impressions can be given.

(a) PL spectra of a dispersed NW at different excitation densities.

(b) Typical spectrum of a dispersed single NW compared to a NW ensemble (sample 30887).
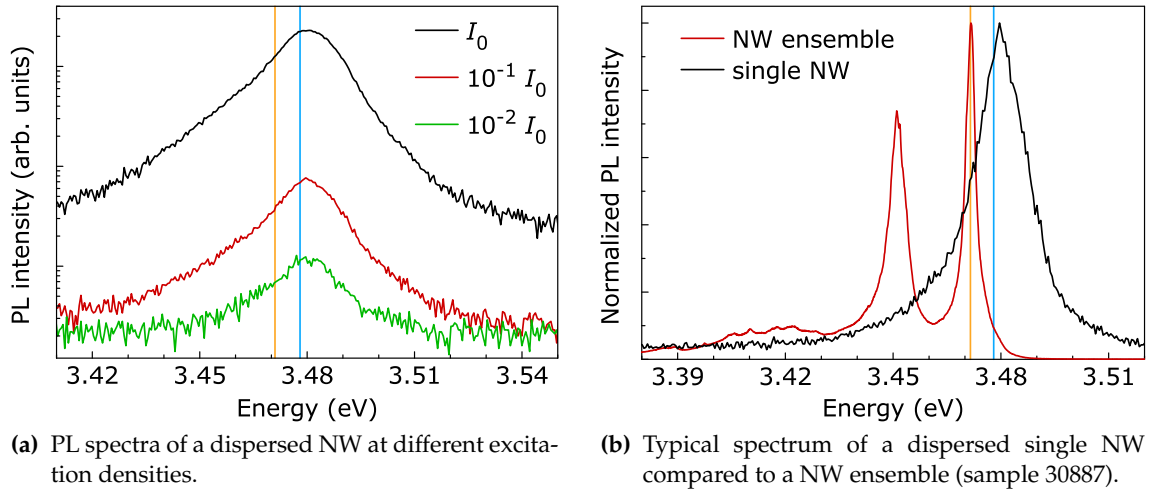
Figure 6.3.: Typical low-temperature PL spectra of a single NW of sample 30887 dispersed on Si(111). The orange and blue lines mark the positions of the (D^0,X) and FX transitions in unstrained GaN.

(D^0,X) transition, the luminescence of single, non-coalesced NWs can be expected to exhibit much sharper lines. In order to investigate this assumption, single NWs of sample 30887 have been dispersed on a Si(111) substrate. More than 30 dispersed single NWs or NW cluster have been investigated, each of which exhibiting its own, individual PL spectrum. Several examples are shown in Fig. 6.2. These spectra are often dominated by a single broad transition (FWHM larger than 20 meV) with a peak energy around 3.48 eV (cf. top row in Fig. 6.2). Probably, these NWs suffer from inhomogeneous, overall compressive strain introduced by adhesive interaction with the substrate the NWs are dispersed on. The excitation-density-dependent measurements of such a NW are shown in Fig. 6.3(a), indicating that the line broadening is not due to the relatively high excitation power necessary to probe single NWs. An additional prominent line is the (U,X) band (cf. middle and bottom rows of Fig. 6.2). For a number of NWs, a reduction of the excitation density revealed a fine structure of this band with lines having a FWHM down to 1.7 meV. The presence of this fine structure indicates that the 3.45 eV band observed in Fig. 5.1(a) may actually be a superposition of many sharp lines. The SF-related luminescence around 3.42 eV as seen in ensemble measurements [cf. Fig. 5.1(a)] can be found only in a few single NW spectra.

Figure 6.3(b) depicts a typical spectrum of a dispersed single NW in comparison to the ensemble PL. It points out what essentially all dispersed NWs have in common. They are distinctively different from the ensemble spectrum, which is, as pointed out above, the superposition of about 10^3 individual NW spectra. Consequently, ensemble measurements are not necessarily eligible to discuss properties of single NWs.

Besides the large number of NWs suffering from adhesion-induced strain,[104] a few NWs do not exhibit any traces of strain. In contrast, the corresponding spectra show well-resolved, narrow transitions. Figure 6.4 depicts the near-band-edge luminescence of two such NWs (in the following referred to as NW 1 and NW 2). The spectrum of NW 1 [depicted in Fig. 6.4(a)] shows a pronounced contribution from the (U,X) transition around 3.45 eV and several, partially merged lines related to (D^0,X) and FX transitions. By varying the excitation density, the typical GaN-related excitonic transitions can be

(a) Excitation-density-dependent PL spectra of NW 1.

(b) High-resolution PL spectra of the same NW at two different excitation densities.

(c) High-resolution PL spectrum of NW 2 recorded at an excitation density of $10^{-2}I_0$.

(d) High-energy range of the same spectrum as in (c) after background subtraction. The resulting spectrum has been fitted with a set of Gaussians (gray line).
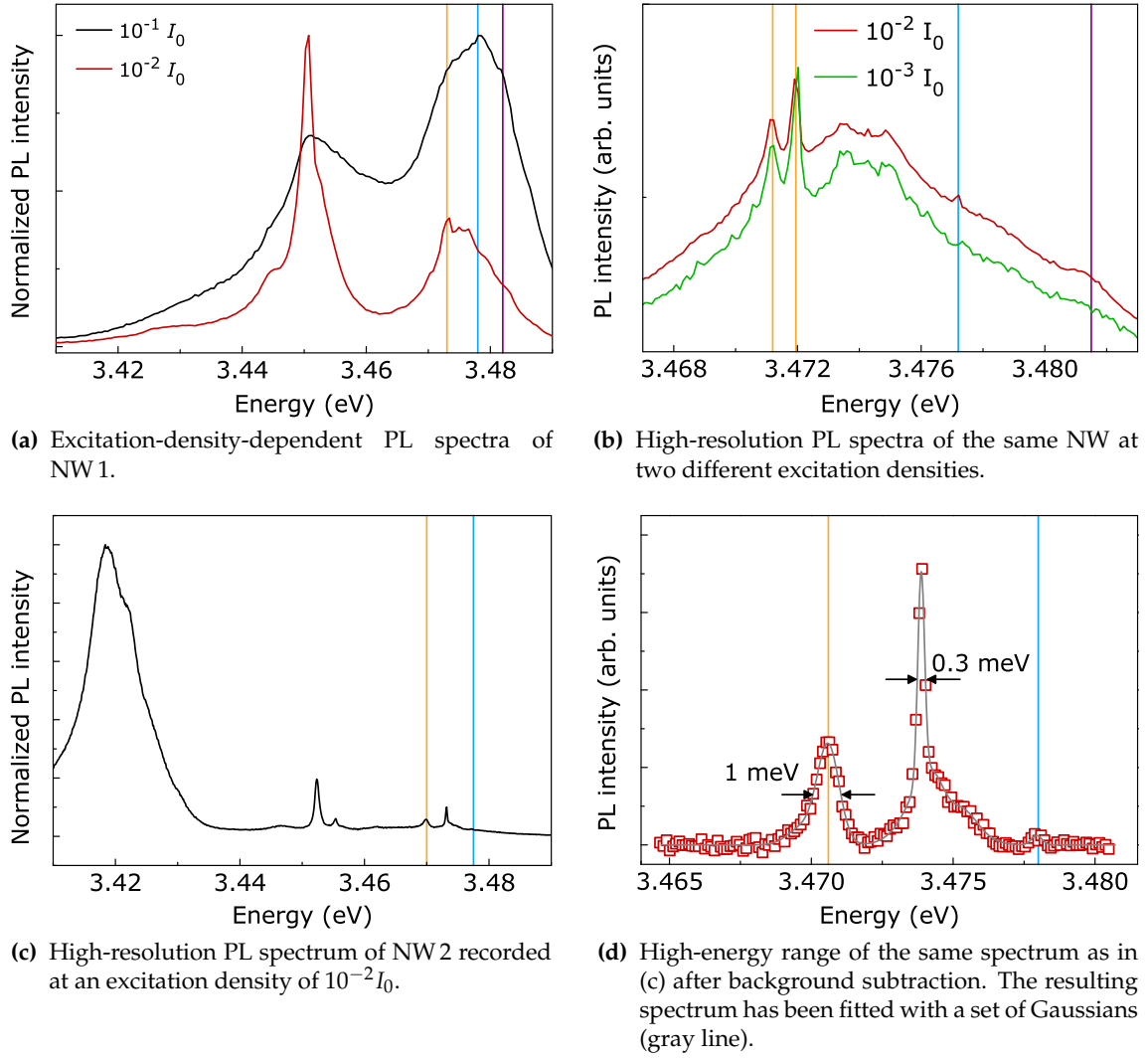
Figure 6.4.: PL spectra of two strain-free, dispersed NWs from sample 30887. The spectra are recorded at 10 K. The orange, blue, and violet lines mark the positions of the (D^0,X_A), FX_A, and FX_B transitions in unstrained GaN, respectively.

identified. The (D^0,X) line is found at 3.472 eV. With increasing excitation density, it saturates, and the FX_A at 3.478 eV becomes dominant. Furthermore, the FX_B at 3.482 eV can be detected as a shoulder on the high-energy side of the major transition. All energy positions agree well with unstrained GaN.

Figure 6.4(b) shows a high-resolution spectrum of the very same NW. The (D^0,X_A) transition splits into two lines at 3.4712 and 3.4719 eV, corresponding to excitons bound to O and Si donors, respectively. [138] As these spectra are recorded with lower excitation density, the FX_A and FX_B transitions are weak and cannot be resolved. However, two small shoulders at 3.477 and 3.4815 eV indicate their presence. Summarizing these findings, this specific NW does not suffer from adhesion-induced strain. More important, however, is the fact that O- and Si-related (D^0,X_A) transitions are spectrally resolved, in contrast to the ensemble spectra. As these transitions are separated by about 1 meV, this finding suggests that indeed sharp transitions may be observed when single NWs are investigated.

The PL spectrum of NW 2 is plotted in Fig. 6.4(c). This NW is one of the few examples, where the SF-related luminescence around 3.42 eV is dominant. A contribution from the (U,X) transition is also visible. The spectrum shows a sharp (D^0,X$_A$) line at 3.471 eV with a FWHM of 1 meV.

Both NWs are interesting as they exhibit several prominent lines in the energy range in between the (D^0,X$_A$) and FX transition energies. In this range, no strong transitions exist for bulk or unstrained GaN. In high-quality epitaxial layers, lines around 3.474 eV have been observed, which either originate from excited states of the (D^0,X$_A$) or from the ground state of the (D^0,X$_B$).[154] However, their intensity, is several orders of magnitude smaller than the ground state (D^0,X$_A$) at 3.471 eV. Furthermore, this line cannot originate from an unknown impurity. With Eqs. 2.8 and 2.9, the *minimum* binding energy of an exciton bound to a hydrogenic donor can be determined to 7 meV. Excitons bound to unknown impurities would therefore emit at lower energies.

As the majority of dispersed NWs is inhomogeneously strained, it might be possible that some NWs experience homogeneous strain, which would not broaden the excitonic transitions, but shift the complete spectrum. In the case of NW 1, such a shift can be excluded as the (D^0,X), FX$_A$, and FX$_B$ transitions are found to occur at the same energies as in unstrained GaN. The excitation-density-dependent measurements illustrate the correct assignment of these transitions. For NW 2, a rigid shift of the entire PL spectrum due to strain can be excluded for the following reason: The energy separation between the two peaks at 3.471 and 3.474 eV amounts to 3 meV, while the energy difference between either the (A^0,X) and (D^0,X) or the (D^0,X) and FX transitions is 7 meV. Hence, the sharp transition at 3.474 eV can neither represent an FX transition in GaN under tensile strain, nor an (A^0,X) transition in compressively strained GaN.

In order to accurately determine the peak positions and linewidths of the highest-energy transitions for NW 2, the underlying background is subtracted, and the lines are fitted to a set of Gaussians as shown in Fig. 6.4(d). At 3.4779 eV, the FX$_A$ is unveiled, further confirming the correct assignment of the (D^0,X) transition, which is now more accurately determined to occur at 3.4706 eV. Just as in NW 1, the linewidth of the (D^0,X) transition in NW 2 is below 1 meV, i.e., considerably less than in the related NW ensemble PL. The FWHM of the line at 3.4739 eV amounts to 280 μeV, which corresponds to the spectral resolution of the setup.

Besides strain, other mechanisms causing a peak shift are conceivable. Due to the pinning of the Fermi level at the NW sidewalls, a depletion region at the NW sidewalls[75] forms. The band profile depends on the diameter and the doping density of the NW. Irrespective of the actual band profile, electric fields and inhomogeneities in the carrier concentration are a consequence of band bending. Both effects are known to shift optical transitions. As their extent varies within a NW, donor-related luminescence originating from different parts of the NW might have different energies. However, the energy of *bound-exciton* transitions is insensitive to electric fields. Although it is true that the exciton binding energy is reduced in electric fields, the resulting blue-shift is almost exactly compensated by the quadratic Stark effect that bound excitons experience. More importantly, the excitonic radiative recombination efficiency is dramatically reduced, which is reflected in a pronounced quenching of the PL intensity.[58,158] In the same manner, screening can be excluded. If the exciton binding energy is decreased due to screening by free carriers, the shrinkage of the bandgap almost completely cancels the resulting blue-shift.[58]
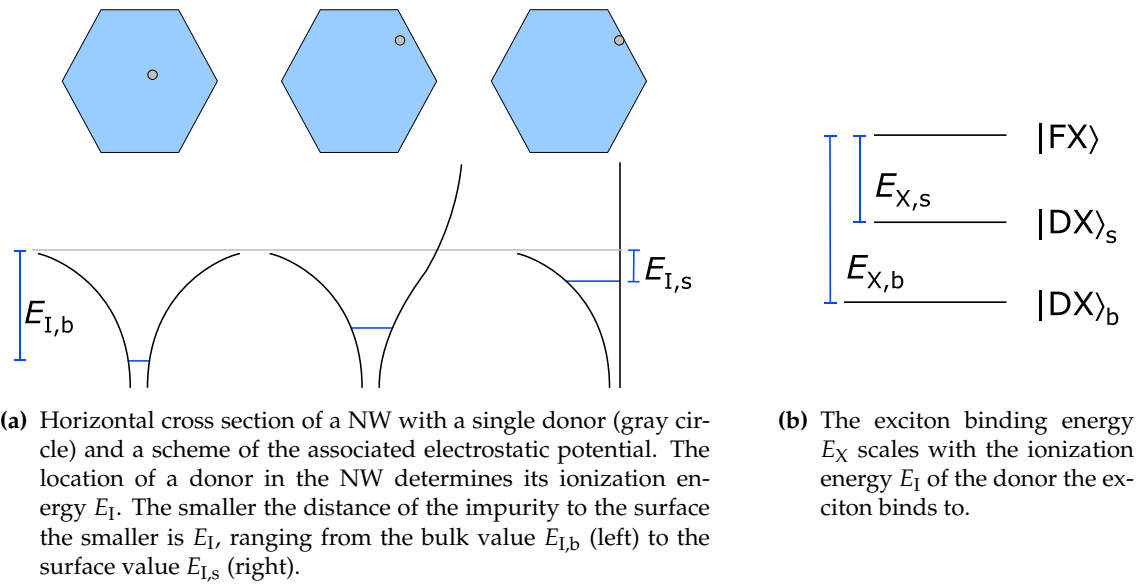
(a) Horizontal cross section of a NW with a single donor (gray circle) and a scheme of the associated electrostatic potential. The location of a donor in the NW determines its ionization energy E_I. The smaller the distance of the impurity to the surface the smaller is E_I, ranging from the bulk value $E_{I,b}$ (left) to the surface value $E_{I,s}$ (right).

(b) The exciton binding energy E_X scales with the ionization energy E_I of the donor the exciton binds to.

Figure 6.5.: Schematic description of the correlation between surface and bulk donors and the corresponding ionization and exciton binding energies.

Surface donors

According to Haynes' rule (cf. Eq. 2.9), the (D^0,X) transition energy is determined by the chemical nature of the associated donor, as the exciton binding energy $E_{X,b}$ scales linearly with the donor ionization energy $E_{I,b}$.[c] A bulk donor has a symmetric electrostatic potential, which defines $E_{I,b}$ (and thus also $E_{X,b}$) as depicted in Fig. 6.5(a). Bringing such a donor close to the crystal surface will affect its electrostatic potential. In the extreme case of surface donors, this potential is highly asymmetric with a high potential barrier outside the crystal. Assuming this barrier to be infinite, the ionization energy can be determined analytically to

$$E_{I,s} = \frac{1}{4} E_{I,b} , \tag{6.1}$$

as shown by Levine.[159] The exciton binding energy $E_{FX,s}$ is also expected to decrease when the exciton is near the surface.[160] This result can be extended to excitonic complexes such as excitons bound to surface donors $(D^0,X)_s$. Recent tight binding calculations[161] confirm the general tendency that $E_{I,s} < E_{I,b}$, even for the more realistic case of a finite barrier and considering the dielectric mismatch between the NW and its surrounding.

If the exciton binding energy E_X decreases, the corresponding spectral line will experience a blue-shift. In the following, the maximum blue-shift (i.e., assuming an infinite barrier as in Eq. 6.1) of an oxygen donor at the surface of a GaN crystal is estimated:

(i) The bulk ionization energy of $E_{I,b} = 32\,\text{meV}$ of an oxygen donor yields, considering Haynes' rule, an exciton binding energy $E_{X,b}$ of $0.21\,E_{I,b} \approx 7\,\text{meV}$.[162]

(ii) The ionization energy of an oxygen donor at the surface is reduced according to Eq. 6.1 to a minimum value of $E_{I,s} \approx 8\,\text{meV}$. The respective exciton binding energy then is reduced to $E_{X,s} \approx 2\,\text{meV}$.

[c]Here, the index b indicates that the general case of a hydrogenic bulk donor is considered, i.e., the donor is sufficiently far from the surface. The index s denotes a surface donor, i.e., a donor right at the surface.

Thus, the maximum possible blue-shift of the (D^0,X)$_s$ line amounts to 5 meV. This shift will be smaller when considering the fact that the energy barrier is finite as well as the dielectric mismatch. Excitons bound to surface donors therefore emit indeed at an energy in between the (D^0,X) and FX transitions. The exact transition energy depends on the actual position of the donor in the NW. Satpathy[160] has calculated the exact position-dependent dispersion of the exciton binding energy E_{FX} for excitons with a distance a to the surface, which is less than $3 a_B$ (where a_B represents the Bohr radius of the exciton).[d] Translating these results to the binding energy E_X of donor-bound excitons in GaN NWs, a peak shift of more than 1 meV is observed if $a \leq 1.4 a_B$, and of more than 2 meV if $a \leq a_B$.

Considering GaN layers, the fraction η of donors residing sufficiently close to the surface to experience its influence is vanishingly small. In NWs, however, the fraction η of donors located close to the surface (i.e., within a cylindrical shell with $R - 1.4 a_B < a < R$, where R is the radius of a cylindrical NW) increases drastically:

$$\eta = 1 - (1 - 1.4 a_B/R)^2. \tag{6.2}$$

In the present case with $R = 20$ nm and $a_B = 4.8$ nm,[58] 56% of the randomly distributed donors are effectively close to or at the surface.[e] The actual number of surface donors depends on the donor concentration. In typical GaN layers, the lower limit of the donor concentration is about 10^{17} cm^{-3}. The NWs have an average volume of less than 10^{-15} cm^3. If we assumed a similar donor concentration in the NWs as in GaN layers, we would expect about 100 donors in a single column. More than 50 of these donors would be close to or at the NW surface. As the individual donors are assumed to be randomly distributed, their distances a from the NW sidewalls would vary from $R - 1.4 a_B$ to R. Probing such a NW optically, all donors would emit simultaneously. With the position-dependent dispersion of the (D^0,X)$_s$ transition energy, the result would be a broad (D^0,X) line, where the contribution from (D^0,X)$_s$ recombination is masked in the high energy tail of the (D^0,X) line (where 50% of the donors emit at the same energy). It would essentially look similar to the (D^0,X) line of a NW ensemble. However, probing single NWs, we observe distinct sharp transitions [cf. Fig. 6.4(c)]. Therefore, we expect to find considerably lower donor concentration of about 10^{16} cm^{-3}. In this case, *on average* around five donors per NW are present and distinct lines may be observed. In fact, much lower donor concentrations on the order of 10^{14} to 10^{16} cm^{-3} have been found in unintentionally doped GaN NWs.[163] The previously mentioned segregation and annihilation of point defects to and at the surface, respectively, enhances the electrical grade of NWs drastically. In Sec. 6.2, the donor concentration of thin NWs of the present sample is estimated to be less than 10^{16} cm^{-3} based on a statistical analysis of about 60 NWs.

Independent of the actual donor concentration, the position-dependent dispersion of the (D^0,X)$_s$ transition energy represents an intrinsic mechanism contributing to the linewidth of the (D^0,X) line in NW ensemble spectra. The mere number of excited NWs yields sufficient statistics to find significant contributions from (D^0,X)$_s$ transitions, each with its individual recombination energy, which will inevitably result in a broad (D^0,X) line in the ensemble PL.

---

[d]Both, free as well as donor-bound excitons can be treated like a hydrogen atom with modified mass and dielectric constant. Therefore, the results obtained by Satpathy[160] for the free exciton binding energy E_{FX} can be transferred to the energy E_X with which excitons are bound to donors.

[e]It should be noted that the accuracy of η is limited. First of all, using SEM, the NW diameter is only accurate within about 5 nm. Second, while the peak position of a surface donor may be determined precisely, the peak shift is still subject to an error of about 1 meV, as the chemical nature of a *surface* donor cannot be identified by PL spectroscopy. For instance, a transition at 3.474 eV may be either related to an O donor or to a Si donor close to the surface. The respective peak shift is then either 3 or 2 meV.[138] Regarding these limitations, Eq. 6.2 may indicate the significance of surface donors for a given sample.
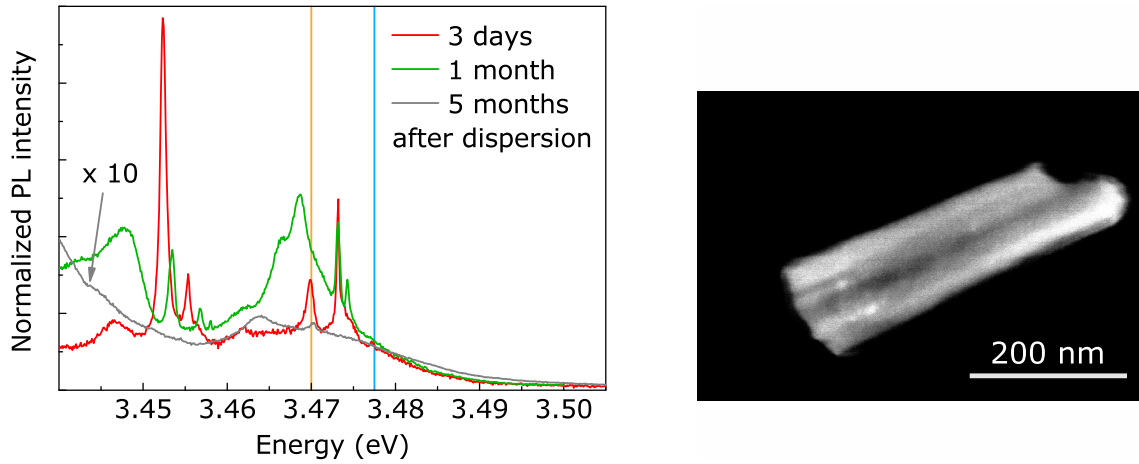
(a) Low-temperature PL spectra of the dispersed NW 2 three days (red), one month (green), and five months (gray) after dispersion. The first two measurements are performed at an excitation density of $10^{-2}I_0$ and the last one at $10^{-1}I_0$. The orange and blue lines mark the positions of the (D^0,X) and FX transitions, respectively, in unstrained GaN.

(b) SEM picture of NW 2 taken between the second (green) and third (gray) PL measurement shown in Fig. 6.6(a).

Figure 6.6.: Long-time evolution of the near-band-edge luminescence of NW 2.

Surface segregation

The segregation of point defects (including impurities) within a semiconductor crystal is mainly observed during growth, where substrate temperatures of typically 780 to 800 °C are applied. The position at the surface of a crystal is energetically favorable for point defects, which represents the driving force for the segregation process.[161] Although at room temperature this process is much less pronounced, it may still be existent on long time scales.

In Fig. 6.6(a), the near-band-edge luminescence of NW 2 recorded three days, one month, and five months after dispersion is depicted. An SEM image of NW 2 [shown in Fig. 6.6(b)] has been taken between the second and third PL measurement, which presumably led to a massive C deposition. The first two PL spectra show several sharp near-band-edge transitions around 3.47 as well as around 3.45 eV. All transitions exhibit different spectral energies, linewidths, and intensities, although each spectrum has been carefully recorded several times.[f] In the third spectrum, the majority of peaks has vanished, and the overall intensity of the luminescence has decreased by about two orders of magnitude. This loss in PL intensity can be ascribed to the SEM-related C contamination. The differences between the first two spectra, however, can only be understood by considering a temporal evolution of the environment of the recombining excitons in the NW. In Figure 6.7, the highest energy transitions are compared for the first and second measurement after background correction and fitted each with a set of Gaussians. Both spectra show weak contributions from the FX, confirming that the strain state of the NW

---

[f]The relative intensity of PL transitions of dispersed NWs critically depend on the position of the NW relative to the laser focus. A thorough positing and focusing of the laser spot is required in order to record reliable spectra. Therefore, each of the three spectra shown in Fig. 6.6(a) has been reproduced multiple times after repositioning the NW.
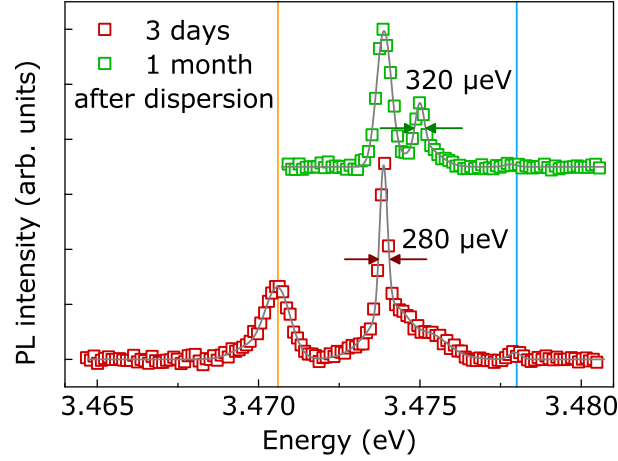
Figure 6.7.: High-resolution PL spectra of NW 2 three days (red) and one month (green) after dispersion. The spectra are fitted each with a set of Gaussians (gray lines). The measurements are performed with an excitation density of $10^{-2}I_0$ at $10\,\mathrm{K}$. The orange and blue lines mark the positions of the (D^0,X) and FX transitions in unstrained GaN.

did not change with time. The donor-related PL, however, shows striking differences. First, the bulk donor at 3.4706 eV appears only in the first spectrum. More importantly, the prominent $(D^0,X)_s$ transition at 3.4739 eV has two high-energy shoulders in the first spectrum. In the second spectrum, the same $(D^0,X)_s$ line can be found. In addition, a sharp $(D^0,X)_s$ transition with a FWHM of 320 µeV emerges at 3.4750 eV.

The degraded PL of the third spectrum in Fig. 6.6(a) has been ascribed to a modification of the surface due to a massive C deposition. Thus, it might be conceivable that the surface is modified between the first and the second measurement as well, possibly due to exposure of the sample to air. However, in Chap. 7 it will be shown that such a modification may affect the intensity of an excitonic transition, but not its energy. Hence, a spectral shift has to be caused by a different mechanism. Figure 6.5(a) describes the dependence of the ionization energy of a donor on its distance to the surface. As a few atomic hops may be sufficient to convert a bulk donor into a surface donor and thus induce a spectral shift, the segregation mechanism of donors to the surface provides a plausible explanation for the temporal evolution of the PL of NW 2.

6.2. Free-standing single nanowires

With only about 10% of the dispersed NWs being free of strain, a systematic investigation of $(D^0,X)_s$-related effects in these NWs is rather difficult. Nonetheless, a statistically significant number of strain-free single NWs is desirable in order to evaluate the significance of surface donors. The high NW density of $10^{10}\,\mathrm{cm}^2$ in as-grown ensembles does not allow for addressing single NWs in a standard µPL setup as the minimum spot diameter of the exciting laser is about 3 µm. However, the NW density thins out considerably toward the edge for samples grown in the MBE at Qimonda as the substrate holder induces a gradient of the substrate temperature. Having an increased substrate temperature at the wafer edge, the desorption of Ga adatoms is increased leading to a reduced nucleation density. As a result, in a region about 1 cm from the wafer edge, the distances between individual NWs are larger than 1 µm, which allows us to optically address single, free-
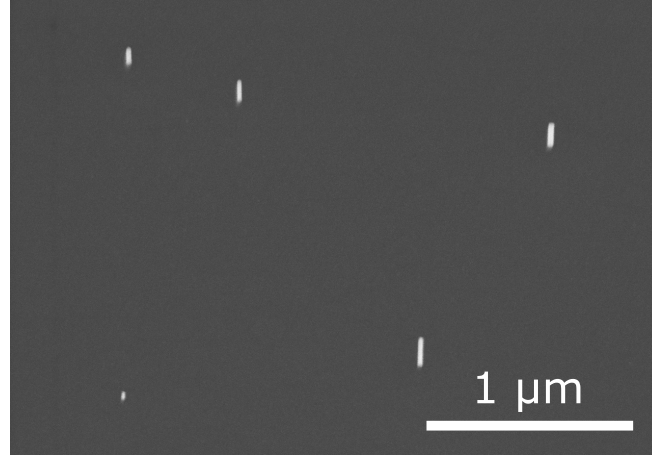
Figure 6.8.: Bird's eye SEM picture of single, free-standing NWs with a diameter of 30 nm and a length of less than 300 nm.
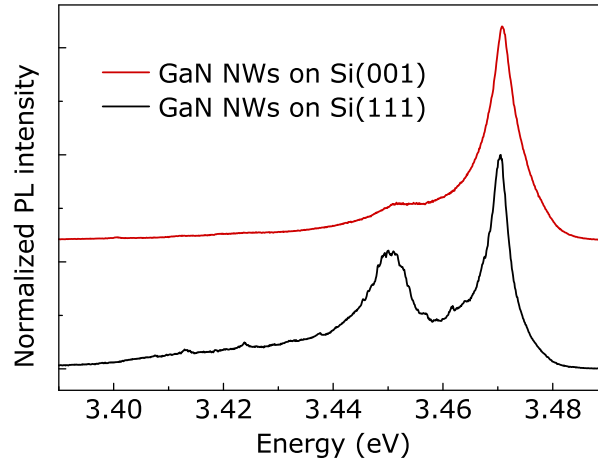

Figure 6.9.: Ensemble PL spectra of samples 30887 and 30927 grown on Si(001) and Si(111), respectively. The spectra are shifted vertically for clarity. Area maps of free-standing NWs of both samples are shown in Fig. 6.10.

standing NWs in our μPL setup. These NWs are free of strain by their very nature (cf. the principle of St. Venant in Sec. 2.4). A bird's eye SEM image of this region is shown in Fig. 6.8. With a diameter of about 30 nm and a length of less than 300 nm, these free-standing NWs are slightly smaller than those in the middle of the wafer. Furthermore, it should be noted that there is no parasitic growth in-between the free-standing NWs.

Free-standing NWs of two samples grown on Si(001) (sample 30927) and on Si(111) (sample 30887) have been investigated. Their respective ensemble PL spectra recorded in the center of the wafer are shown in Fig. 6.9. Both ensemble spectra are similar in that they exhibit the common luminescence bands at 3.471, 3.45, and 3.42 eV corresponding to the dominant (D^0,X) transition, the (U,X) band, and the SF-related luminescence band, respectively.
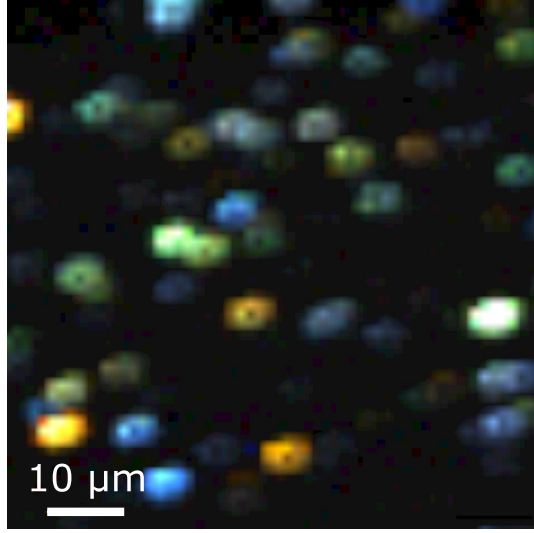
(a) Trichromatic area map of sample 30927 grown on Si(001).
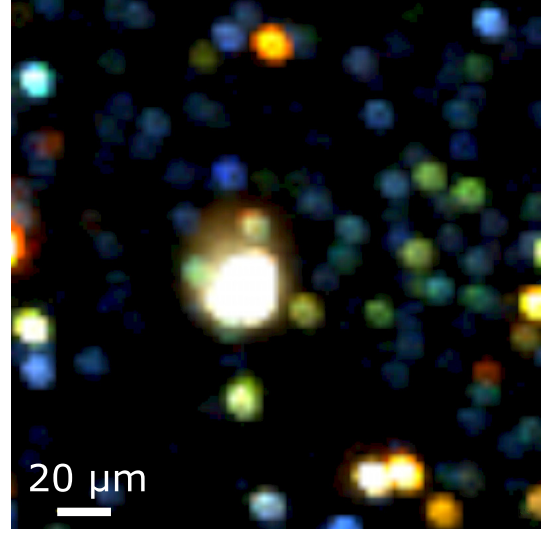
(b) Trichromatic area map of sample 30887 grown on Si(111).

Figure 6.10.: Trichromatic area maps of free-standing GaN NWs recorded at 10 K. The maps are color-coded such that the red/orange, green, and blue spots represent spectra dominated by (D^0,X), $(D^0,X)_s$, and FX transitions, respectively. The large white spot in the center of 6.10(b) is excluded from the analysis as SEM images show that it is caused by a large number of accidentally dispersed NWs.
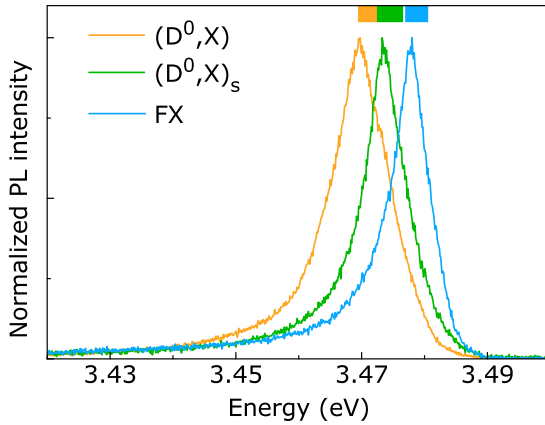
(a) Exemplary PL spectra of free-standing NWs from sample 30927 grown on Si(001).
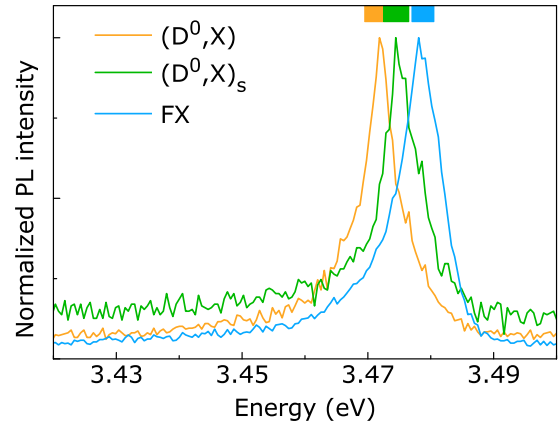
(b) Exemplary PL spectra of free-standing NWs from sample 30887 grown on Si(111).

Figure 6.11.: PL spectra extracted from the trichromatic area maps in Fig. 6.10. The orange, green, and blue spectra exemplify NWs whose PL spectra are dominated by (D^0,X), $(D^0,X)_s$, and FX recombination, respectively. The spectral ranges are illustrated by the correspondingly colored bars at the top of the graphs.

(a) PL spectra of a single, free-standing NW from sample 30927 grown on Si(001) at different excitation densities. The position of the (D^0,X) at 3.471 eV and the FX at 3.478 eV in unstrained GaN are denoted by the vertical, orange and blue lines, respectively.

(b) PL spectra of two NWs from sample 30887 grown on Si(111), which exhibit several excitonic transitions. The spectral ranges of the (D^0,X), $(D^0,X)_s$, and FX transitions are illustrated by the correspondingly colored bars at the top of the graphs.

Figure 6.12.: Confirmation of the presence and correct assignment of distinct recombination channels observed in single, free-standing NWs.

Trichromatic area maps

Trichromatic area maps of free-standing NWs are shown in Fig. 6.10. These maps consist of several thousand near-band-edge spectra (60×60 for sample 30927 and 70×70 for sample 30887) recorded at 10 K with an excitation density of $10^{-2}I_0$. The color code describes the wavelength range of the dominant near-band-edge transition at each position in the area map. Red (including orange), green, and blue spots represent spectra governed by (D^0,X) ($3.4695 - 3.4725$ eV), $(D^0,X)_s$ ($3.4725 - 3.4765$ eV), and FX ($3.4770 - 3.4805$ eV) transitions, respectively. White and yellow spots indicate the presence of several strong transitions. (A^0,X)-related transitions at 3.465 eV are not observed at all, but some NWs from sample 30887 [grown on Si(111)] show additional luminescence around 3.45 eV. In Figure 6.11, exemplary spectra for all three near-band-edge transitions are extracted from the respective area maps. The large linewidth of the depicted spectra is caused by the relatively high excitation density, which is necessary to record the area maps in a feasible timespan.

In order to confirm the strain-free nature of the NWs, exemplary excitation-density-dependent measurements of a single, free-standing NW are shown in Fig. 6.12(a). At low excitation densities, a single (D^0,X) line at 3.471 eV (as in unstrained GaN) with a FWHM of 2 meV is observed. With increasing excitation density, the (D^0,X) transition saturates, and the FX line at 3.477 eV dominates the spectrum. The trichromatic area maps have been recorded using an intermediate excitation density of $10^{-2}I_0$. At this excitation density, the spectrum consists of a relatively broad peak that is actually a superposition of the (D^0,X) and the FX lines. The position of this peak is only slightly shifted with respect to the (D^0,X) line measured at lower excitation density, whereas its linewidth is increased. Nevertheless, the linewidth of these transitions is still sufficiently small to distinguish the different possible transitions.

Figure 6.12(b) depicts two spectra showing several lines. This is the case for about 5% of the free-standing NWs. These free-standing NWs clearly exhibit multiple transitions, originating from different recombination channels. This finding as well as the excitation-dependent measurements shown above confirm both the presence and correct assignment of distinct recombination channels. In other words, the continuous distribution of peak energies in the range from 3.470 to 3.481 eV does not represent one single type of recombination that is shifted by a mechanism such as strain.

Free exciton recombination in free-standing nanowires

As denoted above, most free-standing NWs exhibit only one relatively broad transition at an excitation density of $10^{-2}I_0$. In general, this transition either originates from donor-bound [comprising both (D^0,X) and $(D^0,X)_s$ complexes] or from FX recombination. At the given excitation density of $10^{-2}I_0 = 200\,\text{W/cm}^2$ and a laser wavelength of 325 nm, about 3×10^{20} photons/cm^2 impinge each second on the sample surface. Assuming that the NWs are excited through their sidewall, this translates to about 3×10^{10} photons/s that encounter the NW volume. If *all* of these photons were absorbed, the number of generated excitons would be of the same order. With a $1/e$-decay time of about 130 ps, roughly four excitons would be present in a NW at any given time. Due to the small diameter, only a fraction of the photons will be absorbed. Thus, the average number of excitons can be estimated to be on the order of one or less.

A FX binds to a donor when it experiences the short-range potential of the donor before it actually recombines. In a sufficiently large crystal, a convenient measure is the FX diffusion length, which is at least 200 nm in GaN.[164] Comparing this number to the NW dimensions, in particular to their length of 300 nm, indicates that it is very likely for an FX to bind to any present donor. However, diffusion is a statistical concept, which is only meaningful for a sufficiently large number of excitons and donors. Dealing with single excitons and donors in nanometer-sized crystals, this concept is not applicable. Rather, the sub-wavelength dimensions of the NWs have to be taken into account. Due to the uncertainty principle, the exact location of the generated exciton cannot be determined and the FX has to be treated as a coherent excitation of the *entire* NW volume in the instant of its creation.[60,165] In other words, the center-of-mass wavefunction of the FX extends throughout the complete length of the NW. If an (unoccupied) donor is located anywhere in the NW, it will spatially localize this center-of-mass wavefunction and bind the exciton immediately.[g] Consequently, the PL emitted by this NW will reveal the presence of a donor by (D^0,X) or $(D^0,X)_s$ transitions. Thus, the observation of an FX transition implies that there are more excitons per NW than unoccupied donors. As the average number of excitons per NW is one or less and any free excitons will inevitably bind to any present donor, only donor-free NWs are expected to exhibit FX recombination.[h] In the trichromatic area maps (Fig. 6.10), these donor-free NWs are represented by blue spots. This is the case for roughly 25% of the free-standing NWs.

---

[g]The capture process takes a certain time, which is very short compared to any recombination process involved. Hence, the term "immediately" is appropriate. The capture time can be estimated from the kinetic energy of a generated exciton to be on the order of a few ps.

[h]Note that the integration time for each spectrum of the area maps is 1 s. Consequently, each spectrum represents the average of about 10^9 recombination processes. Even if a FX recombined *before* binding to an available donor, this case would be statistically irrelevant, and the spectrum would still be governed by the statistically relevant (D^0,X) transition.
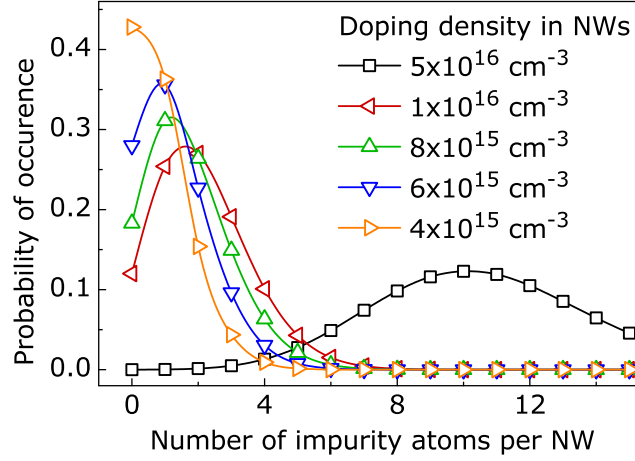
Figure 6.13.: Probability that a certain number of donors is incorporated into a single NW with a diameter of 30 nm and a length of 300 nm. This number follows Poissonian statistics. The probability distribution is shown for various donor concentrations.

Donor concentration in free-standing nanowires

Considering the present free-standing NWs with a volume of around $2 \times 10^{-16}\,\text{cm}^3$, the number of donors per NW follows a Poisson distribution:

$$P_\nu(k) = \frac{\nu^k}{k!}e^{-\nu}. \tag{6.3}$$

$P_\nu(k)$ denotes the probability that a NW contains k impurity atoms. ν describes the probability of a certain atom to be an impurity. It depends on the NW volume and the doping density. $P_\nu(k)$ is plotted for various doping densities in Fig. 6.13. Only for donor densities on the order of $(6-8) \times 10^{15}\,\text{cm}^{-3}$, about 25% of the NWs are found to be free of donors ($k = 0$). These densities are about one order of magnitude smaller than the typical impurity concentration obtained in unintentionally doped GaN layers. However, Sanford *et al.*[163] have reported even lower donor densities of 10^{14} to $10^{16}\,\text{cm}^{-3}$ for GaN NWs. From the resulting donor concentration, we estimate that *on average* one to two donors per NW are expected.

It is important to note that the term "donor concentration" cannot be applied when *single* NWs are considered. A donor concentration is defined as the density of donors. In order to define such a density, a sufficiently large number of donors, i.e., a sufficiently large crystal volume, is necessary. In other words, doping is a statistical concept. When the crystal volume is reduced to a size at which *on average* only one or two donors can be found, the *actual* number of donors in a specific NW is subject to statistical fluctuations according to Poisson statistics. While a doping concentration can be specified for a (macroscopic) NW ensemble, it loses its meaning when a (microscopic) NW is considered.

Quantitative analysis of donor-bound exciton recombination in free-standing nanowires

Although with about 25% the number of donor-free NWs in the trichromatic area maps depicted in Fig. 6.10 is relatively large, the majority of free-standing NWs exhibits donor-bound exciton transitions. Whether or not the involved donor is close to the surface is re-

(a) NW spectrum of sample 30927 dominated by (D⁰,X) recombination.

(b) NW spectrum of sample 30887 dominated by FX recombination.

i	E_i (eV)	A_i	w_i (meV)	r_i
1	3.447	2.42	33.9	71
2	3.464	5.65	18.3	309
3	3.470	0.99	2.7	366
4	3.471	16.24	9.8	1655

i	E_i (eV)	A_i	w_i (meV)	r_i
1	3.453	1.30	36.2	36
2	3.473	0.48	4.0	121
3	3.474	3.44	16.1	214
4	3.480	3.21	5.8	551
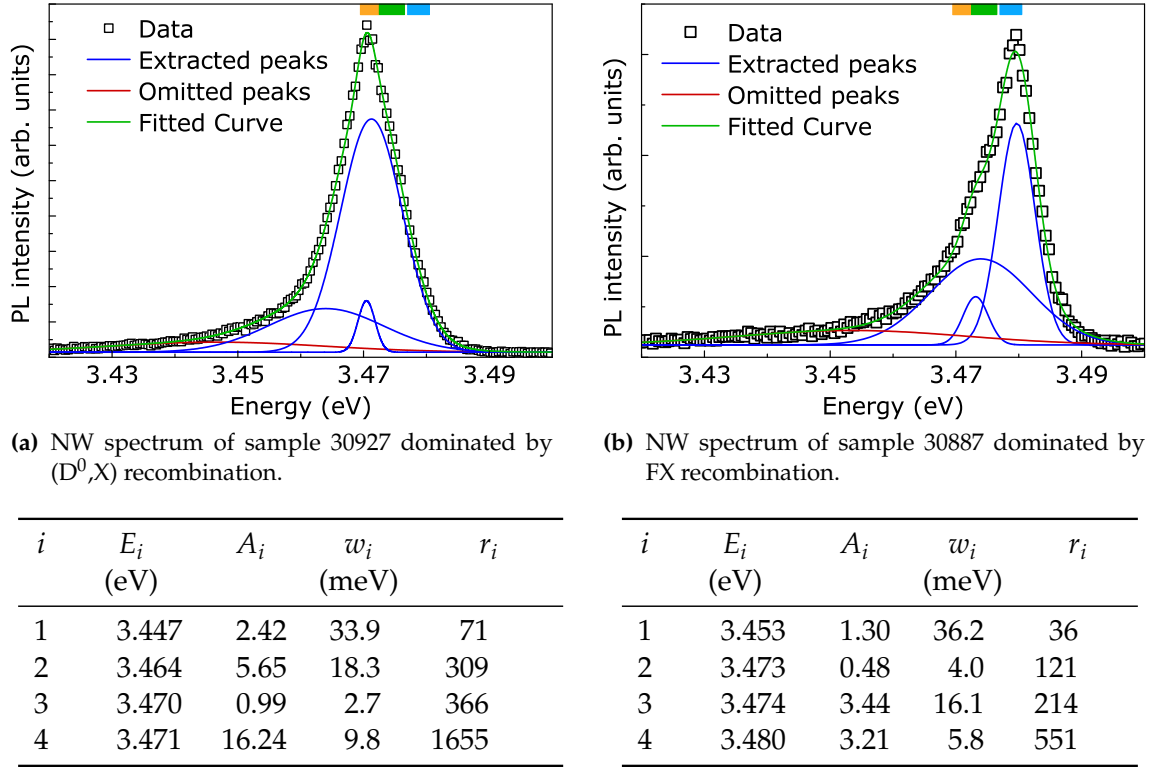
Figure 6.14.: Exemplary PL spectra of free-standing NWs of samples 30887 and 30927. The spectra are fitted with four Gaussians representing the 3.45 eV band, the (D⁰,X), (D⁰,X)$_s$, and FX transitions. The green line depicts the fitted curve as sum of the four Gaussians. In the Tables below the graphs, the fitting parameters are given for the four peaks of each set of Gaussians. In the last column, the respective ratios r_i are given. Peaks with $r_i < 0.1\,r_{max}$ are marked red in the graphs. They are omitted from the further analysis.

vealed by the peak energy of the respective line in the PL spectrum. Both area maps contain a large number of green spots indicating the presence of surface donors. The number of red/orange spots representing bulk donors is, in contrast, rather small. However, due to the relatively large linewidths, a green spot may represent a spectrum that contains in addition to the dominant (D⁰,X)$_s$ transition minor contributions from (D⁰,X) or FX recombination. The corresponding spot in the trichromatic area map would nonetheless appear green. In order to unravel these hidden contributions, a detailed quantitative analysis of the area maps is performed. As the area maps contain several thousand spectra, an automated algorithm is used to perform this analysis.

For this analysis, each spectrum that exceeds a certain intensity threshold is fitted with a set of four Gaussians i, representing the 3.45 eV band and the (D⁰,X), (D⁰,X)$_s$, and FX transitions. For each set of Gaussians, the peak energy E_i, the area A_i, the FWHM w_i, and the ratio of area and FWHM $r_i = A_i/w_i$ is determined. r_{max} is given by the maximum value of r_i for each set of Gaussians. Only peaks with $r_i \geq 0.1 r_{max}$ are considered for the further analysis in order to diminish the influence of spurious signals due to noise. The intensity threshold as well as the threshold for r_i are chosen such that first, the resulting peak distributions are stable against slight variations of these thresholds and second, as many peaks as possible are analyzed. Two exemplary spectra from the area maps

(a) Histogram of peak energies for sample 30927 grown on Si(001).

(b) Histogram of peak energies for sample 30887 grown on Si(111).
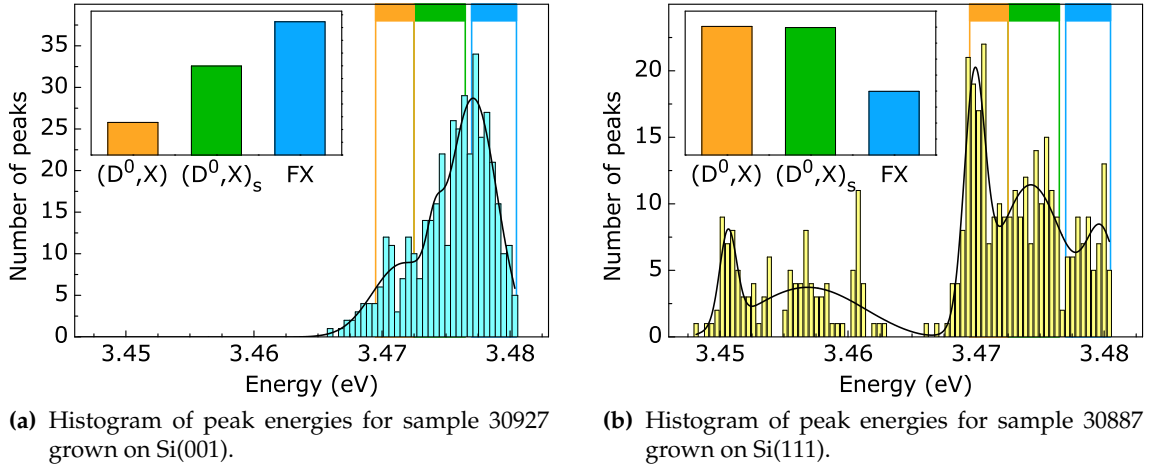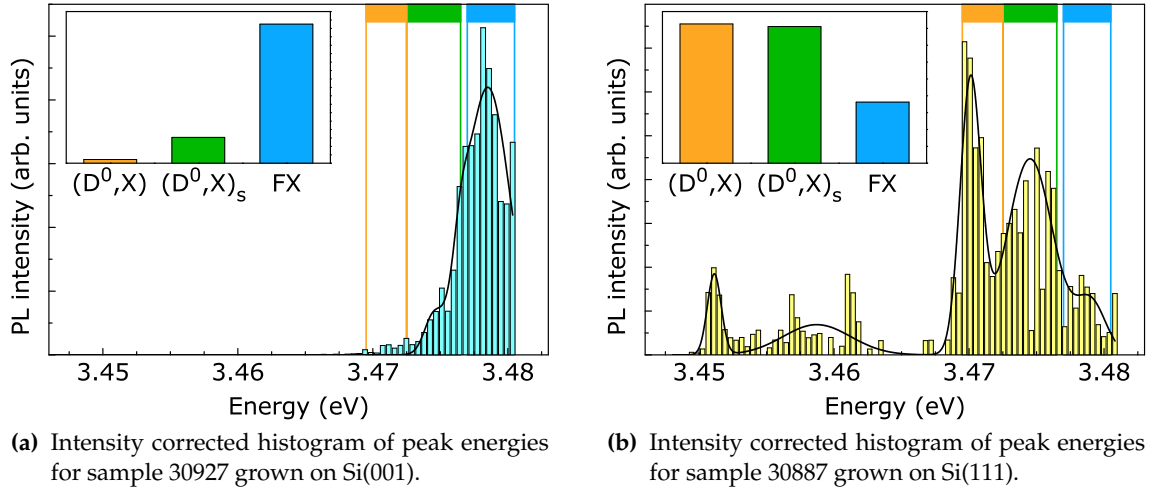
Figure 6.15.: Results of the quantitative analysis of the trichromatic area maps shown in Fig. 6.10. The histograms show the number of peaks with specific energies in these area maps. The black lines visualize the transitions found in the maps. The insets of show the relative occurrence of the three near-band-edge transitions. The spectral ranges of the (D^0,X), $(D^0,X)_s$, and FX transitions are illustrated by the correspondingly colored bars at the top of the graphs.

of samples 30887 and 30927 are shown in Fig. 6.14 together with the respective sets of fitted Gaussians. The orange curves represent peaks that are omitted as their ratio r_i is smaller than $0.1r_{max}$ (cf. respective Tables in Fig. 6.14). The blue Gaussians are taken into account for the quantitative analysis. The results of this analysis are presented in Figs. 6.15 and 6.16.

The distributions of peak energies found in the area maps are shown in Figs. 6.15(a) and 6.15(b), while the histograms in Fig. 6.16(a) and 6.16(b) display the intensity of the respective transitions. For both samples, the strongest contribution to the PL signal is between 3.466 and 3.481 eV. In addition, sample 30887 exhibits a weak PL signal around 3.45 eV. The presence of this band is consistent with the ensemble measurements shown in Fig. 6.9, where the 3.45 eV band is much stronger for sample 30887 than for sample 30927 grown on Si(001). Of particular interest is the near-band-edge region. Here, significant contributions (in terms of numbers as well as intensity) from the $(D^0,X)_s$ as well as from the FX can be found. The insets of Figs. 6.15(a) and 6.15(b) and of Figs. 6.16(a) and 6.16(b) depict the relative occurrence and the relative intensities of the (D^0,X), the $(D^0,X)_s$, and the FX transitions. In the PL of sample 30927, about 50% of the transitions originate from FX recombination. Their intensity even accounts for more than 80% of the overall near-band-edge PL. For sample 30887, about 20% of the transitions represent the FX. Their intensity is of the same order. The results of the quantitative analysis of the area maps thus support the conclusion drawn before: a significant number of NWs is free of donors.

Furthermore, the number of surface donors in sample 30927 is larger than in sample 30887 similar to the number of bulk donors. This finding is actually not surprising. As previously mentioned, the free-standing NWs are slightly smaller than their ensemble counterparts, having a diameter of about 30 nm. Consequently, their surface-to-volume ratio is increased. Using Eq. 6.2, the percentage of surface donors can be estimated to be about 70%. Figures 6.16(a) and 6.16(b) and in particular their respective insets confirm

69

(a) Intensity corrected histogram of peak energies for sample 30927 grown on Si(001).

(b) Intensity corrected histogram of peak energies for sample 30887 grown on Si(111).

Figure 6.16.: Results of the quantitative analysis of the trichromatic area maps shown in Fig. 6.10. The histograms show the number of peaks with specific energies in these area maps weighed for their intensities. The black lines visualize the transitions found in the maps. The insets show the relative intensity of the three near-band-edge transitions. The spectral ranges of the (D^0,X), $(D^0,X)_s$, and FX transitions are illustrated by the correspondingly colored bars at the top of the graphs.

the significance of the $(D^0,X)_s$ transition not only in terms of numbers but also in terms of intensity.

The differences between the two samples may be a consequence of slightly different growth conditions. Especially a slight variation of the substrate temperature may change the amount of incorporated impurities on the one hand and the NW dimensions on the other hand. A reduction of both increases the probability of donor-free NWs. Another apparent difference is the substrate orientation, which might affect the optical properties of the NWs. For instance, the indiffusion of Si from the substrate into the NWs may occur to a different degree and thus lead to different average doping concentrations.

6.3. Conclusions

The investigation of single NWs, either dispersed or free-standing, leads to the important finding that the optical properties of NWs are strongly affected by their large surface-to-volume ratio. First, the number of surface donors is significantly increased and thus radiative $(D^0,X)_s$ transitions contribute to the luminescence of NWs. They represent the intrinsic origin of the commonly observed rather large linewidths observed in NW ensemble measurements. A second significant finding obtained from experiments with single, free-standing NWs is the rather low doping concentration in the NWs, which eventually leads to the presence of a significant number of donor-free NWs. The inherent consequence is that the optical properties of individual NWs may strongly vary, and an extrapolation from ensemble properties to the characteristics of single NWs is not applicable. This is of particular importance for the fabrication of devices based on single NWs, where a high reproducibility is crucial.

7. Electric fields in GaN nanowires - Fermi level unpinning

As shown in Sec. 2.3, the pinning of the Fermi level at the NW sidewalls leads to the presence of electric fields. Especially, the region close to the surface is affected by electric fields if the Fermi level is pinned at the NW sidewalls. Due to the large surface-to-volume ratio in NWs, such surface-related effects may have particular significance for their optical and electrical properties. In the following, electric fields in unintentionally doped NWs are investigated. First, a brief introduction into the correlation between the donor concentration, the Fermi level pinning, and the electric fields for the case of NWs will be given. In the second part, the desorption process of oxygen from the surface of the GaN NWs will be discussed. In this context, the correlation of the electric fields in the NWs with their optical properties will be investigated. The results presented here have been published in Ref. 166.

7.1. Band profile and electric fields in unintentionally doped GaN nanowires

The band profile in semiconductor NWs critically depends on the NW diameter. Calarco *et al.*[75] have shown that for a NW with a donor concentration N_d, a critical diameter d_{crit} exists, below which the NWs are fully depleted. These NWs do not conduct electric current. In NWs with $d > d_{crit}$, however, a conducting channel is formed in the center of the NW. With decreasing N_d, the critical diameter d_{crit} increases.

These results implicate that unintentionally doped NWs as investigated in the present work are in general fully depleted. Considering a GaN layer, the width w_L of the depletion region at the surface can be calculated by:[67]

$$w_L = \sqrt{\frac{2V_b \varepsilon_s}{e N_d}} . \tag{7.1}$$

Assuming a donor concentration of $N_d = 5 \times 10^{16}\,\mathrm{cm}^{-3}$ and a Fermi level pinning of about $0.6\,\mathrm{eV}$ below the conduction band edge,[68,75] the depletion width amounts to roughly $150\,\mathrm{nm}$ and thus by far exceeds the average NW diameter of about $40\,\mathrm{nm}$.

The actual band profile across a NW can be determined by solving Poisson's equation in cylindrical geometry (Eq. 2.29), which simplifies to a parabolic form for fully depleted NWs (see Eq. 2.30).

Figure 7.1(a) depicts a comparison of the conduction band profiles across a fully depleted NW with a diameter of $40\,\mathrm{nm}$ and a thick GaN layer based on simulations using the program 1DPOISSON.[167] The entire NW volume is depleted, and therefore, the band profile across the NW is rather flat compared to the band profile close to the surface of the layer. Despite the complete depletion of the NW, the most important implication of this finding is that the value of the electric field strength at the NW surface is rather small,

(a) Conduction band profile across a GaN NW with a diameter of 40 nm and a donor concentration of $5 \times 10^{16} \, \mathrm{cm}^{-3}$. The band profile is compared to that of a GaN layer with the same donor concentration.

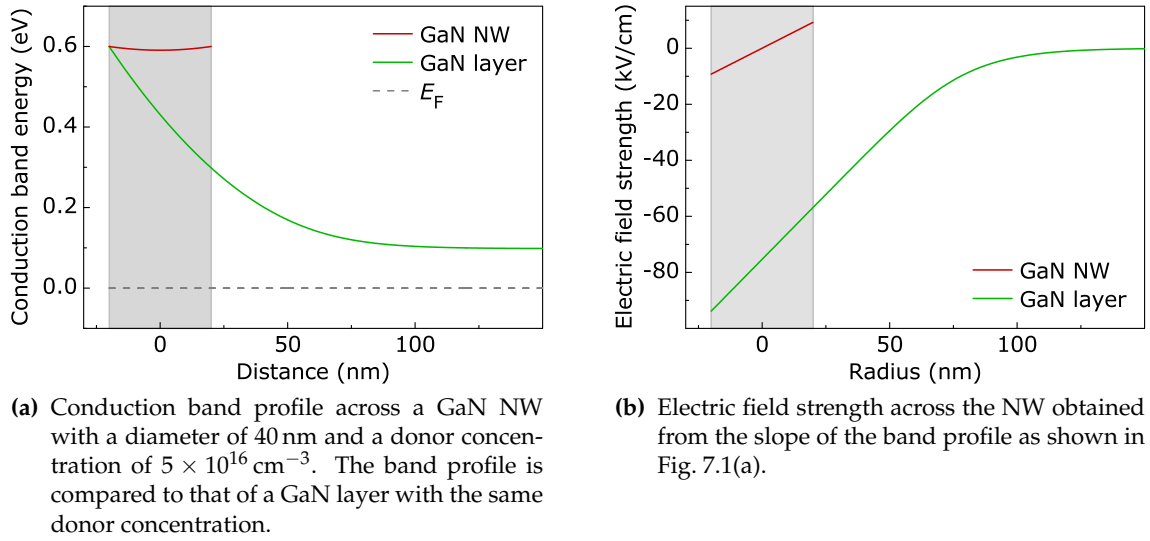**(b)** Electric field strength across the NW obtained from the slope of the band profile as shown in Fig. 7.1(a).

Figure 7.1.: Simulation of the band profile and the electric field strength in a GaN NW and in a thick GaN layer. The gray shaded area indicates the vertical cross section of the NW. The depicted band profile and electric field distribution are obtained from simulations based on 1DPOISSON.

taking values on the order of 10 kV/cm. A comparison of the electric field strength in a fully depleted NW and in a thick GaN layer is shown in Fig. 7.1(b). Another implication is interesting for the optical properties of such NWs. Aside from a line along its center axis, no field-free region exists within the NW.

In order to stress the significance of this finding, the effects of the electric field on excitonic recombination, namely, a dramatic quenching of the PL, have to be considered. By applying a small electric field, the opposite charges in the exciton are pulled apart and eventually may ionize the exciton.[58] Consequently, the radiative recombination efficiency is decreased. This effect depends exponentially on the field strength. Thus, even small electric fields of several 10 kV/cm can quench the excitonic luminescence completely.[58]

For the investigated NWs, the presence of these small electric fields implies that the observed PL signal is in a partially quenched state. A similar conclusion can be drawn for NW-based devices such as LEDs, where the active region is usually undoped and therefore subject to these lateral electric fields. In the following, it will be discussed to which extent the excitonic recombination may be quenched.

7.2. Oxygen desorption from GaN nanowire sidewalls under ultraviolet illumination

Performing PL experiments on many GaN NW ensembles, we observed a recurring phenomenon. When the GaN NWs are exposed to UV light, e.g., to the HeCd laser which has a wavelength of 325 nm, the PL intensity increases with exposure time. This phenomenon occurs irrespectively of the MBE system the NWs were grown in.

Figure 7.2 shows the near-bandgap spectrum of a GaN NW ensemble (sample 30887) at the beginning (black) and after 90 min (red) of continuous exposure to the UV laser. The

Figure 7.2.: Evolution of the PL signal of sample 30887 under continuous exposure to UV light. The measurements were performed at $10\,\mathrm{K}$ with an excitation density of $10^{-5}\,I_0$. The black curve is recorded after $1\,\mathrm{s}$ and the red curve after $90\,\mathrm{min}$ of UV illumination.
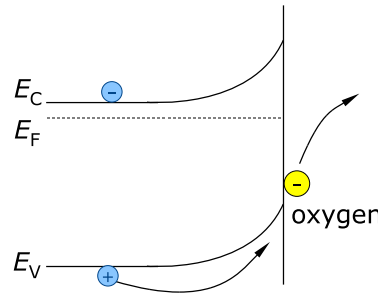

Figure 7.3.: Schematic illustration of the photoinduced desorption of oxygen from semiconductor surfaces.

intensity of the (U,X) and in particular of the (D^0,X) line increases considerably when the sample is exposed to UV light. As long as the NWs are in vacuum, this effect takes place regardless of the excitation density or temperature. Room-temperature experiments allow us to vent the cryostat with air, while the luminescence is recorded. An instantaneous drop of the PL intensity is observed when the cryostat is vented with air, while pure N_2 does not affect the PL intensity. This behavior implies that the observed PL intensity evolution is related to oxygen. As a matter of fact, it is a well-known phenomenon in surface chemistry that oxygen is ionosorbed on semiconductor surfaces. The photoinduced desorption of ionosorbed oxygen from ZnO surfaces has been studied already in the late 1950s. A comprehensive survey is given in the book of Morrison.[168] Photogenerated holes are transferred from the bulk to the surface, where they neutralize negatively charged ionosorbed oxygen. This process is depicted schematically in Fig. 7.3.

Considering GaN layers, only few studies are available.[69,169] They report an increase in PL intensity of up to 40% depending on the donor concentration. In these studies, the oxygen is desorbed from the *C*-plane surface of the GaN layers. For the NWs, we observe a much more pronounced increase of the PL intensity by a factor of 2 to 5, depending on the experimental conditions such as temperature and excitation density. Here, the major part of the desorbed oxygen originates from the *M*-plane sidewalls of the NWs. Contri-

(a) Measurement of sample 30887 at 10 K and with an excitation density of $10^{-5} I_0$. The laser has been turned off after 90 min of illumination to allow for readsorption.

(b) Room-temperature measurement of sample M8849 at an excitation density of $10^{-3} I_0$.
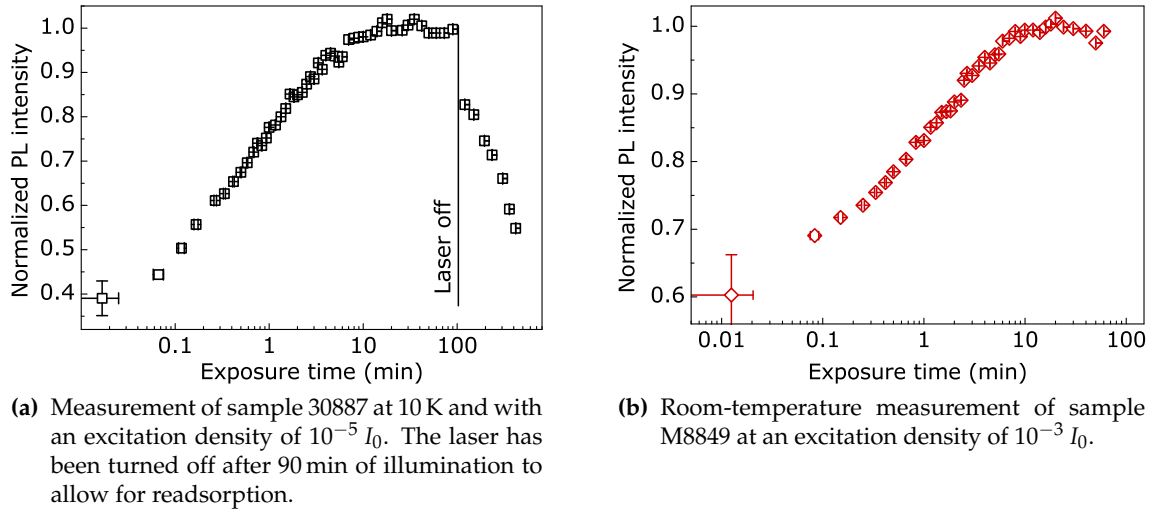
Figure 7.4.: Evolution of the integrated PL intensity during exposure of two GaN NW ensembles to UV illumination. The samples have been grown in different MBE systems. Note the logarithmic time scale in both graphs.

butions from the C-plane top facet is neglected in the following considerations. Figure 7.4 shows examplary the temporal evolution of the integrated PL intensity for two GaN NW ensembles (sample 30887 and sample M8849) grown in different MBE systems. Samples 30887 [Fig. 7.4(a)] and M8849 [Fig. 7.4(b)] are probed at 10 K and room temperature, respectively. In both cases a dramatic increase of the PL intensity can be observed, which takes several minutes before the intensity saturates. Note the logarithmic time scale in the graphs.

Kinetic model of oxygen desorption from nanowire ensembles

In order to achieve further insight into the desorption process in a NW ensemble, the temporal evolution of the PL intensity is investigated over a period of several hours [cf. Fig. 7.4(a)]. A schematic description of the desorption process is depicted in Fig. 7.5. The UV laser is turned on at $t = 0$. At this point [(A) in Fig. 7.5], the NWs are entirely covered with oxygen. After 90 min, the continuous UV exposure is stopped. During this time, several PL spectra are recorded at specific time steps. The PL intensity increases monotonously in an essentially logarithmic manner [note the logarithmic time scale in Fig. 7.4(a)] as the oxygen coverage decreases [(B) in Fig. 7.5] and saturates at a value about 2.6 times larger than the initial intensity [(C) in Fig. 7.5]. This process takes about 10 min. After 90 min, the laser is turned off to allow for readsorption of oxygen. Each data point in Fig. 7.4(a) corresponds to a spectrum with an integration time of 1 s. The error bar lies within the symbol size except for the first data point, where the simultaneous turn-on of the laser and detector unit leads to an error in the PL intensity of 10%.

For monitoring the readsorption process [(D) in Fig. 7.5], the PL signal is recorded after stopping the continuous illumination. This means that the NWs are exposed to the laser only for the time necessary to record the spectra. However, during this exposure to UV light, readsorbed oxygen, the partial pressure of which is about 10^{-7} mbar in the cryostat, is again desorbed. Hence, a quantitative analysis of the readsorption process is
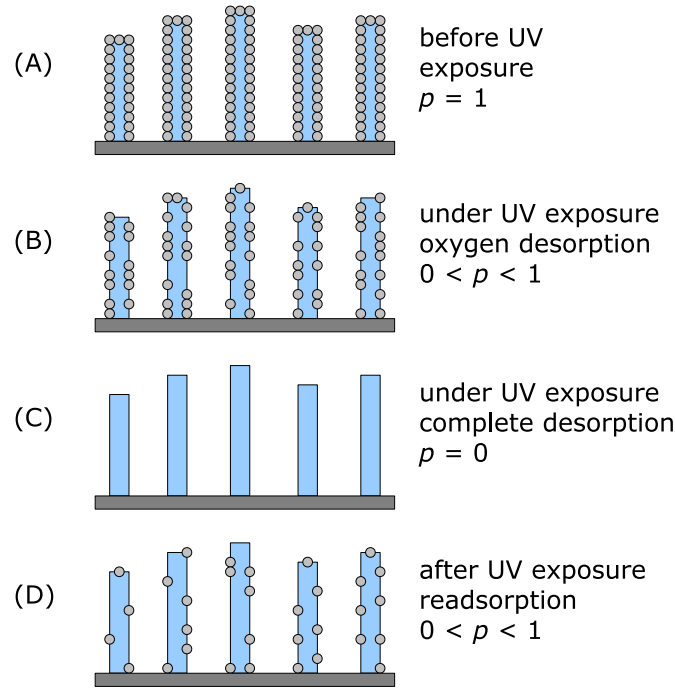
Figure 7.5.: Schematic description of the oxygen desorption process in a NW ensemble. The gray spheres represent adsorbed oxygen, p denotes the oxygen coverage averaged over the entire NW ensemble. (A) Before exposure of the NWs (blue) to the UV light, the NWs are completely covered with oxygen. (B) After turning the laser on, oxygen is desorbed, and the PL intensity increases. (C) When the oxygen is completely desorbed, the PL saturates. (D) After turning the laser off, oxygen is readsorbed, and the PL intensity decreases.

difficult. Qualitatively, a clear readsorption of residual oxygen can be observed, since the PL intensity slowly decreases in Fig. 7.4(a).

Figure 7.6 depicts the evolution of the peak positions of the (D^0,X) and the (U,X) transition. Within the spectral resolution of the setup of 1 meV, the energy of both transitions remains constant throughout the experiment. This observation implies that the increase of the PL intensity is not caused by a change of the recombination channel, but rather by an enhanced recombination efficiency.

Obviously, the PL intensity is related to the oxygen coverage p of the NW surface averaged over the entire ensemble. p is a normalized quantity, which can be understood as the ratio of the oxygen-covered NW surface to the entire NW surface. According to first-order desorption kinetics, an exponential decay of p may be expected. However, the temporal evolution depicted in Fig. 7.4 reflects a highly nonexponential decay of p. In other words, the desorption process is slower than expected.

To understand this discrepancy, the specific sample geometry has to be taken into account. Oxygen molecules desorbed from the sidewalls of NW a may encounter nearest-neighbor NWs $\{a\}$ and be readsorbed with a certain probability $0 \leq \kappa \leq 1$ as illustrated in Fig. 7.7(a). The limiting cases $\kappa = 0$ and $\kappa = 1$ correspond to zero and complete readsorption, respectively. The exact value of κ depends on the specific sample geometry, including the NW density and distribution and varies from NW to NW. If $\kappa > 0$, oxygen molecules may move from NW to NW before leaving the NW ensemble irrevocably. They perform a random-walk-like motion [see Fig. 7.7(b)], and therefore, the readsorp-
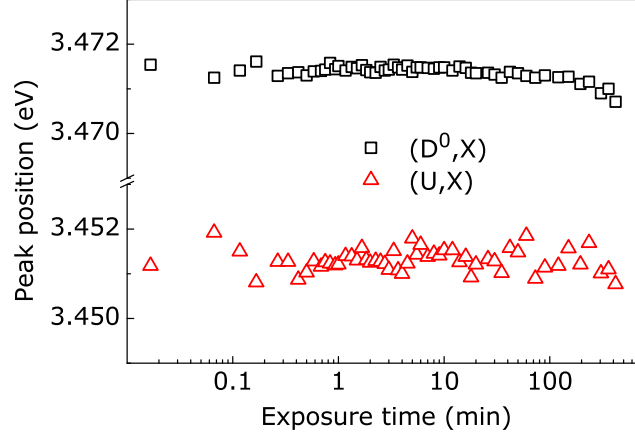
Figure 7.6.: Evolution of the (D^0,X) and (U,X) transition energies of sample 30887. Within the spectral resolution peak energies remain constant.
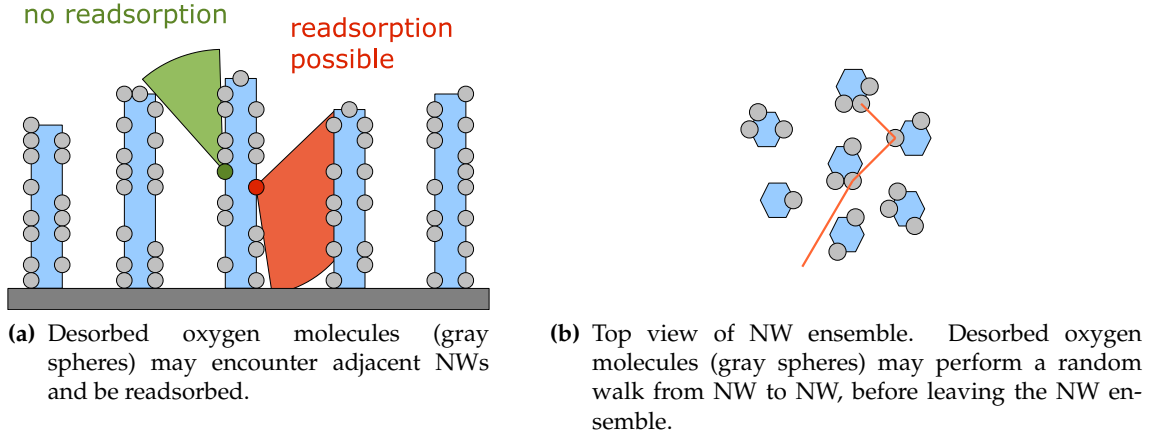

(a) Desorbed oxygen molecules (gray spheres) may encounter adjacent NWs and be readsorbed.

(b) Top view of NW ensemble. Desorbed oxygen molecules (gray spheres) may perform a random walk from NW to NW, before leaving the NW ensemble.

Figure 7.7.: Schematic description of the readsorption model.

tion process is prolonged for fundamental reasons.

Based on these considerations, we develop a model to simulate the temporal evolution of the PL intensity I_{PL} as a function of the oxygen coverage p. For simplicity, we consider the NWs to populate an equidistant square lattice. Furthermore, κ is averaged over the ensemble and thus treated as a constant. The oxygen desorption rate Γ depends on the excitation intensity I_{L}. Therefore, the Gaussian profile $\gamma(\vec{r})$ of the exciting laser yields a position-dependent desorption rate Γ. As a consequence, even in the case of layers ($\kappa = 0$), the oxygen coverage n decreases nonexponentially. More importantly, however, the desorption rate Γ varies from NW to NW.

As explained in the beginning of this section, holes are generated in the bulk of the material, and a certain fraction of them is then transfered to the semiconductor surface. There, they initiate the oxygen desorption and thus determine the desorption rate Γ. While the generation of electron-hole-pairs can be expected to scale linearly with I_{L}, the fraction of holes that eventually reach the surface is not proportional to I_{L}, as can be shown experimentally. To account for the resulting nonlinearity of Γ, a power-law dependence of Γ on the excitation intensity with an exponent b is assumed.

The normalized oxygen coverage $0 \leq p_a(t) \leq 1$ of the ath NW at position $\vec{r}_a$ can be
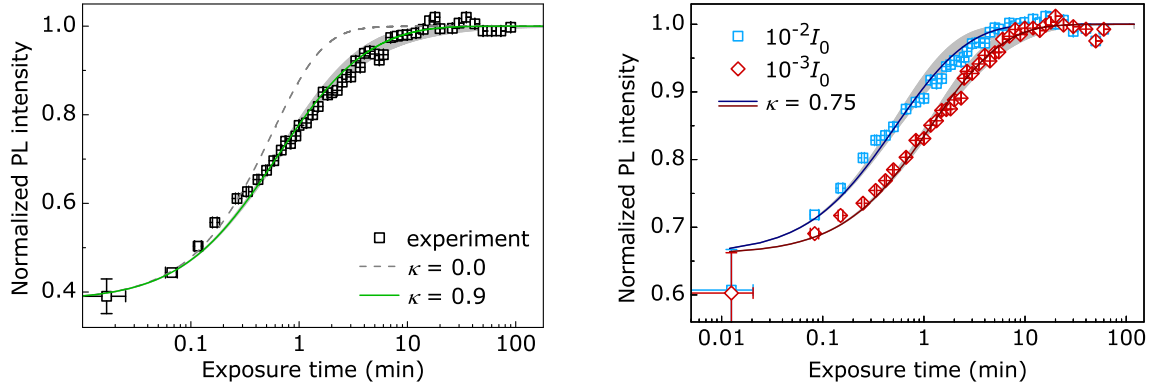
(a) Measurement of sample 30887 at 10 K. The experimental data are simulated with different readsorption probabilities κ. The gray shaded area depicts the range of high readsorption with $0.8 < \kappa < 1.0$. The green line represents a a simulation with $\kappa = 0.9$.

(b) Room-temperature measurements of sample M8849 at two different excitation densities. Both data sets are modeled with $\kappa = 0.75$, the gray areas depict the range of $0.5 < \kappa < 0.9$.

Figure 7.8.: Simulation of the PL intensity increase shown in Figs. 7.4(a) and 7.4(b). The simulations have been performed by F. Grosse.

described by a rate equation system:

$$\frac{dp_a(t)}{dt} = -\Gamma_a p_a(t) + \kappa \frac{1 - p_a(t)}{4} \sum_{i=\{a\}} \Gamma_i p_i(t). \qquad (7.2)$$

The factor $1/4$ accounts for the number of nearest neighbors $\{a\}$ of NW a, to which the summation on the right-hand side of Eq. 7.2 is restricted. Simulations including additional coupling to next-nearest-neighbor NWs do not affect the results significantly.

Initially, the oxygen coverage of the NWs is at its maximum, i.e., $p_a(t = 0)$ is set to 1. The PL intensity of the NW array can then be written as

$$I_{\mathrm{PL}}(t) = I_{p=0} + I_{p=1} \sum_a p_a(t)\,\gamma(\vec{r}_a)\,, \qquad (7.3)$$

where $I_{p=0}$ is the intensity at the minimum oxygen coverage. The initial intensity is therefore $I_{\mathrm{PL}}(t) = I_{p=0} + I_{p=1} \sum_a \gamma(\vec{r}_a)$ with $I_{p=1} \leq 0$ in the case of GaN.

Several parameters are taken from the experiment. First, the excitation density I_L and the diameter of the laser spot are determined by the experimental conditions. Second, the lattice spacing can be deduced from SEM images. The maximum PL intensity is equivalent to $I_{p=0}$, whereas $I_{p=1}$ is a parameter that scales the overall increase in PL intensity. Two remaining parameters have to be found by comparison with the experimental data. The readsorption process is described by κ and the exponent b. In principle, b is a measure for the fraction of photogenerated holes that reach the surface and eventually trigger the desorption of oxygen. To determine b, excitation-density-dependent measurements have to be modeled. Plotting the experimental data on a logarithmic time scale as in Fig. 7.4, b mainly shifts the simulated curve along the time axis. Within the error margin, it has no influence on the slope or curvature of the simulated curve. The slope and curvature are thus primarily determined by κ.

The simulation of the data obtained from sample 30887 and presented in Fig. 7.4(a) is

shown in Fig. 7.8(a). The gray shaded area depicts the relatively narrow range of high readsorption probability, for which the data set can be fitted satisfactorily. The best agreement is achieved for $\kappa = 0.9$. This simulation underlines that the desorption process is considerably prolonged as a significant amount of oxygen is readsorbed on adjacent NWs. This observation is thus consistent with first-order desorption kinetics. The case of no readsorption ($\kappa = 0$) is depicted by the dashed line. The faster desorption process is represented by the steeper slope. It clearly does not match the experiment. Therefore, a significant amount of oxygen must be readsorbed.

Figure 7.8(b) shows the simulation of two room-temperature desorption measurements of sample M8849 [cf. Fig. 7.4(b)] at different excitation densities (blue squares $10^{-2}\,I_0$, red triangles $10^{-3}\,I_0$). According to the model, the excitation density does not affect the readsorption probability κ. Indeed, both data sets can be simulated consistently using the same value for κ. The gray area depicts the range of $0.5 < \kappa < 0.9$ with the blue and the orange line representing simulations for $\kappa = 0.75$, which match the respective data sets. Again, a relatively high readsorption probability is observed.

The exponent b can be deduced from the temporal shift between the two curves. This shift corresponds to $b = 0.34$. Measurements at even lower or higher excitation densities are more difficult due to experimental constraints. On the one hand, the PL signal is too weak to be recorded within a feasible integration time at lower excitation densities. On the other hand, the initial increase of the PL intensity is too fast to be resolved when the excitation density is increased. Thus, the range of applicable excitation densities is limited to one order of magnitude, and a more detailed analysis of the excitation density dependence of the desorption process is difficult. Nonetheless, the obtained value for $b < 1$ allows the conclusion that the fraction of photogenerated holes reaching the NW surface decreases with increasing excitation density.

Time-resolved desorption experiments

The long-term evolution of the NW PL intensity can be explained with the model presented above. It reveals that the desorption process is governed by readsorption of previously desorbed oxygen. The microscopic origin of the PL intensity increase, however, is not clarified by this model. In order to identify the mechanisms responsible for the observed increase in the PL intensity, the evolution of the decay dynamics has been studied by TRPL experiments.

The experimental conditions in the TRPL setup are chosen to be as close as possible to the ones in the cw-PL measurements. The sample is placed in a vacuum cryostat and cooled down to 10 K. The excitation wavelength is 325 nm, but due to a much larger spot size the average excitation density is considerably lower. However, in contrast to the cw-PL measurements, the excitation is pulsed in TRPL experiments. Consequently, the desorption process is pulsed. In between individual laser pulses, i.e., without laser irradiation, readsorption may take place. This readsorption has also been observed in cw-PL experiments after turning off the laser [cf. the last data points in Fig. 7.4(a)]. The exact temporal dependencies of the desorption process in cw-PL and TRPL may therefore differ. The long-term temporal evolution of the PL intensity, however, will by essentially identical. In both cases, a significant PL intensity increase can be observed.

Figure 7.9(a) depicts the spectrally integrated transients of sample 30887 after 8 s, 49 s, and 17 min of exposure to the pulsed UV laser. Each transient shows a clearly nonex-

(a) Spectrally integrated transients after 8 s, 49 s, and 17 min of exposure to pulsed UV light. The data are fitted with a biexponential decay represented by the solid lines.

(b) Spectrally resolved transients for the (D^0,X) and (U,X) transition after 17 min of exposure to pulsed UV light. The solid lines represent biexponential fits with $\tau_{D,nr}$ and $\tau_{U,nr}$ denoted in the graph.
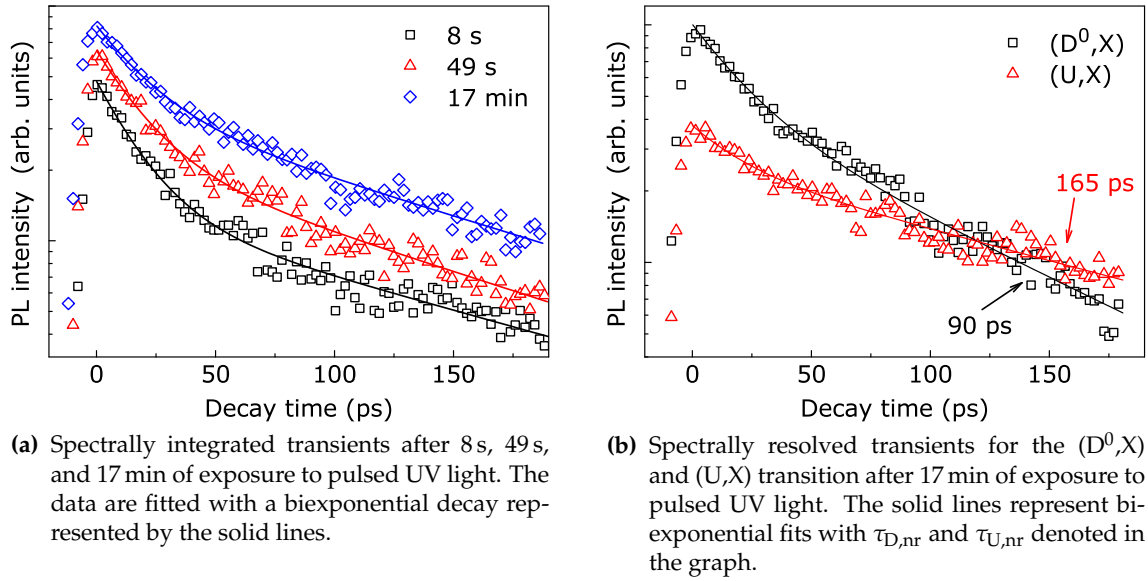
Figure 7.9.: Evolution of the time-resolved PL signal of sample 30887 under pulsed UV excitation. The experiment was carried out at 10 K.

ponential decay, which can be fitted by a biexponential decay function[a] with the two effective decay constants $\tau_{short} \approx 20$ ps and $\tau_{eff} \approx 140$ ps. Both decay constants basically remain constant throughout the experiment. Radiative lifetimes on the order of 1 ns[138] have been reported for GaN. Hence, the decay in the NWs is governed by nonradiative recombination processes ($\tau_{eff} \approx \tau_{nr}$, see Eq. 2.18). At room temperature, the nonradiative surface recombination velocity S has been determined to 9×10^3 cm/s.[104] Assuming that S is of similar magnitude at low temperatures, this value translates into an effective lifetime of about 100 ps for NWs with a diameter of 40 nm (cf. Eq. 4.1), indicating that the lifetime in the NWs is indeed limited by the nearby surface. Upon oxygen desorption, the NW surface is modified. Therefore, the increase of the PL intensity by a factor of 2 to 5 is expected to be reflected in an equivalent increase of τ_{nr}. However, such an increase is not observed.

A detailed analysis of the (D^0,X) and (U,X) transitions shows that τ_{short} is not affected at all by the desorption of oxygen. Therefore, it will be neglected in the following analysis. Regarding τ_{nr}, we will show in the following that the (D^0,X) and the (U,X) transitions exhibit clearly different recombination dynamics. First of all, the transients of both transitions after 17 min of UV exposure are depicted in Fig 7.9(b). The (U,X) complex exhibits a longer decay time of $\tau_{U,nr} = 165$ ps than the (D^0,X) transition ($\tau_{D,nr} = 95$ ps). Second, as shown in Fig. 7.10(a), the nonradiative recombination time $\tau_{U,nr}$ remains constant at about 165 ps throughout the experiment. In contrast, $\tau_{D,nr}$ increases from about 60 to 100 ps. Third, the temporally integrated intensity of the two transitions increases by a different factor: 4.7 for the (D^0,X) and 2.4 for the (U,X) transition. The corresponding evolution of the PL intensities is plotted in Fig. 7.10(b). Table 7.1 gives an overview of

---

[a]In Chap. 8, it will be shown that the assumption of a biexponential decay is not strictly valid. Here, however, it is an acceptable approximation.

(a) Evolution of the PL decay times $\tau_{D,nr}$ and $\tau_{U,nr}$ of the (D^0,X) and the (U,X) transition.

(b) Evolution of the temporally integrated PL intensities of the (D^0,X) and the (U,X) transition.
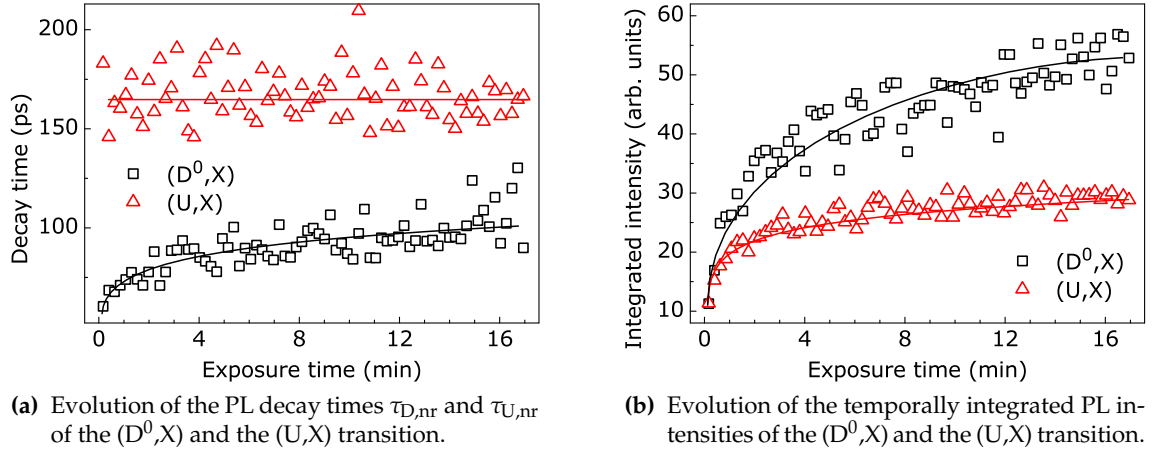
Figure 7.10.: The evolution of the PL decay times and the PL intensities of the (D^0,X) and the (U,X) transition of sample 30887 under pulsed UV exposure. The lines in both graphs serve as guides to the eye.

Table 7.1.: Overview of the factors contributing to the increase in PL intensity of sample 30887 under pulsed UV exposure.

	(D^0,X)		(U,X)	
	progress	factor	progress	factor
integrated intensity (arb. units)	$110 \rightarrow 520$	4.7	$120 \rightarrow 290$	2.4
effective lifetime τ_{eff} (ps)	$60 \rightarrow 100$	1.6	165	1
intensity at $t = 0$ (arb. units)	$40 \rightarrow 85$	2.1	$15 \rightarrow 35$	2.4

the factors contributing to the increase of the PL intensity. The discrepancy between the extent of the intensity increase and the change of τ_{nr} implies that contrary to intuition the nonradiative surface recombination rate is not sufficiently decreased to explain the observed PL intensity increase. In fact, it is rather the radiative recombination rate that is enhanced to a large extent.

In Fig. 7.9(a), a clear increase of the initial PL intensity $I_0 = I(t = 0)$ can be identified. The evolution of $I_{D,0}$ and $I_{U,0}$ under pulsed UV exposure is depicted in Fig. 7.11(a). Brandt *et al.*[143] have shown that I_0 is directly proportional to the radiative recombination rate γ_r or in other words

$$I_0 \propto \gamma_r \propto \frac{1}{\tau_r}. \tag{7.4}$$

Equation 7.4 is valid under the assumption that all recombination processes involved are long in comparison to the excitation pulse. In the present case, this requirement is fulfilled. Having a duration of 200 fs, the excitation pulse is about two orders of magnitude shorter than the fastest recombination processes involved. The relation between I_0 and τ_r can be best illustrated assuming the complete absence of nonradiative recombination channels. In this case, every recombination process will contribute to the PL intensity. Figure 7.11(b) depicts the transients of three samples with different radiative recombination rates (solid lines). As, by definition, the three samples are equally excited,

(a) Evolution of $I_0 = I(t = 0)$ of the (D^0,X) and the (U,X) transition of sample 30887 under pulsed UV exposure. The lines serve as guides to the eye.

(b) Transients of samples with different radiative lifetimes τ_r. If no nonradiative recombination is present, the slope is determined by τ_r (solid line). The dashed lines illustrate the decay if a dominant *nonradiative* recombination channel is allowed ($\tau_{nr} \ll \tau_r$).
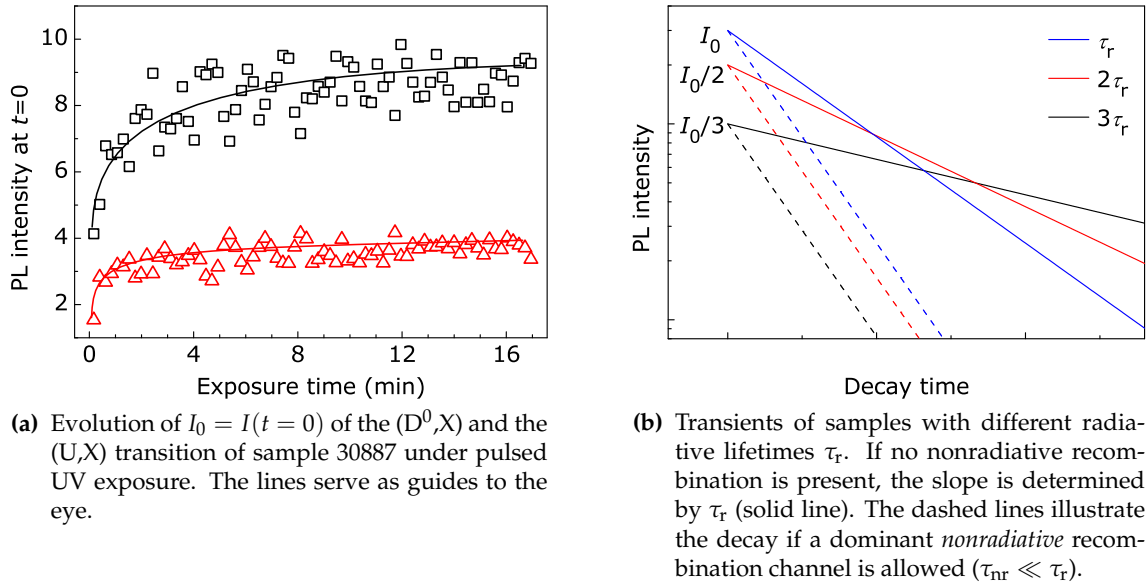
Figure 7.11.: Correlation between initial PL intensity $I_0 = I(t = 0)$ and radiative lifetime.

the same number of electron-hole pairs is generated. Since only radiative recombination is allowed, the temporally integrated PL intensity must be equal in all three cases. Consequently, the initial intensity I_0 has to increase for decreasing τ_r, as described by Eq. 7.4. If nonradiative recombination is allowed, the derivation of this relation, which can be found in the Appendix of Ref. 143, is considerably more complex. In the case of one dominating nonradiative recombination channel ($\tau_{nr} \ll \tau_r$), which is equally present in all three samples, the slope of the transients is governed by τ_{nr} [dashed lines in Fig. 7.11(b)]. As long as $\tau_{nr} \ll \tau_r$, a decreasing radiative lifetime does not cause a change in the slope, but is only represented in the increasing initial intensity I_0.[b]

Note that a similar effect can be achieved when the number of generated excitons is increased. A possible mechanism would be an enhanced absorption, e.g., after desorption of an absorbing layer at the surface of the NWs. However, such a layer would have to be rather thick. Even in the extreme case of having a metal layer[c] on the NW surface, such a layer would have to be about 10 nm thick to absorb around 50% of the incoming photons. Transmission electron microscopy experiments, however, exclude the presence of such a layer. The increase of I_0 thus directly confirms that the origin of the increase in the PL intensity is not a change of the absorption of light, but rather an enhanced radiative recombination efficiency.

The radiative lifetime $\tau_{D,r}$ ($\tau_{U,r}$) decreases in the course of the desorption experiment by a factor of 2.1 (2.4), yielding a corresponding enhancement of the quantum efficiency η_D (η_U). An overview of the extent to which radiative and nonradiative lifetimes change during the experiment is given in Tab. 7.1. The increase of the intensity of the (U,X) transition is completely due to the enhanced radiative quantum efficiency, whereas the increase of the intensity of the (D^0,X) transition benefits from both, a decreasing nonradiative and an

---

[b]The integrated PL intensity is proportional to the internal quantum efficiency η_{int}: $I_{PL} = \int dt\, I(t) \propto \eta_{int} = \tau_{eff}/\tau_r$. For pure radiative recombination, $\tau_{eff} = \tau_r$ and I_{PL} is constant for varying τ_r. If $\tau_{nr} \ll \tau_r$, $\tau_{eff} \approx \tau_{nr}$ and $I_{PL} \propto 1/\tau_r$.

[c]The absorption coefficient of metals is several orders of magnitude larger than the one of oxides such as Ga_xO_y, which are transparent to light of the excitation wavelength.
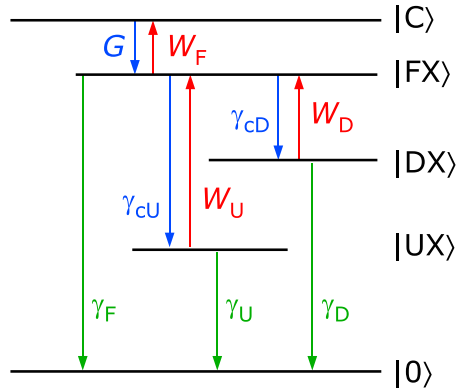
Figure 7.12.: Schematic description of the rate equation system as denoted in Eqs. C.2 in App. C. Here, the excitonic recombination processes in sample 30887 are illustrated.

increasing radiative recombination rate.

In accordance with the rate equation system for excitonic recombination introduced in Sec. 2.2, Fig. 7.12 illustrates the recombination and dissociation processes in the present system with generation and capture rates G, γ_{cD}, and γ_{cU}, dissociation rates W_i and recombination rates γ_i [$i = F, D, U$ for FX, (D^0,X), and (U,X), respectively]. In App. C, the rate equation system is examined in detail, leading to the result that the dissociation rates W_D and W_U decrease in the course of the experiment. As W_i depend on the electric field strength, this result suggests that the electric fields present in the NWs are reduced upon oxygen desorption.

Fermi level unpinning

The time-resolved measurements reveal that the observed increase of the PL intensity can be mostly ascribed to an enhancement of the radiative recombination efficiency. In Sec. 7.1, it has been shown that electric fields are present throughout the entire NW volume due to a pinning of the Fermi level at the NW sidewalls. Furthermore, the effect of electric fields on excitonic radiative recombination, namely a pronounced quenching of the luminescence, has been described (cf. Ref. 58). The electric field pulls apart the two involved opposite charges. The resulting blue-shift of the luminescence is almost exactly canceled by the quadratic Stark effect. Hence, a peak shift cannot be detected before the PL quenches.[58]

The peak energies of both, the (D^0,X) and the (U,X) transition, remain constant during the desorption process (see Fig. 7.6). The only mechanism that can explain these constant peak energies in conjunction with an increasing radiative recombination rate is the presence of an electric field in the NWs that is reduced upon oxygen desorption. Screening can be excluded as a mechanism, since the excitation density, and thus, the carier density remains constant throughout the experiment.

A change in the band bending will alter the associated electric field. Since the band profile is determined by the NW radius R, the donor concentration, and the Fermi level pinning and since both radius and donor concentration are not changed in the experiment, the unpinning of the Fermi level is the only possible mechanism explaining the

(a) Conduction band profiles for different values of the Fermi level pinning. The Fermi level E_F is at $E = 0$.

(b) Electric field strengths for different values of the Fermi level pinning.
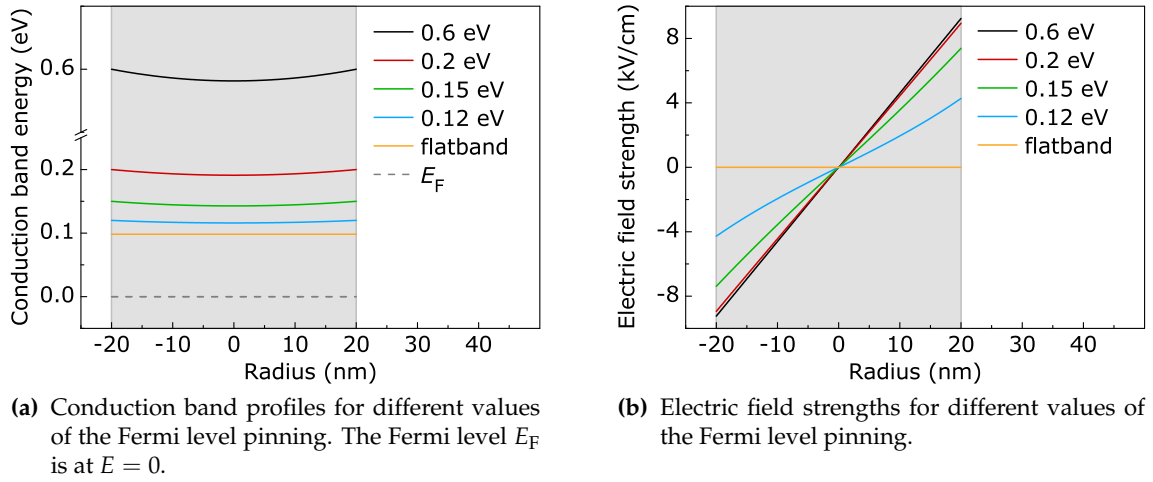
Figure 7.13.: Evolution of the conduction band profile and the electric fields across a NW with decreasing Fermi level pinning. The gray shaded areas indicate the vertical NW cross section. The plotted band profiles are based on simulations by the program 1DPoisson. The simulated NWs have a diameter of 40 nm and a doping concentration of $10^{16}\,\mathrm{cm}^{-3}$.

enhancement of the radiative recombination rate.

It is worthwhile to investigate in more detail the factors determining the strength of the electric field in the NWs. Three cases have to be distinguished:

"thick" NWs with $w \ll R$: Electric fields only occur in the depletion region. As described in Sec. 2.3, the Fermi level pinning and the donor concentration determine the depletion width and the resulting electric fields.

"thin" NWs with $w \gg R$: The Fermi level pinning only influences the height of the conduction band (cf. Eq. 2.30), while the electric fields are solely determined by the donor concentration (see Eq. 2.33).

"intermediate" NWs with $w \approx R$: The description of these NWs is more complicated, since there is a smooth transition between the two limiting cases. The electric fields are again determined by both, the donor density as well as the Fermi level pinning. However, even NWs having a radius slightly larger than w are fully depleted (see Ref. 76 for numerical calculations of w).

The conduction band profiles and the electric fields across a NW cross section for several values of the surface barrier are plotted in Fig. 7.13. If the Fermi level is larger than 0.2 eV, the electric field strength is not affected by a change of the Fermi level pinning, just as in "thin" NWs. However, if the Fermi level pinning drops below 0.2 eV, the transition from "thin" to "thick" NWs sets in, and the electric field strength is drastically reduced. Eventually, when the Fermi level becomes completely unpinned, the conduction and valence bands are flat. For the desorption experiment, these findings imply that the Fermi level pinning must be sufficiently reduced such that the "thin" NW limit becomes invalid.

Only few experimental data on the Fermi level pinning on *M*-plane GaN surfaces are available and theoretical calculations yielded contradictory results. Calculations by van

der Walle *et al.* [68] predicted the presence of intrinsic surface states due to dangling bonds inside the bandgap, with the exact position of the Fermi level pinning depending, for instance, on the growth conditions. [68,170] Experimentally, this result is supported by the work of Calarco *et al.* [75], who found the Fermi level pinning of 0.55 eV at the sidewalls of GaN NWs. Note that these NWs have been subject to an extensive processing involving an ultrasonic bath in a solvent. Hence, the surface of these NWs is most likely contaminated. Contrary theoretical results are obtained by Northrup *et al.* [74], who found no intrinsic states inside the bandgap of GaN. Consequently, the Fermi level is not pinned at clean *M*-plane surfaces, a finding that is confirmed by experimental studies. [171,172] Considering the desorption of oxygen from the *M*-plane sidewalls of GaN NWs as "cleaning" procedure, an unpinning of the Fermi level is consistent with the theoretical and experimental results in the literature.

7.3. Conclusions

The readsorption of atoms or molecules at NWs is not limited to the case of desorption of oxygen under UV exposure considered here, but may be extended to other processes, particularly those occurring during the synthesis of NWs. At elevated temperatures as found during the growth of NWs, desorption of Ga atoms or possible also of dopants from the NW surface is significant. Therefore, the readsorption processes described here will most likely influence the growth of NWs.

Furthermore, the results regarding the presence of electric fields have serious implications for future devices based on GaN NWs. For such devices, the passivation of the NW surface is crucial in order to control the band profile and electric fields in the NWs. Especially for the active region of light emitters that are usually undoped, the presence of undesired electric fields may have detrimental effects on the device performance.

8. External and internal quantum efficiency of GaN nanowires

A figure of merit for the performance of light-emitting semiconductor devices is the external quantum efficiency η_{ext}. It is defined as the emitted power divided by the injected power. In electrically driven devices, η_{ext} is includes the internal efficiency η_{int} and the extraction efficiency η_{out}. For the determination of η_{ext} by PL spectroscopy, the efficiency of the coupling of light into the semiconductor η_{in} has to be considered as well (see Sec. 2.2). In the present chapter, a route to the determination of η_{ext} for GaN NWs is introduced. In the first part, the combined efficiency $\eta_{\text{c}} = \eta_{\text{in}}\eta_{\text{out}}$ is accessed by comparing Raman spectra of a GaN layer and a GaN NW ensemble. In the second part, TRPL spectroscopy of GaN NWs is investigated with the goal to determine the internal quantum efficiency η_{int}.

8.1. Efficiency of coupling of light into and extraction of light out of GaN nanowires

Following Sec. 2.2, the external quantum efficiency is given by $\eta_{\text{ext}} = \eta_{\text{in}}\eta_{\text{int}}\eta_{\text{out}}$, where η_{in} denotes the fraction of the impinging light that is coupled into the crystal. If the photon energy of the light is larger than the bandgap, this light is absorbed and contributes to the generation of free carriers. η_{int} describes the fraction of electron-hole pairs, which recombines radiatively, leading to the emission of photons. These photons are only partly extracted from the semiconductor structure, and the fraction of extracted photons is given by η_{out}. In this section, $\eta_{\text{c}} = \eta_{\text{in}}\eta_{\text{out}}$ for a state-of-the-art GaN NW ensemble (sample M9257) will be estimated based on the comparison of the Raman signal of this NW ensemble and of a thick GaN layer (sample NAE_02042). Raman spectroscopy is performed using two different laser wavelengths, namely, the 482.5-nm line of a Kr^+ laser and the 632.8-nm line of a HeNe laser. For both wavelengths, GaN is transparent, while the Si substrate is opaque. This situation is schematically depicted in Fig. 8.1.

For a perfectly smooth layer, η_{in} can be calculated from the reflectance R (cf. Eq. 2.21). For a transparent layer, reflectance at the underlying substrate may be significant and must therefore be included. Using the transfer matrix method,[173] the reflectance R for such a stack can be calculated. R describes the fraction of light that is reflected from the sample (blue light in Fig. 8.1). The remaining fraction of light is transmitted by the layer and is finally absorbed in the substrate. The efficiency η_{in} is then given by:

$$\eta_{\text{in}} = 1 - R. \tag{8.1}$$

Side-by-side measurements of a GaN layer (sample NAE_02042 with a thickness of 4.44 µm) and a GaN NW ensemble (sample M9257 with a NW length of about 1.6 µm) allow for the comparison of the reflectance of both samples. From this comparison, the fraction of light coupled into both samples can be estimated. The major part of the penetrating light (yellow beam in Fig. 8.1) is transmitted through the layer or the NWs and is
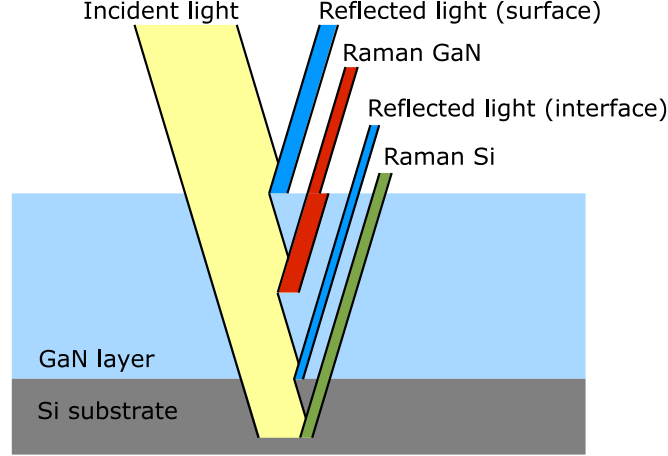
Figure 8.1.: Schematic illustration of the coupling of light into a GaN layer. A fraction of the incident light (yellow) is reflected (blue) at the surface. The remaining light penetrates the GaN layer (light blue) and is mostly transmitted to the substrate (gray), where it is absorbed or reflected at the interface (blue). A small fraction of the light is inelastically scattered in the GaN layer (red) and in the Si substrate (green) and detected as the Raman signal. Note that the experiments are performed at normal incidence.

absorbed by the Si substrate, while only a very small fraction of the light is scattered inelastically, causing the Raman signal (red and green beam in Fig. 8.1). In order to estimate the extraction efficiency of the GaN layer and the GaN NW ensemble, the respective intensities I_{GaN} of the GaN E_2^{H} phonon (red beam in Fig. 8.1) are scaled to the light intensity in the GaN, i.e., to the respective values of η_{in}. Finally, the scattering volume of the layer is about five times larger than that of the NW ensemble. Scaling the intensities of the GaN E_2^{H} phonons to the scattering volumes allows us to relate the extraction efficiency of the NW ensemble to that of the layer. The extraction of light out of a perfectly smooth layer is limited by total internal reflection at the surface of the layer. Using Eqs. 2.23 and 2.24, the absolute value of η_{out} of the GaN layer can be estimated. Table 8.1 summarizes the intensities of the reflected signal, the Raman signals, and the obtained results for η_{in} and η_{out} for the NW ensemble and the layer. We find that η_{in} is almost exactly the same for the layer and the NW ensemble. This finding is surprising, since due to different NW lengths the NW ensemble is expected to represent a rough surface for light of a wavelength larger than the NW diameter. Hence, it is expected that the light couples more efficiently into the NW ensemble than into a smooth layer. In order to understand this result, reflection at the substrate contributing to R has to be considered. If the NW ensemble is considered as a layer of an effective material, R and η_{in} can be analyzed analogously to the case of the GaN layer. The refractive index of this effective material is given by the refractive indices n_λ^{GaN} and $n_\lambda^{\mathrm{air}} \approx 1$ of GaN and air (or vacuum) scaled for their respective volumes. We indeed find that reflection at the surface of the layer is more than two times larger than that at the surface of the NW ensemble. However, considering in addition the reflection at the substrate interface, we obtain similar values for the total reflectance. In contrast, the extraction efficiency η_{out} differs by a factor of 2.5 to 3, depending on the wavelength. These factors actually underestimate the differences in η_{out}. Probing the GaN layer, both the polarized and depolarized configuration contribute to the intensity of the GaN E_2^{H} phonon as the light couples into the layer through its C-plane top facet. In contrast, the

Table 8.1.: Estimates of η_{in} and η_{out} for the GaN NW ensemble (sample M9257) and the GaN layer (sample NAE_02042). Quantities marked by an asterisk are calculated as explained in the text. The fractions $\eta_{out}^{NW}/\eta_{out}^{layer}$ and $\eta_{c}^{NW}/\eta_{c}^{layer}$ are scaled by the volume. In addition, the polarization dependence of the E_2^H phonon in the NWs is accounted for by a factor of 2.

λ_{Laser} (nm)	482.5		632.8	
n_λ^{GaN}	2.46		2.39	
	layer	NWs	layer	NWs
R	0.05*	0.06	0.30*	0.35
η_{in}	0.95*	0.94	0.70*	0.65
I_{GaN} (arb. units) scaled by η_{in}	780	390	240	160
$\eta_{out}^{NW}/\eta_{out}^{layer}$		5.0		6.4
η_{out}	0.04*	0.21	0.05*	0.29
$\eta_{c}^{NW}/\eta_{c}^{layer}$		4.9		5.9

light enters the NWs through their sidewalls. Hence, the E_2^H phonon is only allowed for light polarized perpendicular to the NWs [∗(y, ∗)∗-modes in Tab. 3.3]. Assuming that the light is unpolarized, only 50% of its intensity contributes to the intensity of the E_2^H phonon in the NW spectra. Furthermore, we used a microscope objective with a numerical aperture of 0.55, which accounts only for a part of the scattered light. The majority of light escaping the layer is collected. However, we expect that the NWs act as leaky waveguides, i.e., a significant fraction of the light is not emitted vertically, but under a certain angle. [27,174] Thus, only a fraction of the light leaving the NWs is recorded, and, as a consequence, the given value for the extraction efficiency of the NWs may be considered as a lower boundary. Nevertheless, the obtained values for the extraction efficiency of 0.21 to 0.29 agree well with reported values. [175]

8.2. Internal quantum efficiency of GaN nanowires

The radiative and nonradiative lifetimes τ_r and τ_{nr} determine the internal quantum efficiency η_{int} of a semiconductor (see Eq. 2.19). Therefore, TRPL measurements are commonly used to measure the lifetimes and consequently obtain η_{int}. The recombination dynamics of NW ensembles is typically characterized by a nonexponential decay. In Fig. 8.2, such a typical decay of the near-band-edge luminescence is depicted. This nonexponential decay is often explained to result from two different recombination or capture mechanisms, which, in general, are not further specified. [25,26,104] Therefore, the transients are often fitted by a biexponential decay function as shown by the red line in Fig. 8.2. In the following, a mechanism that possibly explains the observed recombination dynamics is discussed.
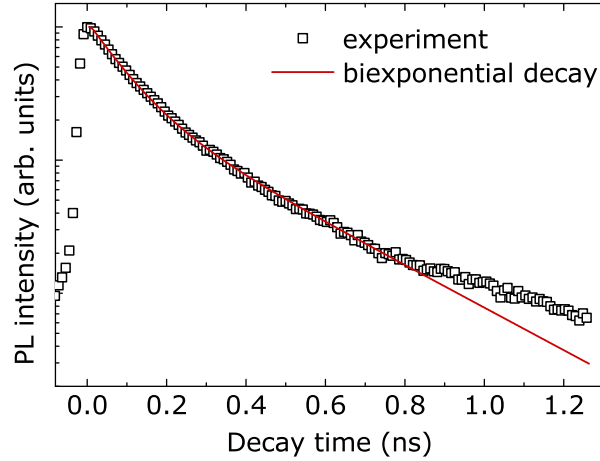
Figure 8.2.: Spectrally integrated transient of the near-band-edge luminescence of a GaN NW ensemble (sample 30887) at low temperatures. The data are fitted assuming a bi-exponential decay (red line). The transient has been recorded by T. Flissikowski.

Nonradiating NW feet

Performing CL experiments[a] at the cross section of GaN NW ensembles, we found that the lower part of the NWs (in the following referred to as NW "feet") is optically inactive, suggesting the presence of a nonradiative recombination mechanism in the lower part of the NWs. The vertical extent of this non-luminescent region is in general slightly larger than the NW diameter. When GaN NWs are grown directly on Si, an amorphous Si_xN_y layer forms, leading to the presence of dangling bonds at the NW/substrate interface. If a crystalline AlN buffer is deposited before NW nucleation, extended defects such as misfit dislocations bound to the interface are present in the lower part of a NW.[89] Both dangling bonds and extended defects represent nonradiative recombination centers, which may be the origin of the optically inactive NW feet.[b] Note that diffusion of excitons or carriers from the NW volume into the substrate can be excluded as the origin of these dark feet. CL measurements of dispersed NWs generally show that one end of the NWs is dark, just as in the case of as-grown NWs. If diffusion of excitons or carriers lead to the non-luminescent NW feet, dispersed NWs should emit along their entire length.

In order to analyze the influence of the non-luminescent NW feet on the recombination dynamics of GaN NWs, we performed cw-PL and TRPL experiments on three NW samples of different length. Except for the duration, the growth conditions were identical for these samples. NWs with a length of 200, 900, and 2 300 nm were synthesized (samples M8876, M8861, and M8891, respectively). In Fig. 8.3, SEM top views of the three samples are shown. Only a few coalesced NWs can be found in sample M8876 with the shortest NWs. With increasing NW length, the coalescence degree increases. Considering that NWs often grow with a slight tilt,[46] this finding is actually not surprising. In addition, although being less favorable, lateral growth contributes to the increase of the NW diameters. As a result, the sample with the longest NWs shows very strong coalescence.

---

[a]The CL measurements have been performed by U. Jahn.

[b]Extended defects can run either perpendicular to the substrate or at a certain angle. In the latter case, they eventually terminate at the NW surface. In the former case, however, the defect can travel along the entire NW and end at the top facet only if it is located at the center of the NW. More commonly, it bends after a certain distance toward the NW sidewalls and terminates there. Therefore, extended defects are expected to exist only in the NW foot.

(a) Top view of GaN NWs with a length of 200 nm (sample M8876).

(b) Top view of GaN NWs with a length of 900 nm (sample M8861).

(c) Top view of GaN NWs with a length of 2 300 nm (sample M8891).
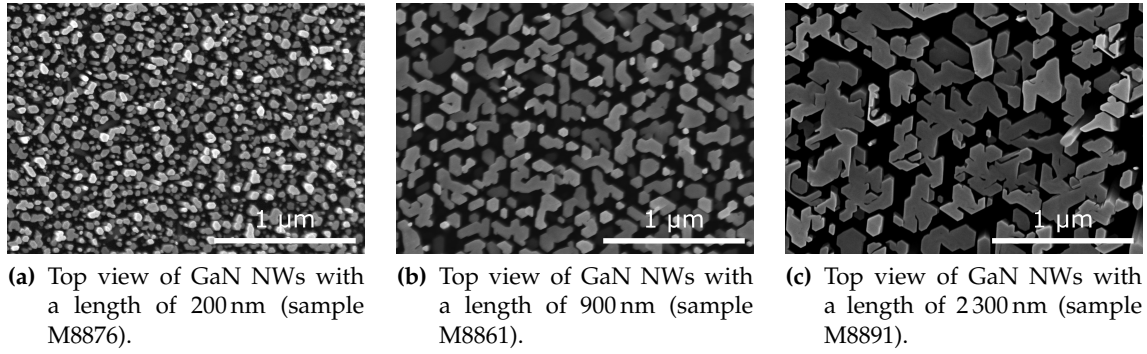
Figure 8.3.: SEM top views of three GaN NW samples with different NW lengths (samples M8876, M8861, and M8891). The images have been taken by A.-K. Bluhm.

Table 8.2.: Morphology parameters of the GaN NW samples M8861, M8876, and M8891.

Sample	M8876	M8861	M8891
Length (nm)	200	900	2 300
Average diameter (nm)	30	90	160
Coalescence	Marginal	Strong	Very strong

Table 8.2 gives an overview of the average lengths and diameters of the three samples.

The PL spectra of the three samples differ considerably. Figure 8.4(a) compares the normalized near-band-edge PL spectra of the three samples. All spectra are dominated by the (D^0,X) line at 3.471 eV. However, the relative intensity of defect-related transitions is the strongest for the shortest NWs (sample M8876, blue line). With increasing NW length, the (D^0,X) transition becomes dominant, and the total PL intensity increases. For the NWs with a length of 900 nm (sample M8861, red line), a minor contribution from SFs and from the (U,X) transition can be observed. In the PL of the longest NWs (sample M8891, green line), a pronounced (D^0,X) transition can be seen as well as a peak related to (A^0,X) recombination at 3.466 eV. Lower energy lines are only visible on a logarithmic scale. The pronounced influence of defect-related PL in the short NWs is reflected by the ratio of the near-band-edge luminescence and the defect luminescence. It considerably decreases with increasing NW length (see Tab. 8.3).

Figure 8.4(b) depicts the transients of samples M8876, M8861, and M8891. They are fitted with a biexponential decay function. Table 8.3 summarizes the decay times of the short and long components, τ_1 and τ_2, respectively. While there is no trend observable for τ_2, the short decay time τ_1 increases with the NW length. More importantly, the ratio of the two decay times τ_2/τ_1 clearly decreases. Using this ratio as a measure of the bowing of the transients, the significance of the fast recombination process can be assessed. The higher the ratio, the stronger its influence. The results listed in Tab. 8.3 thus show that with increasing NW length the significance of this fast recombination process decreases.

The results from the CL, cw-PL and TRPL experiments suggest that the NW/substrate interface acts as an efficient nonradiative sink for excitons, characterized by the interface

(a) Normalized PL spectra of NWs of different lengths. The spectra were recorded at 10 K. The spectra are shifted vertically for clarity.

(b) Low-temperature transients of the near-band-edge luminescence of NWs with different lengths. The solid lines represent biexponential fits to the transients. The measurements have been performed by T. Flissikowski.
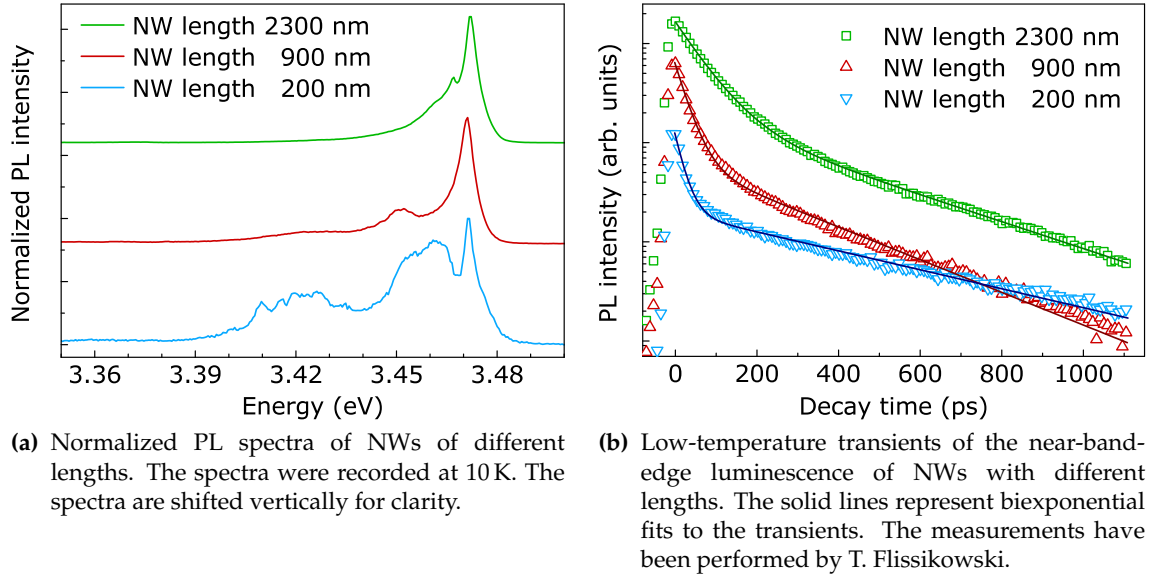
Figure 8.4.: Comparison of PL and TRPL of GaN NW samples M8876, M8861, and M8891 at 10 K.

Table 8.3.: PL results of NW samples M8876, M8861, and M8891. I_{NBE}/I_{def} represents the ratio of the integrated intensity of the near-band-edge luminescence and defect-related luminescence at lower energy. The lifetimes are obtained from biexponential fits to the data presented in Fig. 8.4(b). τ_1 and τ_2 represent the short and the long decay components. The ratio τ_2/τ_1 serves as a measure for the bowing of the transients. The transients have been recorded by T. Flissikowski.

Sample	M8876	M8861	M8891
Length (nm)	200	900	2 300
I_{NBE}/I_{def}	0.33	0.65	0.99
τ_1 (ps)	22	30	65
τ_2 (ps)	455	265	320
τ_2/τ_1	21	9	5

recombination velocity S_i. Taking into account the diffusivity D of excitons along the NW axis, the temporal evolution of the exciton density n in the NW may be expressed as:

$$\frac{\partial n}{\partial t} = G + D\frac{\partial^2 n}{\partial z^2} - \frac{n}{\tau_{eff}}, \tag{8.2}$$

where G denotes the exciton generation rate and τ_{eff} the effective lifetime including radiative and nonradiative recombination in the bulk and at the surface of the NW. To present nonradiative recombination at the NW/substrate interface, the boundary conditions are given by $\partial n(l)/\partial x = 0$ and $\partial n(0)/\partial x = -S_i n/D$, where l denotes the length of the NWs. The scheme on the right-hand side of Fig. 8.5 depicts the assumed initial exciton density profiles. Since light couples into the NWs through their sidewalls, they are excited over their entire length. The blue line depicts a constant initial exciton density and the red curve corresponds to a sinusoidal exciton distribution[149] as predicted by the solution of Maxwell's equation for a periodic array of GaN NWs standing on a Si wafer (cf. Sec. 5.4). The green curve depicts the initial exciton density as expected if the
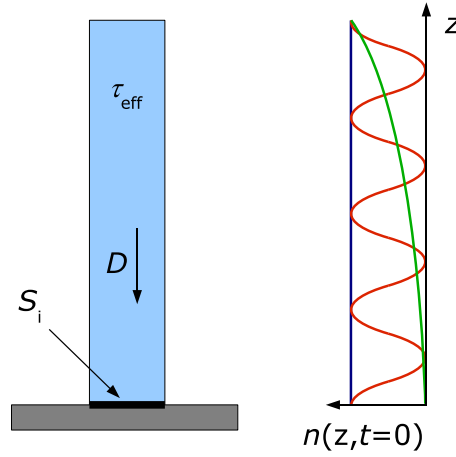
Figure 8.5.: Schematic illustration of the recombination model described by Eq. 8.2. Excitons may diffuse towards the NW foot (described by the diffusion constant D), where they predominantly recombine nonradiatively due to interface recombination represented by S_i. Nonradiative surface recombination is implicitly included in τ_{eff}. On the right-hand side, different initial exciton densities $n(z, t = 0)$ along the NW are illustrated.

NWs were excited through the top facets only. The numerical solution of Eq. 8.2 yields a nearly single-exponential decay, regardless of the chosen parameters τ_{eff}, D, and S_i. As long as the recombination at the NW foot and in the upper NW volume is coupled via the diffusion constant D ($D > 0$), none of these initial profiles results in a biexponential decay behavior.

Alternative ansatz for the recombination dynamics

Only a few models have been proposed to describe the nonexponential recombination dynamics in NW ensembles. Corfdir *et al.*[119] have developed a core-shell model for GaN NWs. In this model, the lifetimes and the relative intensities of (D^0,X) and TES transitions depend on the position of the respective donor within the NW. Another model by Wischmeier *et al.*[115] describes the nonexponential recombination in ZnO NWs. This model is based on the recombination of differently localized surface excitons. Both models are rather complex and involve material specific parameters, i.e., they may not be easily transfered to other material systems. Commonly, the nonexponential recombination dynamics found for NW ensembles is described phenomenologically by a biexponential decay (cf., for instance, Refs. 25, 104, and 26). However, we generally observe that the experimental data systematically deviate from a biexponential decay behavior at long decay times (see, for instance, Fig. 8.2). The larger the dynamic range in a time-resolved PL measurement, the more pronounced are these discrepancies.

These observations in conjunction with the perpetual difficulties to formulate a simple model for the recombination dynamics of NW ensembles raise the question whether a fundamentally different ansatz has to be chosen in order to explain the commonly observed nonexponential decay behavior.

In the previous chapters, several phenomena have been discussed that affect the recombination dynamics of GaN NWs. First, the recombination processes in GaN NWs differ from that in GaN layers. This difference is probably caused by nonradiative sur-

(a) Histogram of the diameter distribution of a NW ensemble. The diameter distribution is obtained from a SEM top view image as shown in Fig. 3.2(c) using the programm IM-AGEJ.[176]

(b) Histogram of the distribution of effective recombination rates. The recombination rates are calculated using Eq. 8.3 with $\gamma_b = 1\,\text{ns}^{-1}$.
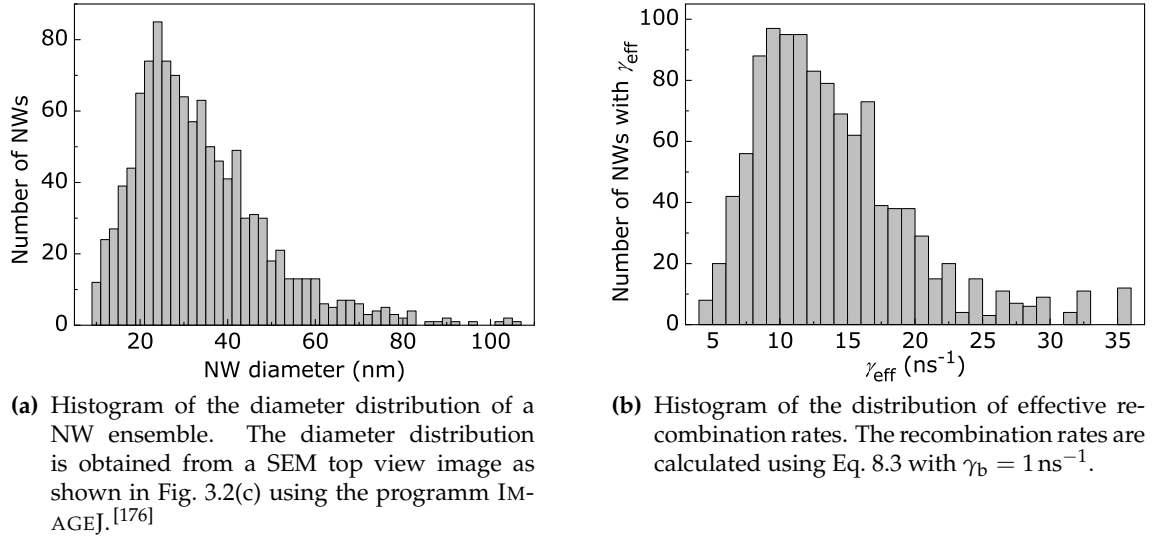
Figure 8.6.: Distribution of the NW diameter and the effective recombination rate γ_{eff} of sample 30887.

face recombination in the NWs (cf. Sec. 5.3). Second, the presence of donors and their location within a NW determines the optical properties of a NW. As shown in Sec. 6.2, these properties fluctuate strongly from NW to NW. Third, the influence of electric fields on the recombination dynamics is investigated in Sec. 7.2. In the following, the effect of these phenomena on the recombination dynamics will be discussed.

Nonradiative surface recombination

Schlager *et al.*[104] have shown that the nonradiative surface recombination significantly affects the PL decay time in GaN NWs. They determined the room-temperature nonradiative surface recombination velocity S to $9 \times 10^3\,\text{cm/s}$ by measuring the diameter dependence of the effective decay time of single GaN NWs.[104] Note that this low value of S indicates that nonradiative surface recombination plays only a minor role in the recombination processes of bulk GaN. For NWs, however, the diameter dependence of the lifetime demonstrates that the surface represents an efficient recombination channel. The effective recombination rate can thus be written as:

$$\gamma_{\text{eff}} = \gamma_b + \frac{4S}{d}, \tag{8.3}$$

where γ_b denotes the bulk recombination rate and the second term describes nonradiative recombination at the surface. For large diameters d, γ_{eff} saturates at the bulk recombination rate. Its inverse, the bulk lifetime τ_b for low temperatures, has been determined to be on the order of 1 ns for low temperatures.[138]

SEM top views of the GaN NW ensembles [cf. Fig. 3.2(c)] reveal a large diameter dispersion within such an ensemble. Figure 8.6a show a histogram of the NW diameters obtained from SEM top views of samples 30887. The respective dispersion of γ_{eff} can be calculated with Eq. 8.3 using the above values for S and $\gamma_b = \tau_b^{-1}$. The resulting rate distribution is relatively broad as depicted in Fig. 8.6b. Thus, due to the diameter dependence of γ_{eff}, each NW exhibits its specific lifetime, and probing a NW ensemble

will in fact display the superposition of contributions from different NWs. Even if individual NWs exhibit a single-exponential decay, the superposition of a large number of exponential functions with varying decay constants is thus nonexponential.

Position of donors

At low temperatures, the PL of the GaN NWs is generally governed by the (D^0,X) emission. The transition energy of a (D^0,X) is determined by the distance of the related donor to the NW surface (cf. Sec. 6.1). If this distance is larger than $1.4\,a_B$, the donor is bulk-like, and its recombination energy corresponds to the one expected for unstrained GaN. If the donor resides closer to the surface, the recombination energy continuously increases because the exciton binding energy decreases. As a consequence, the exciton is less localized, and thus the recombination rate is increased.[62] The relation between exciton binding energy and recombination rate is given by:[177]

$$\gamma_{\text{eff}} \propto E_X^{-3/2}. \tag{8.4}$$

In Sec. 6.2 the influence of the position of a single donor within the NW for the PL spectrum of this NW has been investigated. Equation 8.4 implies that not only the transition energy of a donor-bound exciton but also its recombination rate and accordingly its lifetime are influenced by a nearby surface. Thus, the lifetime of donor-bound excitons can vary *even within* a single NW. For a single, unintentionally doped NW, a single-exponential decay may be observed, since the number of donors per NW is very low (cf. Sec. 6.2). In contrast, the recombination dynamics of a highly doped single NW can be expected to be nonexponential as long as the diameter of the NW is sufficiently small to find a significant amount of surface donors. Probing NW ensembles, however, will inevitably include surface donors as well as bulk-like donors. Consequently, the dispersion of lifetimes will contribute to the nonexponential decay characteristics.

Electric fields

The pinning of the Fermi level at the NW sidewalls gives rise to the presence of electric fields in the NW volume (see Chap. 7). In unintentionally doped NWs ("thin" NWs as defined in Sec. 7.2), these fields are present in the entire NW volume, since the conduction and valence band profiles exhibit a bowing across the entire NW diameter. In highly doped NWs ("thick NWs"), however, a field-free conductive channel can be found in the center of the NWs.[75]

The recombination rate of excitons experiencing electric fields is considerably decreased even at low field strengths.[58] Essentially, the overlap of the electron and hole wave functions is reduced since they are pulled apart due to the electric field. A peak shift, however, is not observed as pointed out in Sec. 7.2.

The strength of the electric field at a certain point in the NW is determined by three factors:

(i) The donor concentration determines the band bending of the conduction and valence bands. Within a NW ensemble, the donor concentration is assumed to be constant.

(ii) The influence of the NW radius R on the field strength at different locations within a NW is depicted in Fig. 8.7. The maximum of the electric field is found at the NW
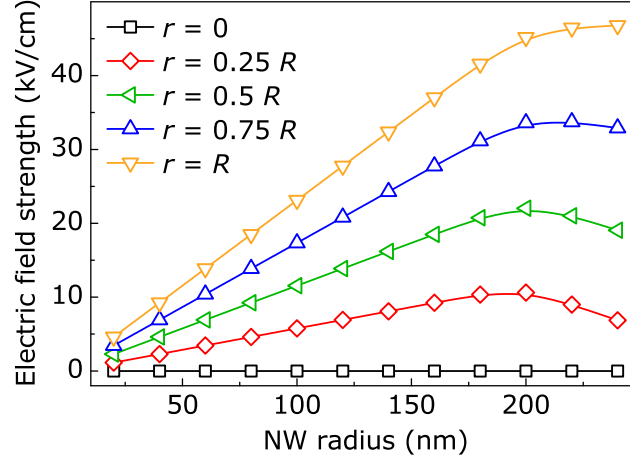
Figure 8.7.: Diameter dependence of the electric field strength in GaN NWs. The Fermi level pinning is set to 0.6 eV, and a donor concentration of 5×10^{16} cm^{-3} is assumed. The five data sets depict the field strength at different distances from the center of the NW in terms of its radius R. The results are based on calculations performed with the program 1DPOISSON

surface. Its strength increases with increasing radius and saturates when R exceeds a critical value of about around 200 nm. [75]

(iii) For donor-bound excitons, the distance of the related donor to the NW surface determines the field strength.

Accounting for all three effects, the recombination rate within a NW ensemble will inevitably vary from NW to NW, depending on their diameter and in addition, within a NW from donor to donor, depending on their location.

Gaussian distribution of the recombination rates

The lifetime that a specific NW exhibits is affected by nonradiative surface recombination, the location of incorporated donors, and the presence of electric fields within the NW. The consequent variations in lifetime between individual NWs have to be taken into account when the recombination dynamics of a NW ensemble is considered. For a simple phenomenological description of these phenomena, we assume first that a single (D^0,X) exhibits a mono-exponential decay with an effective recombination rate γ_{eff}. Secondly, we assume that the variations in the recombination rates of the individual NWs in a NW ensemble follow a Gaussian distribution Γ:

$$\Gamma = \frac{1}{\sqrt{2\pi}\sigma} \exp\left(-\frac{(\gamma_{\text{eff}} - \gamma_0)^2}{2\sigma^2}\right), \tag{8.5}$$

where σ and γ_0 are the standard deviation and the maximum of the Gaussian distribution, respectively. A convolution of the mono-exponential decay of single NWs and Eq. 8.5 describes the PL transient of a NW ensemble:

$$I_{\text{PL}}(t) \propto \int_{\gamma_{\text{b}}}^{\infty} d\gamma_{\text{eff}} \exp\left(-\frac{(\gamma_{\text{eff}} - \gamma_0)^2}{2\sigma^2} - \gamma_{\text{eff}}t\right). \tag{8.6}$$
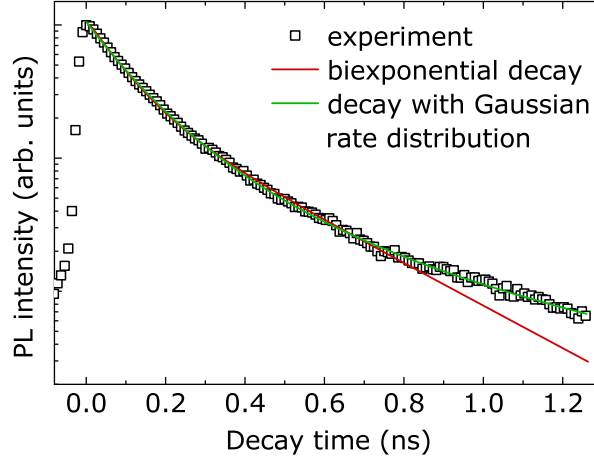
Figure 8.8.: Transients of sample 30887 fitted with a Gaussian distribution of recombination rates (green line). The red line shows a biexponential fit. The transient has been recorded by T. Flissikowski and the simulation has been performed by O. Brandt, V. Kaganer, and K. Sabelfeld.

At the lower end, the rate distribution is cut off at the bulk recombination rate γ_b. Figure 8.8 shows the very same experimental data depicted in Fig. 8.2. The green line in Fig. 8.8 represents a simulation of the excitonic decay according to Eq. 8.6. Over the entire dynamic range the experiment is well described by a Gaussian distribution Γ centering at $\gamma_0 = 9\,\mathrm{ns}^{-1}$. This value is equivalent to an effective lifetime of 110 ps, i.e., the recombination is governed by nonradiative processes. The width of Γ and the cut-off rate γ_b amount to $9.2\,\mathrm{ns}^{-1}$ and $0.6\,\mathrm{ns}^{-1}$, respectively. γ_b corresponds to a radiative bulk lifetime of about 1.7 ns, which is slightly longer than the longest lifetimes reported.[138] The internal quantum efficiency of these NWs can thus be calculated with Eq. 2.19 to be about 6%.

8.3. Conclusion

The determination of the internal and external quantum efficiencies η_{int} and η_{ext} as figures of merit for the optical quality of NW ensembles is not as straight-forward as in the case of layers. The comparison of the reflectance and of the intensity of the Raman signal of a NW ensemble with that of a smooth layer yields quantitative estimates of η_{int} and η_{ext}. We found that the combined efficiency η_c^{NW} of the NW ensemble is about five to six times higher than that of the layer. This difference is mainly caused by a considerably increased extraction efficiency. The absolute value of 6% of the internal quantum efficiency η_{int} is unexpectedly low, mainly due to the strong influence of nonradiative recombination at the NW surface.

For the determination of the internal efficiency η_{int}, a physically motivated model is proposed based on the findings presented in the previous chapters. The key property of this model is the presence of a distribution of the recombination rate. Although the applied Gaussian rate distribution describes the system only phenomenologically, it yields plausible results. Nevertheless, a physically motivated rate distribution is yet to be found. To this end, the analysis of top-view SEM images of NW ensembles is required. Such an analysis may provide a distribution of NW diameters, perimeters, and cross sections. Knowing these morphological parameters, the influence of nonradiative surface recombination and electric fields on the recombination for each of the considered NWs can be quantified, thus eventually yielding a realistic rate distribution.

9. The (U,X) band

The PL spectra of all investigated GaN NW samples studied in this work contain a transition around 3.45 eV, here referred to as the (U,X) transition. Although this feature is commonly observed,[5,119,130,132] its origin remains controversial. Considering bulk GaN, the TES transition of the (D^0,X) is found at this energy, its intensity, however, is generally more than one order of magnitude less than that of the (D^0,X) transition.[135] In the present chapter, the experimental findings of this thesis regarding the (U,X) band are discussed and compared to the potential origins proposed in the literature.

9.1. The (U,X) peak in the literature

E. Calleja *et al.*[5] investigated the optical properties of GaN NWs with different morphologies by cw-PL and TRPL spectroscopy. From the results of the excitation density and temperature dependence of the (U,X) band and from its recombination dynamics, they concluded an excitonic nature of this transition. Furtmayr *et al.*[132] observed a different thermal quenching behavior for the (D^0,X) line than for the (U,X) band. Here, it was speculated that this band originates from excitonic recombination related to Ga vacancies, resulting from the globally N-rich growth conditions.[178,179] With increasing concentration of Mg acceptors, the surface-to-volume ratio was found to decrease as did the relative intensity of the (U,X) transition. Therefore, the authors suggested that the Ga vacancies are predominantly formed at the NW sidewalls. Robins *et al.*[23] studied PL and CL experiments of GaN NWs. Due to the different evolutions of the peak intensities of the (D^0,X) and (U,X) transitions with increasing electron irradiation, they tentatively ascribed the (U,X) band to the presence of inversion domain boundaries.

Corfdir *et al.*[119] attributed the (U,X) band to the the TES transition of the (D^0,X). The high relative intensity of the TES is proposed to be specific to NWs and is explained by a core-shell model. The authors suggest that the (D^0,X) line originates from bulk-like donors in the core of the NWs, whereas the TES line predominantly stems from excitons bound to donors located near the surface. Close to the surface, the envelope function of the (D^0,X) complex is distorted[180] due to the large potential outside of the NW (cf. Ref. 159), and therefore, the TES transition probability is argued to increase.[181] A second peak is observed by the same authors at 3.456 eV, which they discuss in terms of free excitons that are inelastically scattered at unoccupied donors.[180,181] Similar to the TES of the (D^0,X), the donor is left behind in an excited state after the recombination process.

9.2. Observations in the present work

To a certain extent, our results regarding the (U,X) band agree with the model proposed by Corfdir *et al.*[119] First, the (U,X) transition is found in the luminescence of all investigated NW ensembles, regardless of the MBE system they were grown in. In contrast, layers synthesized in the same reactors do not exhibit this peak. Therefore, it is most likely not related to the incorporation of an impurity.

(a) Temperature-dependent PL spectra of sample 30928. The gray, red and violet lines indicate the position of SF luminescence, the (U,X), and the (U,X)' transition, respectively. The orange and blue lines denote the (D⁰,X) and FX transitions, respectively.

(b) Temperature dependence of the peak energies of sample 30928. The energy of the SF luminescence is not shown here.
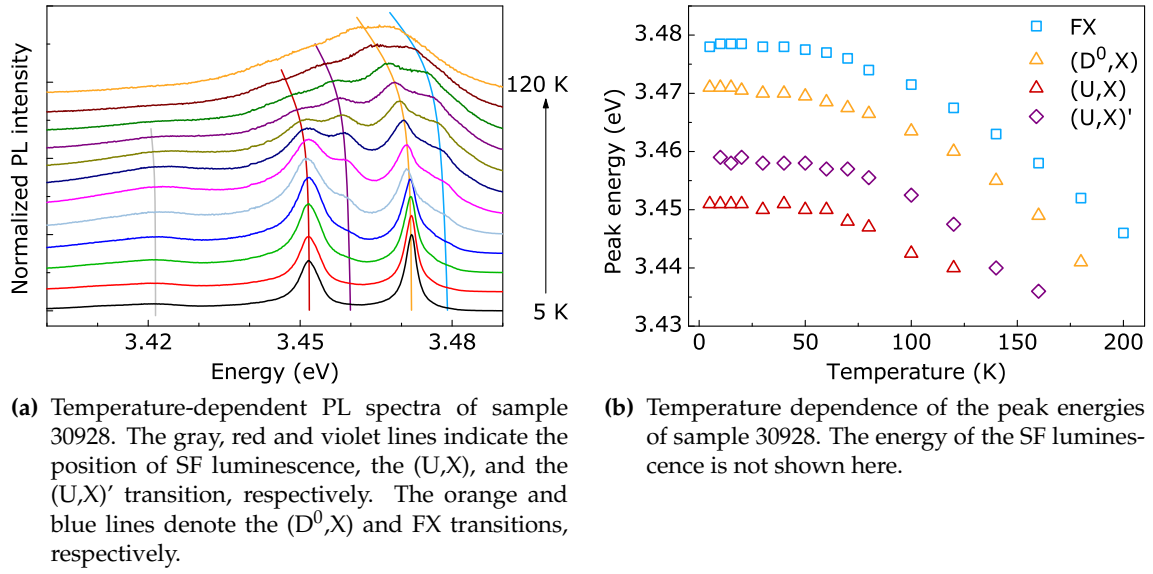
Figure 9.1.: Temperature dependence of the (U,X) transition.

Second, in ensemble measurements, commonly one broad peak or a peak doublet with an energetic separation of 6 to 8 meV is observed. Experiments with single NWs, however, indicate that this band is actually a convolution of several sharp peaks.[156] This finding is consistent with the model of Corfdir *et al.*[119] as numerous TES transitions around 3.45 eV have been reported.[181] This variety of TES lines is due to O and Si donors that in addition may exist in differently excited states.

Third, the temperature dependence of the (U,X) line resembles that of the (D⁰,X) line. In addition, a second peak is observed at 3.458 eV, similar to the peak doublet reported by several groups.[5,132] The evolution of the PL intensity of sample 30928 with increasing temperature is depicted in Fig. 9.1(a), and Fig. 9.1(b) shows the evolution of the peak energies with temperature. At low temperatures, the (D⁰,X) line is observed at 3.471 eV (vertical orange line), the (U,X) transition at 3.45 eV (red line), and a minor peak at 3.42 eV related to SFs. At a temperature of 15 to 20 K, the FX line increases on the high-energy side of the (D⁰,X) line at 3.479 eV. Simultaneously, an additional peak [labeled as (U,X)'] of unknown origin emerges at 3.458 eV. With increasing temperature, the FX and the (U,X)' gain over the (D⁰,X) and the (U,X), respectively. In the model of Corfdir *et al.*,[119] the (U,X)' line represents the recombination of free excitons scattered inelastically at neutral donors.[180,181] The similarities between the energy separation as well as the temperature dependencies of the (U,X) and (U,X)' transitions, on the one hand, and those of the (D⁰,X) and FX transitions, on the other hand, are striking and further substantiate this model.

Nonetheless, a number of experiments performed in this thesis show results, not easily explained in the framework of this model. The desorption of oxygen from the surface of GaN NWs has been discussed in Sec. 7.2. Upon UV illumination, the PL intensity increases due to a reduction of electric fields within the NWs. In this context, the comparison of the increase of the (U,X) and the (D⁰,X) intensity is of particular interest, as the latter one is much more pronounced than the former one [cf. Fig. 7.10(b) and Tab. 7.1]. This result suggests that the origin of the (U,X) luminescence is less affected by the decreasing electric fields than that of the (D⁰,X) transition. The maximum field strength is found at the NW surface (cf. Fig 7.1), i.e., the region the (U,X) line is suggested to originate from. Hence, the decrease of the electric field is much more pronounced in this region than in the NW core. Consequently, the intensity increase of the (U,X) line should be

(a) Normalized PL spectra of sample M8863 taken at different excitation powers.

(b) Relative intensities of the SF, (U,X), and (D^0,X) transitions.
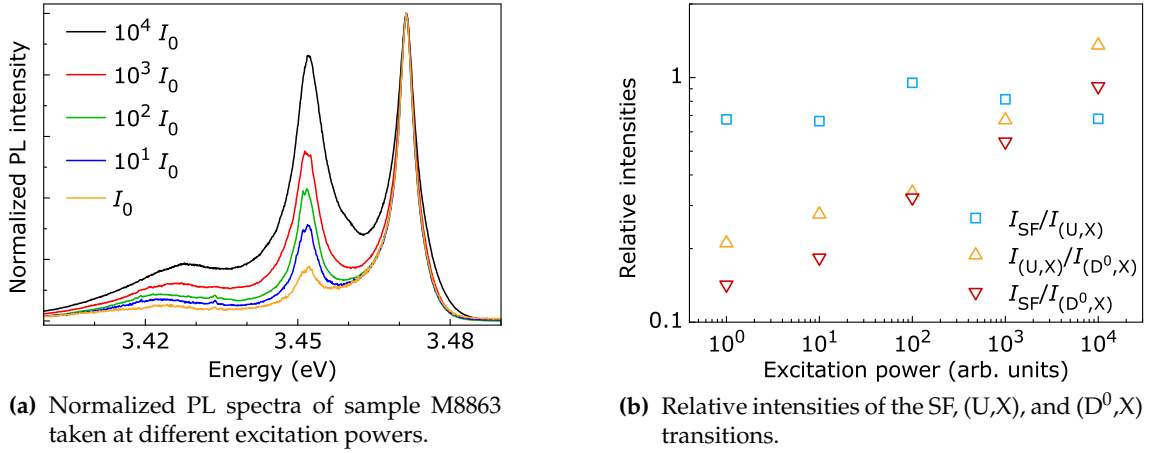
Figure 9.2.: Excitation power dependence of the (U,X) transition.

more pronounced than that of the (D^0,X) transition, which contradicts the experimental findings.

Figure 6.9 depicts the PL spectra of samples 30927 grown on Si(001) and sample 30887 grown on Si(111). Besides the different substrate orientations, the growth conditions were the same for both samples. Nevertheless, the relative intensities of the (U,X) lines differ considerable. While for sample 3088, a prominent peak is found at 3.45 eV, sample 30927 exhibits only a minor transition in this region. This difference could be explained, if the NW diameter of sample 30887 would be much larger than that of sample 30927.[180] However, no significant difference is found studying SEM images of both samples.

Finally, excitation-density-dependent PL spectra of sample M8863 are shown in Fig. 9.2(a). They are normalized to the (D^0,X) transition. The relative intensity of the (U,X) band compared to that of the (D^0,X) transition is found to increase with increasing excitation power. This behavior rather points to a planar defect or to abundant point defects as the origin for the (U,X) band.[156] Both is not consistent with the model of Corfdir *et al.*[119] In Fig. 9.2(b), the relative intensities of the three major luminescence bands are plotted versus the excitation power. Of particular interest is the relation between the SF luminescence and the (U,X) band. The ratio of their intensities remains constant regardless of the excitation power, indicating that both have a common origin. Similar observations have been reported by Robins *et al.*[23] This finding suggests that the (U,X) band is related to the coalescence of adjacent NWs, since SFs are found to form several 100 nm above the contact point of coalesced NWs.[46] At this contact point, boundary dislocations are built in to accommodate the relative tilt of the coalesced NWs. The (U,X) band may therefore be related to the presence of radiative defects induced by the coalescence of NWs. However, this mechanism may not explain all experimental results. For instance, the relative intensity of the (U,X) band increases with decreasing NW diameter and thus with decreasing coalescence.[180]

9.3. Conclusion

In conclusion, the experiments shown in this thesis partly confirm and partly contradict the TES-model proposed by Corfdir *et al.*[119] Based on its excitation density dependence, the (U,X) band may also be related to the coalescence of NWs, a finding that in turn disagrees with some reported results. In either case, additional experiments are necessary in order to identify the nature of this transition.

10. Conclusions and Outlook

10.1. Summary and conclusions

NWs have received increased attention in the last decade as they offer the possibility to grow unstrained semiconductor material of high crystalline quality independent of the used substrate. Thus, they are believed to allow for the integration of III-V and II-VI semiconductors with superior optical and electrical properties even on substrates such as Si that exhibit a large mismatch in the lattice constant and the thermal expansion coefficient. These attractive properties rely on a few simple assumptions, e.g., the effective release of strain due to the small NW/substrate interface and the efficient passivation of extended defects due to the nearby surface. These effects are usually considered to occur regardless of the substrate or the applied growth mechanism.

This thesis presents a detailed study of the optical properties of semiconductor NWs including GaN, GaAs, and ZnO NWs. It is based on PL spectroscopy and focuses on the investigation of single dispersed and single free-standing GaN NWs as well as GaN NW ensembles.

One aim of this thesis was to examine some of the above expectations. For this reason, general NW properties, which are often taken for granted in the NW community, have been investigated:

- The influence of the substrate on the optical properties of NWs has been studied exemplary for ZnO NWs grown on Si, Al_2O_3, and ZnO substrates. The virtually identical optical properties of the three samples imply that the synthesis of NWs, in contrast to the deposition of layers, is indeed free from constraints given by the substrate.

- PL, Raman, and XRD experiments of GaN NWs show that the NWs are, within the experimental error, free of homogeneous strain.

- Light couples to NWs of sub-wavelength dimensions predominantly through their sidewalls rather than through their top facets as Raman spectroscopy of a GaN NW ensemble reveals.

- Temperature-dependent PL measurements of Au-assisted GaAs/(Al,Ga)As core-shell NWs have shown the limited suitability of catalyst-assisted NWs for optical applications as a thermally activated, nonradiative recombination channel is found, potentially due to the incorporation of catalyst atoms.

NWs have been predicted to serve as versatile building blocks of future nanometer-scaled devices.[19,20] The above results show that, to a large extent, NWs meet the high expectations inherent to this vision.

Within the framework of this thesis, a thorough characterization of the optical properties of GaN NWs has been performed:

- The temperature and excitation power dependencies of the PL intensities of GaN NW ensembles and heteroepitaxially grown GaN layers indicate that different non-radiative recombination mechanisms are present in the NWs and in the layer. As the origin, the large surface-to-volume ratio of the NWs is tentatively discussed.

- The influence of the Fermi level pinning on the PL intensity of GaN NWs has been investigated by studying the photoinduced desorption of oxygen from the surface of these NWs. The results show that in unintentionally doped NWs, the entire NW volume experiences electric fields.

- The reflectance and the Raman signal of a thick GaN layer and a GaN NW ensemble, both grown on Si, has been used to estimate the efficiency of coupling of light to the NWs. While the coupling of light into the NWs and into the layer is almost equally efficient, the extraction efficiency of NWs is found to be higher by a factor of five to six.

- Contradictory results regarding the origin of the (U,X) peak have been obtained. Several findings support the model proposed by Corfdir *et al.*,[119] but some observations cannot be easily explained in the framework of this model.

The central message of these findings is that the optical properties of NWs in general are determined to a large part by their surface. In contrast to layers, the large surface-to-volume ratio is crucial for NWs, as it permits an efficient strain release, passivation of extended defects, and a decoupling of the crystal quality from the used substrate. Effects such as surface depletion, electric fields, and nonradiative surface recombination may severely affect the functionality of NW devices, but they may also be exploited, e.g., in sensor applications. The passivation of the surface is crucial for the performance of NWs in light-emitting devices.

Several experiments conducted in the framework of this thesis revealed another important aspect concerning single NWs. To understand certain optical characteristics of NW ensembles, the properties of individual NWs have to be considered. These are found to vary strongly from NW to NW:

- Sharp excitonic transitions in the PL of single NWs with an energy between the (D^0,X) and the FX transition have been identified as radiative transitions of excitons bound to surface donors. The position-dependent energy dispersion of these $(D^0,X)_s$ transition energy is found to cause a broadening of the (D^0,X) peaks in the ensemble spectra.

- The presence and the location of donors within individual NWs determine their emission. Inevitable statistical fluctuations of the donor incorporation thus results in strong variations of the optical properties of individual NWs.

- Electric fields are present in the entire NW volume. Their influence on the recombination of a specific exciton (either free or bound) is determined by the NW radius and the location of this exciton within the NW.

- The desorption of oxygen from the NW surface has been studied. The temporal evolution of the desorption process can be only understood if readsorption of oxygen molecules on adjacent NWs is allowed.

- A model is introduced that describes the nonexponential recombination dynamics commonly observed for NW ensembles. This model is physically motivated by one of the central results of this thesis: each NW potentially exhibits its own individual recombination behavior due to nonradiative surface recombination, the presence and location of donors within the NW, and the presence of electric fields. The result is a dispersion of recombination rates. Preliminary fits using a Gaussian rate distribution describe the recombination dynamics of GaN NW ensembles satisfactorily and indicate that nonradiative recombination processes prevail.

These findings are of particular importance for devices based on single NWs. First, conclusions from ensemble properties to the characteristics of single NWs are debatable. Second, the statistical fluctuations impede the reproducibility of devices based on single NWs. Third, the presence of electric fields has serious implications for the usually undoped active regions of NW LEDs, as these affect the internal quantum efficiency.

10.2. Outlook

The experiments discussed in this thesis showed that the large surface-to-volume ratio of NWs determines to a large extent their optical properties. Some of the surface-related effects have been examined, but further investigations are necessary for a full understanding of the influence of the surface.

In order to optimize the optical properties of GaN NWs, a precise control of the NW surface is required (cf. Chap. 7). This control may be achieved by a passivation of the surface that allows for an adjustment of the Fermi level pinning. Coating the NWs, e.g., with AlN or (Al,Ga)N shells, may prevent a pinning of the Fermi level, and thus, the related electric fields may be diminished. In addition, a shell made of a large-bandgap material would act as a barrier for carriers, and nonradiative recombination at the surface would be reduced.

The sensitivity of the Fermi level pinning may also be exploited for sensing applications. For instance, the Fermi level pinning in GaN NWs coated with Pt is readily increased in the presence of H_2 molecules, but the effects of O_2 are marginal.[182] As a consequence, the conductance of these NWs strongly depends on the ambient gas, and, due to their large surface-to-volume ratio, NWs may serve as efficient gas sensors. In either case, a precise control of the Fermi level pinning is necessary, and extensive studies with different shell or coating materials are required.

Another central result of this work is that each NW exhibits its own individual recombination behavior, which is indirectly caused by the large diameter dispersion found for the self-assisted GaN NWs. Both the influence of nonradiative surface recombination and the strength of the electric fields is to large extent determined by the NW diameter. Therefore, the control of the diameter dispersion is an important step toward the control of the optical properties of single NWs.

Selective-area growth,[183] i.e., a combination of the top-down and the bottom-up approach, may be an effective tool for the synthesis of arrays of GaN NWs with constant diameters. Consequently, some of the many parameters affecting the recombination rates of individual NWs (cf. Chap. 8) may be monitored, namely the nonradiative surface recombination and the strength of the electric fields. TRPL spectroscopy of selectively grown GaN NWs may thus lead to a better understanding of the recombination, and eventually,

the internal quantum efficiency of such NWs may be determined reliably. In addition, TRPL spectroscopy of single NWs may also be helpful to develop a better understanding of the recombination processes in single GaN NWs.

Finally, further investigations are required in order to identify the origin of the 3.45 eV band. For instance, combined PL and transmission electron microscopy experiments of single NWs and NW clusters may clarify, whether this band is related to extended defects, e.g., due to coalescence. In order to verify the model proposed by Corfdir *et al.*,[119] the distortion of the wave function of excitonic complexes near the NW surface should be analyzed theoretically. The results may give insight into the recombination probabilities of different recombination channels [TES vs. direct radiative recombination of the (D^0,X)], which can then be compared to the results of PL experiments of GaN NWs with different diameters.

A. Sample list

Table A.1.: Overview of the NW samples investigated in this work. The GaAs and (Al,Ga)As/GaAs NWs were grown at MBE 6. GaN NWs having sample numbers starting with M8 and M9 were grown at MBE 8 and 9, respectively. MBEs 6, 8, and 9 are located at the PAUL-DRUDE-INSTITUTE in Berlin. The remaining GaN NW samples have been grown at QIMONDA and INFINEON in Munich. The ZnO NWs are grown in MOCVD reactor at the UNIVERSITY OF CALIFORNIA in Santa Barbara.

Sample	Growth temperature (°C)	Substrate	Catalyst	V/III / VI/II ratio	NW length (nm)	NW diameter (nm)	NW density (μm^{-2})
GaAs							
M6835	500	Si(111)	Au	2	2000	50	10
AlGaAs/GaAs							
M6868	500	Si(111)	Au	2	2500	40	8
M6939	500	Si(111)	Au	2	5000	60	5
M6967	580	Si(111)	Ga	1	9000	150	1
GaN							
30887	780	Si(111)	–	4.7	400	40	100
30927	780	Si(001)	–	4.7	420	45	100
30928	780	Si(111)	–	4.7	400	60	140
M8849	800	Si(111)	–	5.1	1200	–	–
M8857	800	Si(111)	–	6.2	1000	120	100
M8861	780	Si(111)	–	6.2	900	45	40
M8863	780	Si(111)	–	6.2	900	120	80
M8876	780	Si(111)	–	6.2	200	20	360
M8891	780	Si(111)	–	6.2	2300	80	20
M9246	720	Si(111)	–	6	840	400	6
M9247	780	Si(111)	–	6	1100	140	35
M9250	800	Si(111)	–	3	1450	150	25
M9257	820	Si(111)	–	1.2	1600	130	38
ZnO							
2	615	Si(111)	–	290	650	40	50
3	550	$Al_2O_3(0001)$	–	39800	280	60	50
5	550	ZnO(0001)	–	660	700	80	10

B. Recombination processes

In the following, the recombination processes in semiconductors are discussed starting with rate equation systems that describe these recombination processes. These rate equation systems are analyzed aiming for analytical expressions for the radiative and non-radiative recombination rates. The limiting cases of low and high excitation conditions are considered. Excitonic and free-carrier recombination processes are considered. The books of Pankove,[38] Ahrenkiel,[184] and Sze[185] are used as references.

B.1. Excitonic recombination

Considering excitonic recombination in an n-type semiconductor with donor density $N_D = N_D^0 + N_D^+$,[a] the free exciton density n_F and the density of available donors under steady-state conditions can be described by a rate equation system:

$$\frac{dn_F}{dt} = G - \gamma_F n_F - b_c n_F N_D^0 + W_D N_D^+ = 0 \,, \tag{B.1a}$$

$$\frac{dN_D^0}{dt} = -\gamma_D N_D^+ + b_c n_F N_D^0 - W_D N_D^+ = 0 \,. \tag{B.1b}$$

G and γ_F denote the generation and recombination rates, respectively, of free excitons. The recombination rate comprises nonradiative and radiative recombination rates $\gamma_{F,nr}$ and $\gamma_{F,r}$, respectively:

$$\gamma_F = \gamma_{F,nr} + \gamma_{F,r} \,. \tag{B.2}$$

A rather complex steady-state solution for the coupled rate equation system (Eqs. B.1) can be obtained assuming $\gamma_D N_D^+ \ll b_c n_F N_D^0 \approx W_D N_D^+$. The transient case can only be solved numerically.

However, under low excitation, such that the donor density N_D is large compared to n_F, Eqs. B.1 can be approximated by:

$$\frac{dn_F}{dt} = G - \gamma_F n_F - \gamma_c n_F + W_D n_D = 0 \,, \tag{B.3a}$$

$$\frac{dn_D}{dt} = -\gamma_D n_D + \gamma_c n_F - W_D n_D = 0 \,, \tag{B.3b}$$

considering the density of donor-bound excitons n_D instead of the density of unoccupied donors. Note that n_D equals N_D^+. γ_c describes the capture rate at which free excitons are localized at donors. This set of rate equations can be solved analytically for both, the steady-state and the transient case. The steady-state solution is obtained from the

---

[a] N_D^+ denotes the density of donors to which an exciton is bound and N_D^0 is the density of unoccupied donors.

summation of Eqs. B.3a and B.3b:

$$n_F = \frac{G(\gamma_D + W_D)}{\gamma_c\gamma_D + \gamma_F\gamma_D + \gamma_F W_D} , \tag{B.4a}$$

$$n_D = \frac{G\gamma_c}{\gamma_c\gamma_D + \gamma_F\gamma_D + \gamma_F W_D} . \tag{B.4b}$$

For low temperatures ($W_D = 0$) the transient case ($G = 0$) takes a concise form setting the boundary conditions to $n_F(0) = G/(\gamma_c + \gamma_F)$ and $n_D(0) = 0$, respectively:

$$n_F = \frac{G}{\gamma_c + \gamma_F} e^{-(\gamma_c + \gamma_F)t} , \tag{B.5a}$$

$$n_D = \frac{\gamma_c G}{(\gamma_c + \gamma_F)(\gamma_D - \gamma_c - \gamma_F)} \left(e^{-(\gamma_c + \gamma_F)t} - e^{-\gamma_D t} \right) . \tag{B.5b}$$

n_F and n_D are coupled via γ_c. While n_F decays exponentially, n_D rises (free excitons are captured by donors), before eventually an exponential decay sets in.

B.2. Free carrier recombination

If the thermal energy $k_B T$ is large compared to the exciton binding energy E_{FX}, excitons are not stable and the recombination of free charge carriers dominates the recombination processes in semiconductors. Considering again an n-type semiconductor, the densities of electrons n and of holes p under steady state conditions are given by:

$$\frac{dn}{dt} = G - Bnp - b_n n n_t^+ = 0 , \tag{B.6a}$$

$$\frac{dp}{dt} = G - Bnp - b_p p n_t^0 = 0 , \tag{B.6b}$$

where B is the bimolecular radiative recombination coefficient and b_n and b_p are the capture coefficients of positively charged (n_t^+) and neutral (n_t^0) nonradiative trap centers. At elevated temperatures, all donors are ionized and thus, the electron concentration equals the donor concentration N_D. If the semiconductor is excited, excess electrons and holes are generated with equal densities $\Delta n = \Delta p$. Consequently, the carrier concentrations can be written as $n = N_D + \Delta n$ and $p = \Delta p$. The last term in Eqs. B.6 describes the nonradiative recombination R_{nr} via a trap state. It is equal for both carrier types:

$$R_{nr} = b_n n n_t^+ = b_p p n_t^0 . \tag{B.7}$$

The density of trap states is the sum of neutral and charged trap state densities, $N_t = n_t^+ + n_t^0$. Applying this relation yields:

$$b_n n (N_t - n_t^0) = b_p p n_t^0 \quad \text{and} \tag{B.8}$$

$$n_t^0 = \frac{b_n n}{b_n n + b_p p} N_t . \tag{B.9}$$

The nonradiative recombination is then given by:

$$R_{nr} = \frac{b_n b_p np}{b_n n + b_p p} N_t \,, \tag{B.10}$$

which is the well-established Shockley-Read-Hall expression.[65,66]

Considering low excitation conditions ($\Delta n = \Delta p \ll N_D$, indicated by index l) the radiative recombination (the second term in Eqs. B.6) is rewritten as:

$$R_r^l = B(\Delta n + N_D)\Delta p = B N_D \Delta p \tag{B.11}$$

$$R_r^l = \gamma_r^l \Delta p = \frac{\Delta p}{\tau_r^l} \,. \tag{B.12}$$

Similarly, the nonradiative recombination can be treated:

$$R_{nr}^l = \frac{b_n b_p (\Delta n + N_D)\Delta p}{b_n(\Delta n + N_D) + b_p \Delta p} N_t = \frac{b_n b_p N_D \Delta p}{b_n N_D} N_t = b_p \Delta p N_t \tag{B.13}$$

$$R_{nr}^l = \gamma_{nr}^l \Delta p = \frac{\Delta p}{\tau_{nr}^l} \,. \tag{B.14}$$

The recombination dynamics are thus determined by the minority charge carriers. In the transient case ($G = 0$) Eq. B.6b can be rewritten as:

$$\frac{dp}{dt} = -R_r^l - R_{nr}^l = -(\gamma_r^l + \gamma_{nr}^l)\Delta p = -\gamma_{eff}^l p \,. \tag{B.15}$$

The solution of this differential equation is an exponential function with the initial condition $p(0) = G/\gamma_{eff}^l$:

$$p = \frac{G}{\gamma_{eff}^l} e^{-\gamma_{eff}^l t} \,. \tag{B.16}$$

The case of high excitation (index h) can be treated in the same manner. Here, $\Delta n = \Delta p \gg N_D$. The radiative term is then determined to:

$$R_r^h = B(\Delta n + N_D)\Delta p = B \Delta p^2 \,. \tag{B.17}$$

Hence, the radiative recombination goes quadratically with the number of charge carriers. The nonradiative recombination is again obtained from Eq. B.10:

$$R_{nr}^h = \frac{b_n b_p (\Delta n + N_D)\Delta p}{b_n(\Delta n + N_D) + b_p \Delta p} N_t = \frac{b_n b_p \Delta p^2}{(b_n + b_p)\Delta p} N_t = \frac{b_n b_p}{b_n + b_p} N_t \Delta p \,, \tag{B.18}$$

$$R_{nr}^h = \gamma_{nr}^h \Delta p = \frac{\Delta p}{\tau_{nr}^h} \,. \tag{B.19}$$

B. Recombination processes
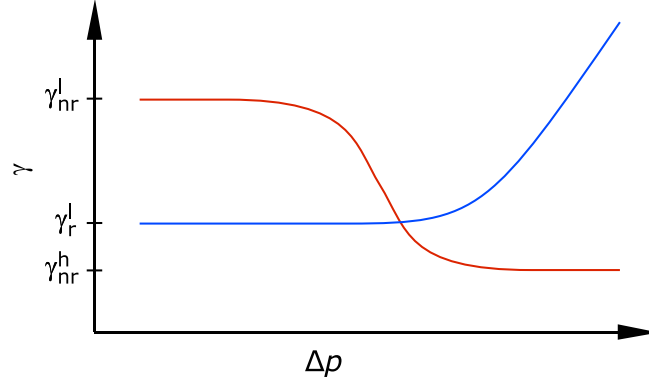
Figure B.1.: Schematic illustration of the excitation density dependence of the radiative and nonradiative recombination rates.

The transient case is then given by:

$$\frac{dp}{dt} = -R_r^h - R_{nr}^h = -B\Delta p^2 - \gamma_{nr}^h \Delta p \,, \tag{B.20}$$

$$\frac{dp}{Bp^2 + \gamma_{nr}^h p} = -dt \,. \tag{B.21}$$

Integration on both sides yields (with c and c' being constants):

$$-\frac{1}{\gamma_{nr}^h} \ln\left(\frac{Bp + \gamma_{nr}^h}{p}\right) = -t + c \,, \tag{B.22}$$

$$p = \frac{\gamma_{nr}^h}{B - c' e^{\gamma_{nr}^h t}} \,. \tag{B.23}$$

c' can be obtained from the initial condition $p(0)$. Equation B.20 results in $p(0) \approx G/2\gamma_{nr}^h$. Consequently, p is given by:

$$p = \frac{G\gamma_{nr}^h}{GB + (2(\gamma_{nr}^h)^2 - GB)e^{\gamma_{nr}^h t}} \,, \tag{B.24}$$

which represents a much more complex solution than in the case of low excitation.

The dependence of the radiative and nonradiative recombination rates on the excitation density is schematically depicted in Fig. B.1. γ_r (blue) is constant at low carrier densities (exponential decay) and increases linearly at high excitation. γ_{nr} equals $b_p N_t$ at low excitation while at high excitation the ratio of b_p and b_n determines the nonradiative recombination rate. With Eq. B.18, γ_{nr} equals $b_p N_t$, $b_p N_t/2$, and $b_n N_t$ for $b_p \ll b_n$, $b_p = b_n$, and $b_p \gg b_n$, respectively. In excitation density ranges, where γ_r or γ_{nr} are not constant, the PL intensity increases nonlinearly with excitation density.

C. Rate equation system describing the Fermi level unpinning

Rate equation system

In order to further examine the change of the recombination dynamics upon oxygen desorption, the system can be modeled with a set of rate equations. The FX, (D^0,X), and (U,X) densities are given by n_F, n_D and n_U, respectively. Free excitons are generated with a rate G and can relax to the (D^0,X) and (U,X) state with the rates γ_{cD} and γ_{cU}. If bound excitons experience an electric field $\mathcal{E}$ with an energy E_{el} they can be released from their associated impurity or defect. For the same reason, free excitons may dissociate.[58,186] Both processes are described by the respective rates W_D, W_U and W_F. Radiative and non-radiative recombination rates are merged into emission rates:

$$\gamma_F = \gamma_{F,r} + \gamma_{F,nr} = \frac{1}{\tau_F}, \tag{C.1a}$$

$$\gamma_D = \gamma_{D,r} + \gamma_{D,nr} = \frac{1}{\tau_D}, \tag{C.1b}$$

$$\text{and} \quad \gamma_U = \gamma_{U,r} + \gamma_{U,nr} = \frac{1}{\tau_U}. \tag{C.1c}$$

For measurements at low temperature the exchange between between (D^0,X) and (U,X) complexes is unlikely and therefore neglected. Similarly, the dissociation rate of bound excitons is considered to equal zero. Under steady-state conditions the system of coupled rate equations can then be expressed as:

$$\frac{dn_F}{dt} = -(\gamma_{cD} + \gamma_{cU} + W_F + \gamma_F)n_F + W_D n_D + W_U n_U + G = 0, \tag{C.2a}$$

$$\frac{dn_D}{dt} = -(W_D + \gamma_D)n_D + \gamma_{cD} n_F = 0, \tag{C.2b}$$

$$\text{and} \quad \frac{dn_U}{dt} = -(W_U + \gamma_U)n_U + \gamma_{cU} n_F = 0. \tag{C.2c}$$

The PL spectra obtained from the desorption experiment under pulsed excitation are dominated by the (D^0,X) and (U,X) line, while the FX transition is not resolved. Thus, only the intensities I_D and I_U will be discussed in the following as their evolution can be determined from the time-resolved PL data. These intensities are determined by the number of radiatively recombining excitons:

$$I_D = \gamma_{D,r} n_D \tag{C.3a}$$

$$\text{and} \quad I_U = \gamma_{U,r} n_U. \tag{C.3b}$$

From the experiment, the intensities before (I_i^{ox}) and after (I_i^{des}) oxygen desorption can be determined. Under the assumption that the FX recombination rate remains constant,

C. Rate equation system describing the Fermi level unpinning

the ratio of the intensities before and after desorption can be written as:

$$\frac{I_D^{des}}{I_D^{ox}} = \frac{\gamma_{D,r}^{des} n_D^{des}}{\gamma_{D,r}^{ox} n_D^{ox}} = \frac{\gamma_{D,r}^{des}(W_D^{des} + \gamma_D^{des})}{\gamma_{D,r}^{ox}(W_D^{ox} + \gamma_D^{ox})} \tag{C.4a}$$

$$\text{and} \quad \frac{I_U^{des}}{I_U^{ox}} = \frac{\gamma_{U,r}^{des} n_U^{des}}{\gamma_{U,r}^{ox} n_U^{ox}} = \frac{\gamma_{U,r}^{des}(W_U^{des} + \gamma_U^{des})}{\gamma_{U,r}^{ox}(W_U^{ox} + \gamma_U^{ox})} \ . \tag{C.4b}$$

The emission rates γ_i^{des} and γ_i^{ox} are determined from the transients and the ratios $\gamma_{i,r}^{des}/\gamma_{i,r}^{ox}$ are deduced from the initial intensity increase at $t = 0$. Finally, the ratio I_i^{des}/I_i^{ox} is obtained from the temporally integrated transients. The evolution of the electric field can now be discussed, when Eqs. C.4 are solved for the ionization rates W_i^{ox}:

$$W_D^{ox} = \frac{I_D^{des}}{I_D^{ox}} \frac{\gamma_{D,r}^{ox}}{\gamma_{D,r}^{des}} \left(W_D^{des} + \gamma_D^{des}\right) - \gamma_D^{ox} \tag{C.5a}$$

$$\text{and} \quad W_U^{ox} = \frac{I_U^{des}}{I_U^{ox}} \frac{\gamma_{U,r}^{ox}}{\gamma_{U,r}^{des}} \left(W_U^{des} + \gamma_U^{des}\right) - \gamma_U^{ox} \ . \tag{C.5b}$$

Using the data summarized in Tab. 7.1, the ionization rates are given by:

$$W_D^{des} = 0.45 \, W_D^{ox} - 0.0025 \, \text{ps}^{-1} \tag{C.6a}$$

$$\text{and} \quad W_U^{des} = 0.97 \, W_U^{ox} - 0.0002 \, \text{ps}^{-1} \ . \tag{C.6b}$$

Both, W_D and W_U decrease during the desorption process. The ionization rates W_i depend on the electric field energy E_{el} as $W_i \propto \exp\left(-cE_{iX}/E_{el}\right)$, where c is a constant and E_{iX} represents the exciton binding energy.[58] The decrease of W_i therefore indicates a decreasing electric field. In other words, the results of the rate equation model are consistent with an unpinning of the Fermi level as described in Sec. 7.2.

Bibliography

[1] ITRS webpage. URL `http://www.itrs.net`. Accessed on 04.06.2010.

[2] P. S. Peercy. The drive to miniaturization. *Nature (London)*, 406:1023–1026, 2000.

[3] Wei Lu and Charles M. Lieber. Nanoelectronics from the bottom up. *Nature Mater.*, 6:841–850, 2007.

[4] Wei Lu and Charles M. Lieber. Topical review - semiconductor nanowires. *J. Phys. D*, 39:R387, 2006.

[5] E. Calleja, M. A. Sánchez-García, F. J. Sánchez, F. Calle, F. B. Naranjo, E. Muñoz, U. Jahn, and K. H. Ploog. Luminescence properties and defects in GaN nanocolumns grown by molecular beam epitaxy. *Phys. Rev. B*, 62:16826, 2000.

[6] Kimberly A. Dick. A review of nanowire growth promoted by alloys and non-alloying elements with emphasis on Au-assisted III-V nanowires. *Progr. Cryst. Gr. Char. Mater.*, 54:138–173, 2008.

[7] V. Schmidt, J. V. Wittemann, and U. Gösele. Growth, Thermodynamics, and Electrical Properties of Silicon Nanowires. *Chem. Rev.*, 110:361–388, 2010.

[8] Y. W. Heo, D. P. Norton, L. C. Tien, Y. Kwon, B. S Kang, F. Ren, S. J. Pearton, and J. R. LaRoche. ZnO nanowire growth and devices. *Mater. Sc. Eng. R. Rep.*, 47:1, 2004.

[9] Ritesh Agarwal. Heterointerfaces in Semiconductor Nanowires. *Small*, 4:1872–1893, 2008.

[10] Satoshi Harui, Hidetoshi Tamiya, Takanobu Akagi, Hideto Miyake, Kazumasa Hiramatsu, Tsutomu Araki, and Yasushi Nanishi. Transmission Electron Microscopy Characterization of Position-Controlled InN Nanocolumns. *Jpn. J. Appl. Phys.*, 47:5330, 2008.

[11] F. Glas. Critical dimensions for the plastic relaxation of strained axial heterostructures in free-standing nanowires. *Phys. Rev. B*, 74:121302(R), 2006.

[12] E. Ertekin, P. A. Greaney, D. C. Chrzan, and T. D. Sands. Equilibrium limits of coherency in strained nanowire heterostructures. *J. Appl. Phys.*, 97:114325, 2005.

[13] Nicolas Thillosen, Kathrin Sebald, Hilde Hardtdegen, Ralph Meijers, Raffaella Calarco, Simone Montanari, Nicoleta Kaluza, Jürgen Gutowski, and Hans Lüth. The state of strain in single GaN nanocolumns as derived from micro-photoluminescence measurements. *Nano Lett.*, 6:704–708, 2006.

[14] M. G. Lagally and R. H. Blick. Materials science: A 'bed of nails' on silicon. *Nature (London)*, 432:450–451, 2004.

[15] R. Agarwal and C. M. Lieber. Semiconductor nanowires: optics and optoelectronics. *Appl. Phys. A*, 85:209, 2006.

[16] C. M. Lieber and Z. L. Wang. Functional Nanowires. *MRS. Bulletin*, 32:99, 2007.

[17] Fernando Patolsky and Charles M. Lieber. Nanowire nanosensors. *Mater. Today*, 8: 20–28, 2005.

[18] Xiangfeng F. Duan, Yu Huang, Ritesh Agarwal, and Charles M. Lieber. Single-nanowire electrically driven lasers. *Nature (London)*, 421:241–245, 2003.

[19] C. M. Lieber. Nanoscale Science and Technology: Building a Big Future from Small Things. *MRS. Bulletin*, 28:486, 2003.

[20] Lars Samuelson. Self-forming nanoscale devices. *Mater. Today*, 6:22, 2003.

[21] M. Knelangen, V. Consonni, A. Trampert, and H. Riechert. In-situ analysis of strain relaxation during catalyst-free nucleation and growth of GaN nanowires. *Nano Technol.*, 21:245705, 2010.

[22] M. Tchernycheva, J. C. Harmand, G. Patriarche, L. Travers, and G. E. Cirlin. Temperature conditions for GaAs nanowire formation by Au-assisted molecular beam epitaxy. *Nano Technol.*, 17:4025, 2006.

[23] L. H. Robins, K. A. Bertness, J. M. Barker, N. A. Sanford, and J. B. Schlager. Optical and structural study of GaN nanowires grown by catalyst-free molecular beam epitaxy. II. Sub-band-gap luminescence and electron irradiation effects. *J. Appl. Phys.*, 101:113506, 2007.

[24] Martin Heiss, Sonia Conesa-Boj, Jun Ren, Hsiang-Han Tseng, Adam Gali, Andreas Rudolph, Emanuele Uccelli, Francesca Peiró, Joan Ramon Morante, Dieter Schuh, Elisabeth Reiger, Efthimios Kaxiras, Jordi Arbiol, and Anna Fontcuberta i Morral. Direct correlation of crystal structure and optical properties in wurtzite/zinc-blende GaAs nanowire heterostructures. *Phys. Rev. B*, 83:045303, 2011.

[25] S. W. Jung, W. I. Park, H. D. Cheong, Gyu-Chul Yi, Hyun M. Jang, S. Hong, and T. Joo. Time-resolved and time-integrated photoluminescence in ZnO epilayers grown on Al_2O_3(0001) by metalorganic vapor phase epitaxy. *Appl. Phys. Lett.*, 80: 1924–1926, 2002.

[26] Jinkyoung Yoo, Young-Joon Hong, Sung Jin An, Gyu-Chul Yi, Bonghwan Chon, Taiha Joo, Jong-Wook Kim, and Jeong-Soo Lee. Photoluminescent characteristics of Ni-catalyzed GaN nanowires. *Appl. Phys. Lett.*, 89:043124, 2006.

[27] Tobias Voss, Geoffry T. Svacha, Eric Mazur, Sven Müller, Carsten Ronning, Denan Konjhodzic, and Frank Marlow. High-Order Waveguide Modes in ZnO Nanowires. *Nano Lett.*, 7:3675–3680, 2007.

[28] Julien Claudon, Joel Bleuse, Nitin Singh Malik, Maela Bazin, Perine Jaffrennou, Niels Gregersen, Christophe Sauvan, Philippe Lalanne, and Jean-Michel Gérard. A highly efficient single-photon source based on a quantum dot in a photonic nanowire. *Nature Phot.*, 4:174–177, 2010.

[29] Hwa-Mok Kim, Yong-Hoon Cho, Hosang Lee, Suk Il Kim, Sung R. Ryu, Deuk Y. Kim, Tae W. Kang, and Kwan S. Chung. High-Brightness Light Emitting Diodes Using Dislocation-Free Indium Gallium Nitride/Gallium Nitride Multiquantum-Well Nanorod Arrays. *Nano Lett.*, 4:1059–1062, 2004.

[30] S. Porowski and I. Grzegory. Thermodynamical properties of III-V nitrides and crystal growth of GaN at high N2 pressure. *J. Cryst. Growth*, 178:174–188, 1997.

[31] Akihiko Kikuchi, Mizue Kawai, Makoto Tada, and Katsumi Kishino. InGaN/GaN Multiple Quantum Disk Nanocolumn Light-Emitting Diodes Grown on (111) Si Substrate. *Jpn. J. Appl. Phys.*, 43:L1524, 2004.

[32] Hiroto Sekiguchi, Kei Kato, Jo Tanaka, Akihiko Kikuchi, and Katsumi Kishino. Ultraviolet GaN-based nanocolumn light-emitting diodes grown on n-(111) Si substrates by rf-plasma-assisted molecular beam epitaxy. *Phys. Stat. Sol. A*, 205:1067, 2008.

[33] Yu Huang, Xiangfeng Duan, Yi Cui, and Charles M. Lieber. Gallium Nitride Nanowire Nanodevices. *Nano Lett.*, 2:101–104, 2002.

[34] Reui-San Chen, Hsin-Yi Chen, Chien-Yao Lu, Kuei-Hsien Chen, Chin-Pei Chen, Li-Chyong Chen, and Ying-Jay Yang. Ultrahigh photocurrent gain in *m*-axial GaN nanowires. *Appl. Phys. Lett.*, 91:223106, 2007.

[35] M. H. Huang, S. Mao, H. Feick, H. Yan, Y. Wu, H. Kind, E. Weber, R. Russo, and P. Yang. Room-temperature ultraviolet nanowire nanolasers. *Science*, 292:1897–1899, 2001.

[36] Charles Kittel. *Introduction to Solid State Physics*. John Wiley & Sons, 1996.

[37] Hadis Morkoç. *Nitride Semiconductors and Devices*, volume 32 of *Materials Science*. Springer, Berlin, 1999.

[38] Jacques I. Pankove. *Optical Processes in Semiconductors*. Dover Publications, New York, 1971.

[39] Jacques I. Pankove and Theodore D. Moustakas, editors. *Gallium Nitride (GaN) I*, volume 50 of *Semiconductors and Semimetals*. Academic Press, San Diego, 1998.

[40] Robert S. Knox. *Theory of Excitons*, volume 5 of *Sol. Stat. Phys.* Academic Press, New York, 1963.

[41] DIAMOND program. URL http://www.crystalimpact.com/diamond/.

[42] S. Breuer, M. Hilse, A. Trampert, L. Geelhaar, and H. Riechert. Vapor-liquid-solid nucleation of GaAs on Si(111): Growth evolution from traces to nanowires. *Phys. Rev. B*, 82:075406, 2010.

[43] J. Renard, G. Tourbot, D. Sam-Giao, C. Bougerol, B. Daudin, and B. Gayral. Optical spectroscopy of cubic GaN in nanowires. *Appl. Phys. Lett.*, 97:081910, 2010.

[44] Jianwei Zhao, Lirong Qin, Yong Zhang, Yonghao Hao, Qing Guo, and Lide Zhang. Catalytic growth of cubic phase ZnO nanowires with jagged surface. *Micro Nano Lett.*, 5:336–339, 2010.

Bibliography

[45] Y. T. Rebane, Y. G. Shreter, and M. Albrecht. Stacking Faults as Quantum Wells for Excitons in Wurtzite GaN. *Phys. Stat. Sol. A*, 164:141, 1997.

[46] V. Consonni, M. Knelangen, U. Jahn, A. Trampert, L. Geelhaar, and H. Riechert. Effects of nanowire coalescence on their structural and optical properties on a local scale. *Appl. Phys. Lett.*, 95:241910, 2009.

[47] D. Spirkoska, J. Arbiol, A. Gustafsson, S. Conesa-Boj, F. Glas, I. Zardo, M. Heigoldt, M. H. Gass, A. L. Bleloch, S. Estrade, M. Kaniber, J. Rossler, F. Peiro, J. R. Morante, G. Abstreiter, L. Samuelson, and A. Fontcuberta i Morral. Structural and optical properties of high quality zinc-blende/wurtzite GaAs nanowire heterostructures. *Phys. Rev. B*, 80:245325, 2009.

[48] P. Misra, O. Brandt, H. T. Grahn, H. Teisseyre, M. Siekacz, C. Skierbiszewski, and B. Łucznik. Complete in-plane polarization anisotropy of the A exciton in un-strained *A*-plane GaN films. *Appl. Phys. Lett.*, 91:141903, 2007.

[49] K. P. Korona, A. Wysmołek, K. Pakuła, R. Stępniewski, J. M. Baranowski, I. Grze-gory, B. Łucznik, M. Wróblewski, and S. Porowski. Exciton region reflectance of homoepitaxial GaN layers. *Appl. Phys. Lett.*, 69:788–790, 1996.

[50] D. D. Sell. Resolved Free-Exciton Transitions in the Optical-Absorption Spectrum of GaAs. *Phys. Rev. B*, 6:3750–3753, 1972.

[51] K. Kornitzer, T. Ebner, K. Thonke, R. Sauer, C. Kirchner, V. Schwegler, M. Kamp, M. Leszczynski, I. Grzegory, and S. Porowski. Photoluminescence and reflectance spectroscopy of excitonic transitions in high-quality homoepitaxial GaN films. *Phys. Rev. B*, 60:1471, 1999.

[52] D. C. Reynolds, D. C. Look, B. Jogai, C. W. Litton, W. C. Harsch, and G. Cantwell. Valence-band ordering in ZnO. *Phys. Rev. B*, 60:2340, 1999.

[53] V. A. Rodina, M. Dietrich, A. Göldner, L. Eckey, A. Hoffmann, Al. L. Efros, M. Rosen, and B. K. Meyer. Free excitons in wurtzite GaN. *Phys. Rev. B*, 64:115204, 2001.

[54] D. Volm, K. Oettinger, T. Streibl, D. Kovalev, M. Ben-Chorin, J. Diener, B. K. Meyer, J. Majewski, L. Eckey, A. Hoffmann, H. Amano, I. Akasaki, K. Hiramatsu, and T. Detchprohm. Exciton fine structure in undoped GaN epitaxial films. *Phys. Rev. B*, 53:16543–16550, 1996.

[55] Lorenzo Pavesi and Mario Guzzi. Photoluminescence of $Al_xGa_{1-x}As$ alloys. *J. Appl. Phys.*, 75:4779–4842, 1994.

[56] A. Teke, Ü. Özgür, S. Dogan, X. Gu, H. Morkoç, B. Nemeth, J. Nause, and H. Everitt. Excitonic fine structure and recombination dynamics in single-crystalline ZnO. *Phys. Rev. B*, 70:195207, 2004.

[57] A. D. Yoffe. Semiconductor quantum dots and related systems: Electronic, optical, luminescence and related properties of low dimensional systems. *Adv. Phys.*, 50: 1–208, 2001.

[58] J. Pedrós, Y. Takagaki, T. Ive, M. Ramsteiner, O. Brandt, U. Jahn, K. H. Ploog, and F. Calle. Exciton impact-ionization dynamics modulated by surface acoustic waves in GaN. *Phys. Rev. B*, 75:115305, 2007.

[59] Ü. Özgür, Ya. I. Alivov, C. Liu, A. Teke, M. A. Reshchikov, S. Doğan, V. Avrutin, S.-J. Cho, and H. Morkoç. A comprehensive review of ZnO materials and devices. *J. Appl. Phys.*, 98:041301, 2005.

[60] Eiichi Hanamura. Rapid radiative decay and enhanced optical nonlinearity of excitons in a quantum well. *Phys. Rev. B*, 38:1228–1234, 1988.

[61] J. R. Haynes. Experimental Proof of the Existence of a New Electronic Complex in Silicon. *Phys. Rev. Lett.*, 4:361–363, 1960.

[62] G. W. 't Hooft, W. A. J. A. van der Poel, L. W. Molenkamp, and C. T. Foxon. Giant oscillator strength of free excitons in GaAs. *Phys. Rev. B*, 35:8281–8284, 1987.

[63] S. J. Rosner, E. C. Carr, M. J. Ludowise, G. Girolami, and H. I. Erikson. Correlation of cathodoluminescence inhomogeneity with microstructural defects in epitaxial GaN grown by metalorganic chemical-vapor deposition. *Appl. Phys. Lett.*, 70:420–422, 1997.

[64] D. F. Nelson, J. D. Cuthbert, P. J. Dean, and D. G. Thomas. Auger recombination of excitons bound to neutral donors in gallium phosphide and silicon. *Phys. Rev. Lett.*, 17:1262–1265, 1966.

[65] W. Shockley and W. T. Read, Jr. Statistics of the recombinations of holes and electrons. *Phys. Rev.*, 87:835–842, 1952.

[66] R. N. Hall. Electron-Hole Recombination in Germanium. *Phys. Rev.*, 87:387, 1952.

[67] Juan Bisquert, Germà Garcia-Belmonte, and Francisco Fabregat-Santiago. Modelling the electric potential distribution in the dark in nanoporous semiconductor electrodes. *J. Sol. St. El.-chem.*, 3:337–347, 1999. 10.1007/s100080050164.

[68] Chris G. van de Walle and David Segev. Microscopic origins of surface states on nitride surfaces. *J. Appl. Phys.*, 101:081704, 2007.

[69] M. Foussekis, A. A. Baski, and M. A. Reshchikov. Photoadsorption and photodesorption for GaN. *Appl. Phys. Lett.*, 94:162116, 2009.

[70] V. M. Bermudez. Study of oxygen chemisorption on the GaN(0001)-(1×1) surface. *J. Appl. Phys.*, 80:1190–1200, 1996.

[71] G. Koley and M. G. Spencer. Surface potential measurements on GaN and AlGaN/GaN heterostructures by scanning Kelvin probe microscopy. *J. Appl. Phys.*, 90:337–344, 2001.

[72] C. I. Wu, A. Kahn, N. Taskar, D. Dorman, and D. Gallagher. GaN (0001)-(1×1) surfaces: Composition and electronic properties. *J. Appl. Phys.*, 83:4249–4252, 1998.

[73] J. P. Long and V. M. Bermudez. Band bending and photoemission-induced surface photovoltages on clean n- and p-GaN (0001) surfaces. *Phys. Rev. B*, 66:121308, 2002.

[74] John E. Northrup and Jörg Neugebauer. Theory of GaN(10$\bar{1}$0) and (11$\bar{2}$0) surfaces. *Phys. Rev. B*, 53:R10477, 1996.

[75] R. Calarco, M. Marso, T. Richter, A. I. Aykanat, R. Meijers, A. v. d. Hart, T. Stoica, and H. Lüth. Size-dependent Photoconductivity in MBE-Grown GaN-Nanowires. *Nano Lett.*, 5:981–984, 2005.

[76] B. S. Simpkins, M. A. Mastro, C. R. Eddy, Jr., and P. E. Pehrsso. Surface depletion effects in semiconducting nanowires. *J. Appl. Phys.*, 103:104313, 2008.

[77] John David Jackson. *Classical Electrodynamics*. John Wiley & Sons, New York, 2 edition, 1975.

[78] Erik P. A. M. Bakkers, Jorden A. van Dam, Silvano de Franceschi, Leo P. Kouwenhoven, Monja Kaiser, Marcel Verheijen, Harry Wondergem, and Paul van der Sluis. Epitaxial growth of InP nanowires on germanium. *Nature Mater.*, 3:769–773, 2004.

[79] A. E. H. Love. *A Treatise on the Mathematical Theory of Elasticity*. Dover, New York, fourth edition, 1944.

[80] G. W. Housner and T. Vreeland, Jr. *The Analysis of Stress and Deformation*. McMillan, New York, 1966.

[81] S. Timoshenko and J. N. Goodier. *Theory of Elasticity*. McGraw-Hill, New York, second edition, 1951.

[82] Tevye Kuykendall, Philipp Ulrich, Shaul Aloni, and Peidong Yang. Complete composition tunability of InGaN nanowires using a combinatorial approach. *Nature Mater.*, 6:951–956, 2007.

[83] Christoph Böcklin, Ratko G. Veprek, Sebastian Steiger, and Bernd Witzigmann. Computational study of an InGaN/GaN nanocolumn light-emitting diode. *Phys. Rev. B*, 81:155306, 2010.

[84] Y. Xia, P. Yang, Y. Sun, Y. Wu, B. Mayers, B. Gates, Y. Yin, F. Kim, and H. Yan. One-Dimensional Nanostructures: Synthesis, Characterization, and Applications. *Adv. Mater.*, 15:353, 2003.

[85] S. Noor Mohammad. Self-catalysis: A contamination-free, substrate-free growth mechanism for single-crystal nanowire and nanotube growth by chemical vapor deposition. *J. Chem. Phys.*, 125:094705, 2006.

[86] R. S. Wagner and W. C. Ellis. Vapor-liquid-solid mechanism of single crystal growth. *Appl. Phys. Lett.*, 4:89–90, 1964.

[87] L. Samuelson, C. Thelander, M. T. Björk, M. Borgström, K. Deppert, K. A. Dick, A. E. Hansen, T. Mårtensson, N. Panev, A. I. Persson, W. Seifert, N. Sköld, M. W. Larsson, and L. R. Wallenberg. Semiconductor nanowires for 0D and 1D physics and applications. *Physica E*, 25:313–318, 2004. Proceedings of the 13th International Winterschool on New Developments in Solid State Physics - Low-Dimensional Systems.

[88] A. Fontcuberta i Morral, C. Colombo, G. Abstreiter, J. Arbiol, and J. R. Morante. Nucleation mechanism of gallium-assisted molecular beam epitaxy growth of gallium arsenide nanowires. *Appl. Phys. Lett.*, 92:063112, 2008.

[89] V. Consonni, M. Knelangen, L. Geelhaar, A. Trampert, and H. Riechert. Nucleation mechanisms of epitaxial GaN nanowires: Origin of their self-induced formation and initial radius. *Phys. Rev. B*, 81:085310, 2010.

[90] K. A. Bertness, N. A. Sanford, J. M. Barker, J. B. Schlager, A. Roshko, A. V. Davydov, and I. Levin. Catalyst-Free Growth of GaN nanowires. *J. Electron. Mater.*, 35:576, 2006.

[91] C. Chèze, L. Geelhaar, B. Jenichen, and H. Riechert. Different growth rates for catalyst-induced and self-induced GaN nanowires. *Appl. Phys. Lett.*, 97:153105, 2010.

[92] Caroline Chèze. *Investigation and comparison of GaN nanowire nucleation and growth by the catalyst-assisted and self-induced approaches*. PhD thesis, Humboldt-Universität zu Berlin, 2010.

[93] John Vig. UV/ozone cleaning of surfaces. *J. Vac. Sci. Technol. A*, 3:1027–1034, 1985.

[94] CODATA webpage. URL `http://www.codata.org/`. Accessed on 03.08.2009.

[95] refractiveindex.info webpage. URL `http://refractiveindex.info/`. Accessed on 12.11.2010.

[96] Hiroshi Harima. Properties of gan and related compounds studied by means of raman scattering. *J. Phys.: Cond. Mat.*, 14:R967, 2002.

[97] Matt Law, Joshua Goldberger, and Peidong Yang. Semiconductor Nanowires and Nanotubes. *Ann. Rev. Mater. Res.*, 34:83, 2004.

[98] L. Samuelson, M. T. Björk, K. Deppert, M. Larsson, B. J. Ohlsson, N. Panev, A. I. Persson, N. Sköld, C. Thelander, and L. R. Wallenberg. Semiconductor nanowires for novel one-dimensional devices. *Physica E*, 21:560–567, 2004. Proceedings of the Eleventh International Conference on Modulated Semiconductor Structures.

[99] Steffen Breuer, Carsten Pfüller, Timur Flissikowski, Oliver Brandt, Holger T. Grahn, Lutz Geelhaar, and Henning Riechert. Suitability of Au- and Self-assisted GaAs Nanowires for Optoelectronic Applications. *Nano Lett.*, 2011.

[100] C. Pfüller, O. Brandt, T. Flissikowski, H. T. Grahn, T. Ive, J. S. Speck, and S. P. DenBaars. Comparison of the spectral and temporal emission characteristics of homoepitaxial and heteroepitaxial ZnO nanowires. *Appl. Phys. Lett.*, 98(11):113113, 2011.

[101] M. Tchernycheva, C. Sartel, G. Cirlin, L. Travers, G. Patriarche, Le Si Harmand, J-C. Dang, J. Renard, B. Gayral, L. Nevou, and F. Julien. Growth of GaN freestanding nanowires by plasma-assisted molecular beam epitaxy: structural and optical characterization. *Nano Technol.*, 18:385306, 2007.

Bibliography

[102] Thang B. Hoang, A. F. Moses, H. L. Zhou, D. L. Dheeraj, B. O. Fimland, and H. Weman. Observation of free exciton photoluminescence emission from single wurtzite GaAs nanowires. *Appl. Phys. Lett.*, 94:133105, 2009.

[103] Patrick Parkinson, Hannah J. Joyce, Qiang Gao, Hark Hoe Tan, Xin Zhang, Jin Zou, Chennupati Jagadish, Laura M. Herz, and Michael B. Johnston. Carrier Lifetime and Mobility Enhancement in Nearly Defect-Free Core-Shell Nanowires Measured Using Time-Resolved Terahertz Spectroscopy. *Nano Lett.*, 9:3349–3353, 2009. PMID: 19736975.

[104] J. B. Schlager, K. A. Bertness, P. T. Blanchard, L. H. Robins, A. Roshko, and N. A. Sanford. Steady-state and time-resolved photoluminescence from relaxed and strained GaN nanowires grown by catalyst-free molecular-beam epitaxy. *J. Appl. Phys.*, 103:124309, 2008.

[105] D. J. Wolford, G. D. Gilliland, T. F. Kuech, J. F. Klem, H. P. Hjalmarson, J. A. Bradley, C. F. Tsang, and J. Martinsen. Comparison of transport, recombination, and interfacial quality in molecular beam epitaxy and organometallic vapor-phase epitaxy GaAs/Al$_x$Ga$_{1-x}$As structures. *Appl. Phys. Lett.*, 64:1416–1418, 1994.

[106] H. A. Zarem, P. C. Sercel, J. A. Lebens, L. E. Eng, A. Yariv, and K. J. Vahala. Direct determination of the ambipolar diffusion length in GaAs/AlGaAs heterostructures by cathodoluminescence. *Appl. Phys. Lett.*, 55:1647–1649, 1989.

[107] A. Chiari, M. Colocci, F. Fermi, YH. Li, R Querzoli, A. Vinattieri, and WH. Zhuang. Temperature-dependence of the Photoluminescence in GaAs-GaAlAs Multiple Quantum Well Structures. *Phys. Stat. Sol. B*, 147:421–429, 1988.

[108] L. V. Titova, Thang B. Hoang, H. E. Jackson, L. M. Smith, J. M. Yarrison-Rice, Y. Kim, H. J. Joyce, H. H. Tan, and C. Jagadish. Temperature dependence of photoluminescence from single core-shell GaAs–AlGaAs nanowires. *Appl. Phys. Lett.*, 89:173126, 2006.

[109] B. K. Meyer, H. Alves, D. M. Hofmann, W. Kriegseis, D. Forster, F. Bertram, J. Christen, A. Hoffmann, M. Straßburg, M. Dworzak, U. Haboeck, and A. V. Rodina. Bound exciton and donor-acceptor pair recombinations in ZnO. *Phys. Stat. Sol. B*, 241:231, 2004.

[110] Linus C. Chuang, Michael Moewe, Shanna Crankshaw, and Connie Chang-Hasnain. Optical properties of InP nanowires on Si substrates with varied synthesis parameters. *Appl. Phys. Lett.*, 92:013121, 2008.

[111] J. E. Van Nostrand, K. L. Averett, R. Cortez, J. Boeckl, C. E. Stutz, N. A. Sanford, A. V. Davydov, and J. D. Albrecht. Molecular beam epitaxial growth of high-quality GaN nanocolumns. *J. Cryst. Growth*, 287:500, 2006.

[112] B. P. Zhang, N. T. Binh, Y. Segawa, Y. Kashiwaba, and K. Haga. Photoluminescence study of ZnO nanorods epitaxially grown on sapphire (11$\bar{2}$0) substrates. *Appl. Phys. Lett.*, 84:586–588, 2004.

[113] J. Grabowska, A. Meaney, K. K. Nanda, J.-P. Mosnier, M. O. Henry, J. R. Duclère, and E. McGlynn. Surface excitonic emission and quenching effects in ZnO nanowire/nanowall systems: Limiting effects on device potential. *Phys. Rev. B*, 71: 115439, 2005.

[114] V. V. Travnikov, A. Freiberg, and S. F. Savikhin. Surface excitons in ZnO crystals. *J. Lumin.*, 47:107, 1990.

[115] L. Wischmeier, T. Voss, I. Rückmann, J. Gutowski, A. C. Mofor, A. Bakin, and A. Waag. Dynamics of surface-excitonic emission in ZnO nanowires. *Phys. Rev. B*, 74:195333, 2006.

[116] D. C. Reynolds, D. C. Look, B. Jogai, C. W. Litton, T. Collins, W. C. Harsch, and G. Cantwell. Neutral-donor-bound-exciton complexes in ZnO crystals. *Phys. Rev. B*, 57:12151, 1998.

[117] G. Heiland, E. Mollwo, and F. Stöckmann. *Electronic Processes in Zinc Oxide*, volume 8 of *Sol. Stat. Phys.* Academic Press, 1959.

[118] K. Vanheusden, W. L. Warren, C. H. Seager, D. R. Tallant, J. A. Voigt, and B. E. Gnade. Mechanisms behind green photoluminescence in ZnO phosphor powders. *J. Appl. Phys.*, 79:7983–7990, 1996.

[119] P. Corfdir, P. Lefebvre, J. Ristić, P. Valvin, E. Calleja, A. Trampert, J.-D. Ganière, and B. Deveaud-Plédran. Time-resolved spectroscopy on GaN nanocolumns grown by plasma assisted molecular beam epitaxy on Si substrates. *J. Appl. Phys.*, 105:013113, 2009.

[120] J. S. Reparaz, F. Güell, M. R. Wagner, A. Hoffmann, A. Cornet, and J. R. Morante. Size-dependent recombination dynamics in ZnO nanowires. *Appl. Phys. Lett.*, 96: 053105, 2010.

[121] Q. X. Zhao, L. L. Yang, M. Willander, B. E. Sernelius, and P. O. Holtz. Surface recombination in ZnO nanorods grown by chemical bath deposition. *J. Appl. Phys.*, 104:073526, 2008.

[122] Kazumasa Hiramatsu, Theeradetch Detchprohm, and Isamu Akasaki. Relaxation Mechanism of Thermal Stresses in the Heterostructure of GaN Grown on Sapphire by Vapor Phase Epitaxy. *Jpn. J. Appl. Phys.*, 32:1528–1533, 1993.

[123] Nobuo Itoh, Jung Chul Rhee, Toshiharu Kawabata, and Susumu Koike. Study of cracking mechanism in GaN/α-Al$_2$O$_3$ structure. *J. Appl. Phys.*, 58:1828–1837, 1985.

[124] H. Lahrèche, P. Vennéguès, O. Tottereau, M. Laügt, P. Lorenzini, M. Leroux, B. Beaumont, and P. Gibart. Optimisation of AlN and GaN growth by metalorganic vapour-phase epitaxy (MOVPE) on Si (111). *J. Cryst. Growth*, 217:13–25, 2000.

[125] S. Li, S. Fündling, Ü. Sökmen, S. Merzsch, R. Neumann, P. Hinze, T. Weimann, U. Jahn, A. Trampert, H. Riechert, E. Peiner, H.-H. Wehmann, and A. Waag. GaN and LED structures grown on pre-patterned silicon pillar arrays. *Phys. Stat. Sol. C*, 7:84, 2010.

[126] H. Sekiguchi, T. Nakazato, A. Kikuchi, and K. Kishino. Structural and optical properties of GaN nanocolumns grown on (0001) sapphire substrates by rf-plasma-assisted molecular-beam epitaxy. *J. Cryst. Growth*, 300:259, 2007.

[127] H. Sekiguchi, K. Kishino, and A. Kikuchi. GaN/AlGaN nanocolumn ultraviolet light-emitting diodes grown on n-(111) Si by RF-plasma-assisted molecular beam epitaxy. *Electron. Lett.*, 44:151–152, 2008.

[128] Jelena Ristić, Enrique Calleja, Achim Trampert, Sergio Fernández-Garrido, Carlos Rivera, Uwe Jahn, and Klaus H. Ploog. Columnar AlGaN/GaN Nanocavities with AlN/GaN Bragg Reflectors Grown by Molecular Beam Epitaxy on Si(111). *Phys. Rev. Lett.*, 94:146102, 2005.

[129] Fang Qian, Silvija Gradecak, Yat Li, Cheng-Yen Wen, and Charles M. Lieber. Core/multishell nanowire heterostructures as multicolor, high-efficiency light-emitting diodes. *Nano Lett.*, 5:2287–2291, 2005.

[130] L. H. Robins, K. A. Bertness, J. M. Barker, N. A. Sanford, and J. B. Schlager. Optical and structural study of GaN nanowires grown by catalyst-free molecular beam epitaxy. I. Near-band-edge luminescence and strain effects. *J. Appl. Phys.*, 101:113505, 2007.

[131] Y. S. Park, C. M. Park, D. J. Fu, T. W. Kang, and J. E. Oh. Photoluminescence studies of GaN nanorods on Si(111) substrates grown by molecular-beam epitaxy. *Appl. Phys. Lett.*, 85:5718–5720, 2004.

[132] Florian Furtmayr, Martin Vielemeyer, Martin Stutzmann, Andreas Laufer, Bruno K. Meyer, and Martin Eickhoff. Optical properties of Si- and Mg-doped gallium nitride nanowires grown by plasma-assisted molecular beam epitaxy. *J. Appl. Phys.*, 104:074309, 2008.

[133] Ching-Lien Hsiao, Li-Wei Tu, Tung-Wei Chi, Min Chen, Tai-Fa Young, Chih-Ta Chia, and Yu-Ming Chang. Micro-Raman spectroscopy of a single freestanding GaN nanorod grown by molecular beam epitaxy. *Appl. Phys. Lett.*, 90:043102, 2007.

[134] P. P. Paskov, T. Paskova, P. O. Holtz, and B. Monemar. Polarized photoluminescence study of free and bound excitons in free-standing GaN. *Phys. Rev. B*, 70:035210, 2004.

[135] A. Wysmolek, K. P. Korona, R. Stępniewski, J. M. Baranowski, J. Błoniarz, M. Potemski, R. L. Jones, D. C. Look, J. Kuhl, S. S. Park, and S. K. Lee. Recombination of excitons bound to oxygen and silicon donors in freestanding GaN. *Phys. Rev. B*, 66:245317, 2002.

[136] K. Kornitzer, T. Ebner, M. Grehl, K. Thonke, R Sauer, C. Kirchner, V. Schwegler, M. Kamp, M. Leszczynski, I. Grzegory, and S. Porowski. High-Resolution Photoluminescence and Reflectance Spectra of Homoepitaxial GaN Layers. *Phys. Stat. Sol. B*, 216:5–9, 1999.

[137] M. A. Reshchikov, D. Huang, F. Yun, P. Visconti, L. He, H. Morkoç, J. Jasinski, Z. Liliental-Weber, R. J. Molnar, S. S. Park, and K. Y. Lee. Unusual luminescence lines in GaN. *J. Appl. Phys.*, 94:5623–5632, 2003.

[138] B. Monemar, P. P. Paskov, J. P. Bergman, A. A. Toropov, T. V. Shubina, T. Malinauskas, and A. Usui. Recombination of free and bound excitons in GaN. *Phys. Stat. Sol. B*, 245:1723, 2008.

[139] Jörg Neugebauer and Chris G. van de Walle. Gallium vacancies and the yellow luminescence in GaN. *Appl. Phys. Lett.*, 69:503–505, 1996.

[140] R. Pässler. Dispersion-related assessments of temperature dependences for the fundamental band gap of hexagonal GaN. *J. Appl. Phys.*, 90:3956–3964, 2001.

[141] Y. P. Varshni. Temperature dependence of the energy gap in semiconductors. *Physica*, 34:149–154, 1967.

[142] R. Pässler. Basic model relations for temperature dependencies of fundamental energy gaps in semiconductors. *Phys. Stat. Sol. B*, 200:155–172, 1997.

[143] O. Brandt, P. Waltereit, S. Dhar, U. Jahn, Y. J. Sun, A. Trampert, K. H. Ploog, M. A. Tagliente, and L. Tapfer. Properties of (In,Ga)N/GaN quantum wells grown by plasma-assisted molecular beam epitaxy. *J. Vac. Sci. Technol. B*, 20:1626–1639, 2002.

[144] Oliver Brandt, Hui Yang, and Klaus H. Ploog. Impact of recombination centers on the spontaneous emission of semiconductors under steady-state and transient conditions. *Phys. Rev. B*, 54:R5215, 1996.

[145] J. Lloyd-Hughes, S. K. E. Merchant, L. Fu, H. H. Tan, C. Jagadish, E. Castro-Camus, and M. B. Johnston. Influence of surface passivation on ultrafast carrier dynamics and terahertz radiation generation in GaAs. *Appl. Phys. Lett.*, 89:232102, 2006.

[146] J. H. Parker, Jr., D. W. Feldman, and M. Ashkin. Raman Scattering by Silicon and Germanium. *Phys. Rev.*, 155:712–714, 1967.

[147] K. Jeganathan, R. K. Debnath, R. Meijers, T. Stoica, R. Calarco, D. Grützmacher, and H. Lüth. Raman scattering of phonon-plasmon coupled modes in self-assembled GaN nanowires. *J. Appl. Phys.*, 105:123707, 2009.

[148] O. Brandt, 2010. Personal communication.

[149] A. Rathsfeld, 2009. Personal communication.

[150] B. Jenichen, 2010. Personal communication.

[151] M. A. Moram and M. E. Vickers. X-ray diffraction of III-nitrides. *Rep. Prog. Phys.*, 72:036502, 2009.

[152] L. Cerutti, J. Ristić, S. Fernández-Garrido, E. Calleja, A. Trampert, K. Ploog, S. Lazic, and J. Calleja. Wurtzite GaN nanocolumns grown on Si(001) by molecular beam epitaxy. *Appl. Phys. Lett.*, 88:213114, 2006.

[153] C. Kirchner, V. Schwegler, F. Eberhard, M. Kamp, K. J. Ebeling, K. Kornitzer, T. Ebner, K. Thonke, R. Sauer, P. Prystawko, M. Leszczynski, I. Grzegory, and S. Porowski. Homoepitaxial growth of GaN by metalorganic vapor phase epitaxy: A benchmark for GaN technology. *Appl. Phys. Lett.*, 75:1098–1100, 1999.

[154] K. Kornitzer, M. Grehl, K. Thonke, R. Sauer, C. Kirchner, V. Schwegler, M. Kamp, M. Leszczynski, I Grzegory, and S. Porowski. High-resolution PL spectra of donor- and acceptor-bound excitons in homoepitaxial GaN-layers. *Physica B*, 273-274:66, 1999.

[155] D. Karaiskaj, J. A. H. Stotz, T. Meyer, M. L. W. Thewalt, and M. Cardona. Impurity Absorption Spectroscopy in ^{28}Si: The Importance of Inhomogeneous Isotope Broadening. *Phys. Rev. Lett.*, 90:186402, 2003.

[156] Oliver Brandt, Carsten Pfüller, Caroline Chèze, Lutz Geelhaar, and Henning Riechert. Sub-meV linewidth of excitonic luminescence in single GaN nanowires: Direct evidence for surface excitons. *Phys. Rev. B*, 81:045302, 2010.

[157] Carsten Pfüller, Oliver Brandt, Timur Flissikowski, Caroline Chèze, Lutz Geelhaar, Holger T. Grahn, and Henning Riechert. Statistical analysis of excitonic transitions in single, free-standing GaN nanowires: Probing impurity incorporation in the poissonian limit. *Nano Res.*, 3:881–888, 2010. 10.1007/s12274-010-0061-1.

[158] J. Camacho, P. V. Santos, F. Alsina, M. Ramsteiner, K. H. Ploog, A. Cantarero, H. Obloh, and J. Wagner. Modulation of the electronic properties of GaN films by surface acoustic waves. *J. Appl. Phys.*, 94:1892–1897, 2003.

[159] Jules D. Levine. Nodal Hydrogenic Wave Functions of Donors on Semiconductor Surfaces. *Phys. Rev.*, 140:A586, 1965.

[160] S. Satpathy. Eigenstates of Wannier excitons near a semiconductor surface. *Phys. Rev. B*, 28:4585, 1983.

[161] Mamadou Diarra, Yann-Michel Niquet, Christophe Delerue, and Guy Allan. Ionization energy of donor and acceptor impurities in semiconductor nanowires: Importance of dielectric confinement. *Phys. Rev. B*, 75:045301, 2007.

[162] Michael A. Reshchikov and Hadis Morkoç. Luminescence properties of defects in GaN. *J. Appl. Phys.*, 97:061301, 2005.

[163] N. A. Sanford, P. T. Blanchard, K. A. Bertness, L. Mansfield, J. B. Schlager, A. W. Sanders, A. Roshko, B. B. Burton, and S. M. George. Steady-state and transient photoconductivity in *c*-axis GaN nanowires grown by nitrogen-plasma-assisted molecular beam epitaxy. *J. Appl. Phys.*, 107:034318, 2010.

[164] Naoyuki Ino and Naoki Yamamoto. Low temperature diffusion length of excitons in gallium nitride measured by cathodoluminescence technique. *Appl. Phys. Lett.*, 93:232103, 2008.

[165] F. Dubin, R. Melet, T. Barisien, R. Grousson, L. Legrand, M. Schott, and V. Voliotist. Macroscopic coherence of a single exciton state in an organic quantum wire. *Nature Phys.*, 2:32–35, 2006.

[166] C. Pfüller, O. Brandt, F. Grosse, T. Flissikowski, C. Chèze, V. Consonni, L. Geelhaar, H. T. Grahn, and H. Riechert. Unpinning the Fermi level of GaN nanowires by ultraviolet radiation. *Phys. Rev. B*, 82:045320, 2010.

[167] G. L. Snider, I.-H. Tan, and E. L. Hu. Electron states in mesa-etched one-dimensional quantum well wires. *J. Appl. Phys.*, 68:2849–2853, 1990.

[168] S. R. Morrison. *The Chemical Physics of Surfaces*. Plenum Press, New York, first edition, 1977.

[169] U. Behn, A. Thamm, O. Brandt, and H. T. Grahn. Unpinned behavior of the surface Fermi level of GaN detected by photoreflectance spectroscopy. *J. Appl. Phys.*, 87: 4315–4318, 2000.

[170] David Segev and Chris G. van de Walle. Electronic structure of nitride surfaces. *J. Cryst. Growth*, 300:199, 2007.

[171] M. Bertelli, P. Löptien, M. Wenderoth, A. Rizzi, R. G. Ulbrich, M. C. Righi, A. Ferretti, L. Martin-Samos, and C. M. Bertoni. Atomic and electronic structure of the nonpolar GaN(1$\bar{1}$00) surface. *Phys. Rev. B*, 80:115324, 2009.

[172] L. Ivanova, S. Borisova, H. Eisele, M. Dähne, A. Laubsch, and P. Ebert. Surface states and origin of the Fermi level pinning on nonpolar GaN(1$\bar{1}$00) surfaces. *Appl. Phys. Lett.*, 93:192110, 2008.

[173] Tommy Ive. *Growth and investigation of AlN/GaN and (Al,In)N/GaN based Bragg reflectors*. PhD thesis, Humboldt-Universität zu Berlin, 2005.

[174] Justin C. Johnson, Haoquan Yan, Peidong Yang, and Richard J. Saykally. Optical Cavity Effects in ZnO Nanowire Lasers and Waveguides. *J. Phys. Chem. B*, 107: 8816–8828, 2003.

[175] Anne-Line Henneghien, Gabriel Tourbot, Bruno Daudin, Olivier Lartigue, Yohan Désières, and Jean-Michel Gérard. Optical anisotropy and light extraction efficiency of MBE grown GaN nanowires epilayers. *Opt. Expr.*, 19:527–539, 2011.

[176] IMAGEJ program. URL `http://rsbweb.nih.gov/ij/`.

[177] R. Heitz, A. Hoffmann, and I. Broser. Exciton dynamics in Ni-activated CdS. *Phys. Rev. B*, 49:14307–14314, 1994.

[178] Jörg Neugebauer and Chris G. Van de Walle. Atomic geometry and electronic structure of native defects in GaN. *Phys. Rev. B*, 50:8067–8070, 1994.

[179] T. Mattila and R. M. Nieminen. Point-defect complexes and broadband luminescence in GaN and AlN . *Phys. Rev. B*, 55:9571–9576, 1997.

[180] P. Lefebvre, S. Fernández-Garrido, J. Grandal, J. Ristić, M.-A. Sánchez-García, and E. Calleja. Radiative defects in GaN nanocolumns: Correlation with growth conditions and sample morphology. *Appl. Phys. Lett.*, 98:083104, 2011.

[181] P. P. Paskov, B. Monemar, A. Toropov, J. P. Bergman, and A. Usui. Two-electron transition spectroscopy of shallow donors in bulk GaN. *Phys. Stat. Sol. C*, 4:2601, 2007.

[182] J. Teubert, 2010. Personal communication.

[183] K. Kishino, T. Hoshino, S. Ishizawa, and A. Kikuchi. Selective-area growth of GaN nanocolumns on titanium-mask-patterned silicon (111) substrates by RF-plasma-assisted molecular-beam epitaxy. *Electron. Lett.*, 44:819–821, 2008.

[184] R. K. Ahrenkiel and M. S. Lundstrom, editors. *Minority Carriers in III-V Semiconductors: Physics and Applications*, volume 39 of *Semiconductors and Semimetals*. Academic Press, 1993.

[185] S. M. Sze. *Semiconductor Devices, Physics and Technology*. John Wiley & Sons, New York, 1985.

[186] I. H. Oğuzman, E. Bellotti, K. F. Brennan, J. Kolník, R. Wang, and P. P. Ruden. Theory of hole initiated impact ionization in bulk zincblende and wurtzite GaN. *J. Appl. Phys.*, 81:7827–7834, 1997.

List of Figures

List of Tables

Acknowledgements

At this point, I would like to express my deep gratitude to the many people who supported me in the one or the other way.

I wish to thank Prof. H. Riechert for giving me the opportunity to work in this exciting field and to write this thesis. My thanks go to Prof. W. T. Masselink and Dr. habil. P. Lefebvre for reviewing this thesis.

I am grateful to Prof. H. T. Grahn for the supervision of this thesis, for taking the time to discuss my work, and for giving me the possibility to visit several conferences and workshops.

My gratitude goes to L. Geelhaar, for his interest in this work, for his advice and for the ability to place our results into a larger context.

I very much appreciate the work of O. Brandt. Without his support, brilliant ideas, and patience much of this thesis would not exist. His profound knowledge of semiconductor physics and his computational skills have been the solution to many of my questions. I enjoyed his perpetual curiosity and his willingness to discuss even absurd ideas and I hope that he had as much fun as I did. I learned a lot!

Several excellent experts working at PAUL-DRUDE-INSTITUTE have contributed to this work: T. Flissikowski performed TRPL measurements and supplied the routines for the statistical analysis of free-standing NWs. M. Ramsteiner had the idea to use Raman spectroscopy for the estimation of the quantum efficiency of NWs. U. Jahn performed CL measurements of GaN and GaAs NWs. A.-K. Bluhm took beautiful SEM images. F. Grosse simulated the desorption of oxygen from NW ensembles. V. Kaganer and K. Sabelfeld performed simulations of the decay dynamics of GaN NW ensembles. I enjoyed the discussions with all of these people and their contributions have been very valuable for my thesis.

The NW samples I have investigated have been fabricated by many different people. GaN NW samples have been synthesized by C. Chèze (at INFINEON and QIMONDA in Munich), M. Knelangen, T. Gotschke, V. Consonni, P. Dogan, M. Wölz, and F. Limbach. GaAs NW samples have been grown by S. Breuer and M. Hilse. The ZnO NWs have been produced by T. Ive at the UNIVERSITY OF CALIFORNIA in Santa Barbara. I am thankful for their constant efforts to produce excellent and/or challenging NW samples.

The growth of GaN NWs was partially supported by the EU Marie Curie RTN contract MRTN-CT-2004-005583 (PARSEM), by the IST project NODE 015783, and by the German BMBF joint research project MONALISA (Contract No. 01BL0810).

I appreciate the work of D. Dormeyer and S. Räther, who were able to find every single piece of literature, I requested. Furthermore, I thank the administrative personnel of PAUL-DRUDE-INSTITUTE for its motivated work.

Many other people have been supportive to me: L. Schrottke, B. Jenichen, R. Farshchi, E. Luna, Y. Takagaki, A. Trampert, H.-P. Schönherr, G. Paris, P. Grasnick, K. Arnhold,

134

Selbständigkeitserklärung

Ich erkläre, dass ich die vorliegende Arbeit selbständig und nur unter Verwendung der angegebenen Literatur und Hilfsmittel angefertigt habe.

Berlin, den 02.03.2011   Carsten Pfüller